Institut für Nutzpflanzenwissenschaften und Ressourcenschutz

Investigating the Potential of UAV-Based Low-Cost Camera Imagery for Measuring Biophysical Variables in Maize

Dissertation
zur Erlangung des Grades
Doktor der Agrarwissenschaften (Dr.agr.)
der Landwirtschaftlichen Fakultät
der
Rheinischen Friedrich-Wilhelms-Universität Bonn

vorgelegt von:

Dipl.-Geograph Andreas Tewes
aus Köln

Bonn 2018

Referent:	PD Dr. Jürgen Schellberg
Korreferent:	Prof. Dr. Uwe Rascher
Tag der mündlichen Prüfung:	19.10.2018

Angefertigt mit Genehmigung der Landwirtschaftlichen Fakultät der Universität Bonn

Zusammenfassung

Das Potenzial von Produktivitätssteigerungen bei Nutzpflanzen wird regelmäßig in agronomischen Feldversuchen untersucht. Eine periodische Erfassung von biophysikalischen Pflanzenvariablen in den oft kleinparzellierten Versuchen ist nötig, um gesicherte Aussagen über die Leistung der Pflanzen treffen zu können. Händische Messungen im Feld sind mühsam, teuer und räumlich eingeschränkt. Unmanned Aerial Vehicle (UAV)-basierte Fernerkundung bietet durch die flexible Einsatzmöglichkeit der Plattform sowie die räumlich und zeitlich hochaufgelösten Sensordaten Potenzial, um Variablen in Feldversuchen schnell, günstig und zerstörungsfrei zu erfassen.

In dieser Dissertation wurde untersucht, ob sich Daten UAV-gestützter, kostengünstiger modifizierter Kompaktkameras dazu eignen, die Variablen *grüner Blattflächenindex (gLAI)* und *Lichtnutzungseffizienz (RUE)* in einem Mais-Feldversuch bei unterschiedlichen Managementeinflüssen zu erfassen. Hierzu wurde in den Jahren 2015 und 2016 auf der universitätseigenen Forschungsstation Campus Klein-Altendorf südwestlich von Bonn ein Feldversuch angelegt, bei dem in vier Behandlungen (zwei Varianten von Stickstoffgabe sowie zwei Varianten von Pflanzdichte) mit jeweils fünf Wiederholungen die Ausbildung von Blattfläche unterschiedlich beeinflusst werden sollte. gLAI und Biomasse wurde destruktiv gemessen, UAV-basierte Daten wurden in ca. 14-tägigen Abständen erhoben, bei denen der gesamte Versuch beflogen wurde. Drei Studien wurden angefertigt, die zur Begutachtung bei internationalen Fachzeitschriften eingereicht wurden.

In Studie I wurden drei ausgewählte spektrale Vegetationsindizes (NDVI, GNDVI, 3BSI) in Beziehung zu den destruktiven gLAI-Messungen gesetzt. Die gefundenen Zusammenhänge pro Behandlungsstufe waren unterschiedlich, aber eindeutig. Die Schätzung von gLAI mithilfe von Zwei-Band-Indizes (NDVI, GNDVI) zeigte gute Ergebnisse bis gLAI-Werte von 3. Der 3-Band-Ansatz (3BSI) zeigte keinerlei Vorteile. Ein Vergleich von statistischen Ergebnissen der gLAI-Messungen und solcher der Indizes führte zur Schlussfolgerung, dass die alleinige Feststellung der Einflüsse von Managementfaktoren auf Blattflächenentwicklung über Vegetationsindizes nicht möglich war.

In Studie II wurden, auf Studie I aufbauend, parametrische und nicht-parametrische

Regressionsmethoden hinsichtlich ihrer Vorhersagefähigkeit in Bezug auf gLAI von Mais evaluiert. Hierzu wurden in den UAV-basierten Bilddaten einmal die Pixel, die keine Pflanzeninformationen enthielten (d.h. schattierter oder sonnenbeschienener Boden) in der Analyse berücksichtigt, ein weiteres Mal nicht. Hinsichtlich der parametrischen Methoden wurden alle möglichen Bänderkombinationen für eine ausgewählte Zahl von Zwei- und Dreiband-Formulierungen sowie verschiedener Anpassungsfunktionen getestet. Hinsichtlich der nicht-parametrischen Methoden wurden sechs Algorithmen (Random Forests Regression, Support Vector Regression, Relevance Vector Machines, Gaussian Process Regression, Kernel Regularized Least Squares, Extreme Learning Machine) getestet. Die Ergebnisse zeigten, dass alle nicht-parametrischen Methoden bessere Vorhersageergebnisse lieferten als die parametrischen, wobei kernel-basierte Algorithmen besonders hohe Genauigkeit erreichten. Der Ausschluss von Pixel ohne Pflanzeninformationen verschlechterte die Leistung der Methoden. Bei parametrischen Methoden war keine Unterscheidung von gLAI-Werten >3 möglich, und keine bei Werten >4 bei nicht-parametrischen Methoden.

In Studie III wurde untersucht, ob a) die Daten der Kameras es erlaubten, die Lichtnutzungseffizienz von Mais in verschiedenen Parzellen des Versuchs von 2016 zu schätzen, b) diese Werte sich von jenen unterschieden, die in anderen Veröffentlichungen zu finden waren und c) ob es Unterschiede zwischen den Werten der RUE-Definitionen RUE_{total} und RUE_{green} gab. Mithilfe der Fernerkundungs-Daten wurden Bedeckungsgrad und Reflektanz geschätzt. Die Werte für RUE_{total} variierten zwischen 4.05 und 4.59, und zwischen 4.11 und 4.65 für RUE_{green}. Im Vergleich mit publizierten Werten sind sie höher, aber noch in einem plausiblen Rahmen. Die Differenz zwischen RUE_{total} und RUE_{green} war minimal, was möglicherweise auf ein verlängertes Grün der Pflanzen (induziert durch das Stay-Green-Merkmal der angebauten Sorte) zurückzuführen ist.

Es lässt sich schlussfolgern, dass UAV-basierte Daten kostengünstiger modifizierter Kompaktkameras sich mit Einschränkung zur Schätzung von gLAI und RUE in Mais-Feldversuchen eignen.

Abstract

The potential for improved crop productivity is readily investigated in agronomic field experiments. Frequent measurements of biophysical crop variables are necessary to allow for confident statements on crop performance. Commonly, in-field measurements are tedious, labour-intensive, costly and spatially selective and therefore pose a challenge in field experiments. With the versatile, flexible employment of the platform and the high spatial and temporal resolution of the sensor data, Unmanned Aerial Vehicle (UAV)-based remote sensing offers the possibility to derive variables quickly, contactless and at low cost.

This thesis examined if UAV-borne modified low-cost camera imagery allowed for remote estimation of the crop variables *green leaf area index (gLAI)* and *radiation use efficiency (RUE)* in a maize field trial under different management influences. For this, a field experiment was established at the university's research station Campus Klein-Altendorf southwest of Bonn in the years 2015 and 2016. In four treatments (two levels of nitrogen fertilisation and two levels of plant density) with five repetitions each, leaf growth of maize plants was supposed to occur differently. gLAI and biomass was measured destructively, UAV-based data was acquired in 14-day intervals over the entire experiment. Three studies were conducted and submitted for peer-review in international journals.

In study I, three selected spectral vegetation indices (NDVI, GNDVI, 3BSI) were related to the gLAI measurements. Differing but definite relationships per treatment factor were found. gLAI estimation using the two-band indices (NDVI, GNDVI) yielded good results up to gLAI values of 3. The 3-bands approach (3BSI) did not provide improved accuracies. Comparing gLAI results to the spectral vegetation indices, it was determined that sole reliance on these was insufficient to draw the right conclusions on the impact of management factors on leaf area development in maize canopies.

Study II evaluated parametric and non-parametric regression methods on their capability to estimate gLAI in maize, relying on UAV-based low-cost camera imagery with non-plants pixels (i.e. shaded and illuminated soil background) a) included in and b) excluded from the analysis. With regard to the parametric regression methods, all possible

band combinations for a selected number of two- and three-band formulations as well as different fitting functions were tested. With regard to non-parametric methods, six regression algorithms (Random Forests Regression, Support Vector Regression, Relevance Vector Machines, Gaussian Process Regression, Kernel Regularized Least Squares, Extreme Learning Machine) were tested. It was found that all non-parametric methods performed better than the parametric methods, and that kernel-based algorithms outperformed the other tested algorithms. Excluding non-plant pixels from the analysis deteriorated models' performances. When using parametric regression methods, signal saturation occurred at gLAI values of about 3, and at values around 4 when employing non-parametric methods.

Study III investigated if a) UAV-based low-cost camera imagery allowed estimating RUEs in different experimental plots where maize was cultivated in the growing season of 2016, b) those values were different from the ones previously reported in literature and c) there was a difference between RUE_{total} and RUE_{green}. Fractional cover and canopy reflectance was determined based on the RS imagery. Our study showed that RUE_{total} ranges between 4.05 and 4.59, and RUE_{green} between 4.11 and 4.65. These values were higher than those published in other research articles, but not outside the range of plausibility. The difference between RUE_{total} and RUE_{green} was minimal, possibly due to prolonged canopy greenness induced by the stay-green trait of the cultivar grown.

In conclusion, UAV-based low-cost camera imagery allows for estimation of plant variables within a range of limitations.

Contents

List of Abbrevations

3BSI	3-Band Spectral Index
ANOVA	Analysis of Variance
APAR	Absorbed Photosynthetically Active Radiation
CFA	Color Filter Array
CKA	Campus Klein-Altendorf
COTS	Commercial Off-The-Shelf Cameras
BRDF	Bidirectional Reflectance Distribution Function
BRD	Bidirectional Reflectance Factor
DN	Digital Number
ELM	Extreme Learning Machine
fAPAR	Fraction of absorbed PAR
GAI	Green Area Index
GCP	Ground Control Point
gLAI	Green Leaf Area Index
GPS	Global Positioning System
GSD	Ground Sampling Distance
GNDVI	Green Normalized Difference Vegetation Index
GPR	Gaussian Process Regression
IR	Infrared
KRLS	Kernel Regularized Least Squares
KRR	Kernel Ridge Regression
LAI	Leaf Area Index
LUT	Lookup Table
N	Nitrogen
ND	Normalized Difference
NDVI	Normalized Difference Vegetation Index
NIR	Near-Infrared
PAR	Photosynthetically Active Radiation
PD	Plant Density
RF	Random Forest
RGB	Red, Green and Blue Bands
RMSE	Root Mean Square Error
RS	Remote Sensing
RSS	Residual Sum of Squares

RTK	Real Time Kinematic
RTM	Radiative Transfer Model
RUE	Radiation Use Efficiency
RVM	Relevance Vector Machines
SfM	Structure from Motion
SR	Simple Ratio
SVI	Spectral Vegetation Index
SVR	Support Vector Regression
UAV	Unmanned Aerial Vehicle
UV	Ultraviolet Spectrum
VIS	Visible Spectrum

List of Figures

List of Tables

1 Introduction

With an anticipated world population of 9 billion people by the year 2050, impacts of climate change and limited availability of arable land and fresh water, agriculture faces great challenges to ensure global food security through increasing yields, while simultaneously reducing environmental costs (Cui et al., 2016; Fedoroff et al., 2010).

The potential for improved crop productivity is readily investigated in scientific experiments, which aim at finding the optimal agricultural conditions by varying management factors, in possible combination with the modification of the genetic composition of crop varieties (Maat, 2011). Results from controlled environments (e.g. greenhouse or growth chamber), however, are distinct from the actual situations that plants experience in the field and therefore difficult to extrapolate to conditions outside of these (Araus and Cairns, 2014; Yang et al., 2017). For simulation of the 'real world cropping system', scientists turn to field experiments where the crop response to different factors can be evaluated under natural conditions.

The biophysical crop variables selected for evaluation should be measured frequently, simultaneously and in various locations to allow for confident statements on crop performance. Commonly, in-field measurements are tedious, labour-intensive, costly and spatially selective, and therefore pose a challenge in field experiments.

Satellite-based remote sensing (RS) has become an extremely useful technology for collecting data for various agricultural applications over larger areas (Sankaran et al., 2015). The high cost, susceptibility to cloud coverage, long revisit periods and the lack of spatial resolution, however, limit its applicability in field experiments, since plot sizes are commonly below the spatial resolution of spaceborne sensors (Yang et al., 2017). It is furthermore difficult to compare the satellite data with in-field ground measurements, because processes may display a finer-scale heterogeneity (Brüser et al., 2014).

The ongoing advancement of Unmanned Aerial Vehicle (UAV)-based RS has

opened up new opportunities in agronomic research. The versatile, flexible employment of the platform and the high spatial resolution of the sensor data enables researchers to monitor crop development with unprecedented temporal resolution and great spatial detail.

With ground sampling distances (GSD) ranging from millimetres to centimetres, this data can add value to field experiments, as biophysical plant variables can be captured non-destructively, frequently and rapidly over a larger amounts of plots (Rasmussen et al., 2016; Zaman-Allah et al., 2015). Yet, the high procurement cost of the UAV-carried sensors puts constraints on the applicability of this data in experimental research. Commercial off-the-shelf (COTS) digital camera imagery with a similar information content, commonly derived from cameras that cost only a fraction of sensors developed for scientific use, might provide an alternative. This, however, comes at the expense of data certainty, given that specifications of COTS cameras are rarely documented in great detail (Berra et al., 2015).

Maize (*Zea mays L.*) is one of the three major cereal crops in the world, besides wheat and rice (Tollenaar and Wu, 1999). First cultivated by farmers in Mexico 7000 to 10,000 years ago, it has spread around the globe ever since, with the three countries USA, China and Brazil accounting for more than 75% of today's worldwide production (Ranum et al., 2014). Its grain is a major staple food in several countries of Central and Latin America, Eastern and Southern Africa as well as Southeast Asia, whereas it is mainly grown for animal fodder (both grain and residual biomass for silage) and energy production (ethanol, biogas) in the rest of the world (Ranum et al., 2014; Shiferaw et al., 2011). Through plant breeding, the plant has adapted to the growing conditions of temperate regions, which is why it is widely found under cultivation on German fields. Given the importance of the maize crop in the agricultural production worldwide, increases in productivity are central to efforts concerning food security and reduction of worldwide carbon emissions.

The green leaf area index (gLAI) and the radiation use efficiency (RUE) are important variables for crop growth analysis since they ultimately indicate crop productivity. Several studies have shown that RS allows for remote estimation of gLAI, RUE and other variables in maize based on large-scale multispectral satellite data (e.g. Dong et al. (2017); González-Sanpedro et al. (2008); Kira et al. (2017); Kross et al. (2015)).

However, until lately no attention has been paid to the UAV-based estimation of gLAI and RUE in maize in small-scale experimental plots.

2 Objectives of Study

The estimation of biophysical crop variables over larger areas via satellite-based RS is well-explored and well-documented in scientific literature. The rise of UAV-based RS, however, has opened up new opportunities, given the high spatial resolution of the data and the versatile employment of the platform.
We[1] were interested in the potentials of UAV-based COTS camera imagery for estimating gLAI and RUE in a controlled biannual maize field experiment located at Campus Klein-Altendorf (CKA), one of the university's agricultural research stations located southwest of Bonn.
The objectives of this study therefore were:

i To generally evaluate if UAV-based COTS camera imagery can be used to estimate gLAI and RUE of maize in a biannual field experiment consisting of small plots of different treatments;

ii To particularly locate potentials and limitations in gLAI estimation accuracy using different regression methods and different band combinations;

iii To explore if improving estimations of gLAI is possible by excluding non-relevant information present in the ultra-high spatial resolution data;

iv To explore if it is possible to rely entirely on the RS data to analyse the effects of different treatments on leaf area development.

The data that provides the basis for this study was collected in the years 2015 and 2016, and was subsequently analysed with regard to the study objectives listed above. Three manuscripts were prepared and submitted for publication in scientific journals.
The main part of this thesis is structured as follows:

[1] The three studies in chapters 5, 6 and 7, submitted for publication, and forming the core part of this thesis were written in collaboration with my first supervisor PD Dr. Jürgen Schellberg. To conform with the formulations of those chapters, the term 'we' will be used throughout the entire thesis. However, I would like to point out that all other chapters are solely my own intellectual product.

Chapter 3 provides a general overview of the basic concepts of vegetation RS, RS-based estimation of biophysical plant variables, UAV-based RS and the handling of COTS camera imagery,

Chapter 4 presents a detailed look into the study area, the image acquisition workflow and the preprocessing of the images ahead of the analysis,

Chapter 5 examines the relationship between three selected spectral vegetation indices (NDVI, GNDVI, 3BSI) derived from UAV-based COTS imagery and the field-based gLAI measurements. It furthermore compares gLAI results of different treatments with those of the corresponding spectral vegetation indices,

Chapter 6 evaluates parametric and non-parametric regression methods on their capability to estimate gLAI in maize, relying on imagery with non-plants pixels (i.e. shaded and illuminated soil background) a) included in and b) excluded from the analysis,

Chapter 7 investigates if a) UAV-based COTS camera imagery allowed estimating RUEs in different experimental plots where maize was cultivated in the growing season of 2016, b) those values were different from the ones previously reported in literature and c) there was a difference between RUE_{total} and RUE_{green}.

This chapter was peer-reviewed and published as:

Tewes, A., Schellberg, J., 2018*. Towards Remote Estimation of Radiation Use Efficiency in Maize Using UAV-Based Low-Cost Camera Imagery. Agronomy 8, 16. https://doi.org/10.3390/agronomy8020016*

Chapter 8 summarizes the main results of this thesis in relation to the research questions. It furthermore discusses the overall limitations of the findings, and provides an outlook for future research.

3 State of Research

3.1 The Basic Concepts of Remote Sensing of Vegetation

RS techniques are increasingly contributing valuable information for the study of vegetation systems and their functioning. Of particular advantage is that they are contactless and non-destructive, and observations can easily be extrapolated to larger scales (Jones and Vaughan, 2010). With the gathering of information at a distance as the central concept, it has evolved into a discipline that is applied by a range of scientists in different fields such as agriculture, archaeology, forestry, geography or geology. RS uses electromagnetic radiation in one or more regions of the electromagnetic spectrum to derive information (see figure 3.1), reflected or emitted from the objects of interest (Campbell and Wynne, 2011). Knowledge about the properties of that radiation and its interaction with the object as well as the atmosphere through which it travelled and the detecting sensor allows for correct interpretation by the analyst (Campbell and Wynne, 2011; Jones and Vaughan, 2010). The electromagnetic spectrum describes the continuum of electromagnetic waves of all existing frequencies and wavelengths. The sun produces a full spectrum of electromagnetic radiation, which passes through the atmosphere before reaching the surface of the earth. A part of it is reflected, another part is absorbed and then re-radiated as thermal energy. The spectrum is commonly divided into regions, with the optical spectrum (from 0.3 μm to 15 μm) defined as those wavelengths that can be reflected and refracted with lenses and mirrors, and the reflective spectrum (from 0.38 μm to 3 μm) defined as the portion of the solar spectrum that is used directly for RS (Campbell and Wynne, 2011; Jones and Vaughan, 2010). The visible (VIS) spectrum constitutes only a small portion of the spectrum (0.4 to 0.7 μm), but is of great importance in RS of vegetation, since it approximately corresponds with the photosynthetically active region (PAR). The infrared (IR) region, which is partitioned into the near-infrared

(NIR, 0.7-1 μm), the mid-infrared (MIR, 1-4 μm), the thermal infrared (TIR, 4-15 μm) and the far infrared (15-100 μm) is found on the longer-wavelength side (Jones and Vaughan, 2010). Radiation in the NIR region behaves, with regard to optical systems, in an analogous manner to radiation in the visible spectrum. This implies that films, filters and cameras with similar designs to those intended for use with visible light can be used (Campbell and Wynne, 2011). Microwaves are the longest wavelengths commonly used in RS, ranging from 1 mm to 1 m in length. These can be sensed passively, but most RS in the microwave region uses radiation that is artificially generated (Jones and Vaughan, 2010).
The spectral resolution of most remote sensing systems can be described in terms of number and width of the bands of the electromagnetic spectrum (Jensen, 2007). Figure 3.1 shows the most important wavelength ranges of the bands used in RS, and the corresponding parts of the spectrum that are covered.

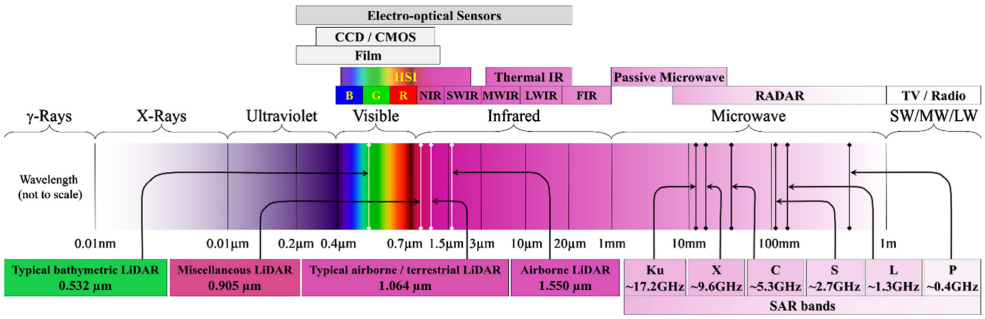

Figure 3.1: Electromagnetic spectrum with important remote sensing bands. Source: Toth and Jóźków (2016)

For more information on the basic concepts of RS, the interested reader is referred to introductory literature such as Campbell and Wynne (2011), Jensen (2007), Lillesand (2000) or Jones and Vaughan (2010).

3.1.1 Remote Sensing Instruments and Platforms

RS is a quickly advancing technology, where the progress is mainly driven by imaging sensor developments and the increasing performance of the information infrastructure, including processing, storage and communication (Toth and Jóźków, 2016). Science can nowadays benefit from a large variety of RS data provided by different passive and active RS instruments carried by range of platforms (the components acting together is referred to as *RS system*), ranging from the early aerial camera to the modern hyperspectral scanner (Homolová et al.,

2013; Jones and Vaughan, 2010). Additionally, new sensor-carrying platforms are introduced and continuously improved. Especially Unmanned Aerial Vehicles (UAV) have seen unprecedented development in recent times (Colomina and Molina, 2014; Pajares, 2015). The choice of sensor for a particular purpose depends on a number of factors, such as the use to which the data will be put, the most suitable wavelength of electromagnetic radiation, the frequency at which the observation is required, and the scale and variability in the scene observed (Jones and Vaughan, 2010). Current operating RS systems can provide a wide variety of spatial, spectral and temporal resolutions, with the majority being imaging instruments.

The purpose of the platform is to position the sensor over the area of interest; the choice may affect the spatial and temporal resolution of the data obtained. The requirements of the desired measurements therefore determine the selection of the platform (Jones and Vaughan, 2010). Typical ones comprise static and 'within-field' platforms, UAVs, aircrafts and spaceborne satellites, each platform exhibiting different operational parameters (see table 3.1). The prevailing systems used in vegetation studies are optical, passive systems. These optical spectroradiometers aboard satellite-, airborne- and ground-based platforms represent a trade-off between spatial, spectral and temporal resolutions. The electromagnetic spectrum is commonly sampled only with a few spectral bands (Homolová et al., 2013).

Belward and Skøien (2015) provide an overview over satellites under civilian and/or commercial control with the potential to gather global land-cover observations, Toth and Jóźków (2016) present a review of state-of-the-art remote sensing technologies, including platforms and sensors. Besides the introductory books listed above, the interested reader is referred to these publications for further information.

3.1.2 Radiative Properties of Leaves and Canopies

The radiative properties of a plant canopy as a whole and its components (leaves, stems, soil, water) are fundamental principles to the understanding of remote sensing of vegetation in general and remote sensing of crops in particular. The interaction of radiation with plant leaves and the resulting magnitudes of spectral reflectance (ρ_λ), spectral absorption (α_λ) and spectral transmission (α_τ) does not only depend on the wavelength, but also on a range of structural and chemical

Table 3.1: Typical sensor and platform configurations with main operational parameters. MS: Multispectral, HSI: Hyperspectral Image, LiDAR: Light Detection and Ranging, SAR: Synthetic Aperture Radar. Source: Toth and Jóźków (2016, modified)

Applicability and operation aspects	Data acquisition platforms			
	Satellite	Airborne	UAV	Static
Maneuverability	No/limited	Moderate	High	Limited
Observation space	Worldwide	Regional	Local	Local
Sensor diversity	MS / HSI / SAR	MS / HSI / LiDAR / SAR	MS / LiDAR / HSI	MS / LiDAR / HSI
Environment	Outdoors	Outdoors	Outdoors/Indoors	Outdoors/Indoors
Scale (inverse sensor range)	Small	Small/Medium	Medium/Large	Medium/Large
Ground Coverage	Large (10km)	Medium (1km)	Small (100m)	Small (50m)
FOV	Narrow	Wide	Wide/Super Wide	Wide/Super Wide
Repeat Rate	Day	Hours	Minutes	Minutes
Spatial Resolution (GSD)	0.3-300 m	5-25 cm	1-5 cm	1-5 cm
Spatial Accuracy	1-3m	5-10cm	1-25cm	3-50cm
Deployability	Difficult	Complex	Easy	Moderate
Observability	Vertical/Oblique	Vertical / Oblique	Vertical / Oblique / 360	Oblique / 360
Operational Risk	Moderate	High	Low	Moderate
Cost	$$$$$	$$$	$	$$

characteristics (see Figure 3.2 for a typical spectrum of healthy green vegetation) (Jones and Vaughan, 2010). All leaves absorb a large proportion of incident radiation in the visible wavelength. This is largely determined by photosynthetic pigments (especially chlorophyll, but also carotenoids and flavonoids) found in the palisade layer of the leaf. Chlorophyll absorbs sunlight for photosynthesis, preferentially in the blue and red part of the spectrum (Figure 3.3), with as much as 70% to 90% of the incident light. Less light is absorbed in the green region due to the gap in the absorption spectrum of chlorophyll a and b, which is why foliage appears green to the human eye (Figure 3.3) (Campbell and Wynne, 2011; Jensen, 2007). Radiative properties of other pigments are usually masked by the dominance of chlorophyll absorption, and only emerge during leaf senescence or environmental stress, when chlorophyll concentration decreases (Jensen, 2007). Relatively little radiation is absorbed in the infrared, where radiative properties are controlled by the structure of the spongy mesophyll tissue, not by plant pigments (Figure 3.3) (Campbell and Wynne, 2011). Mesophyll tissue is composed

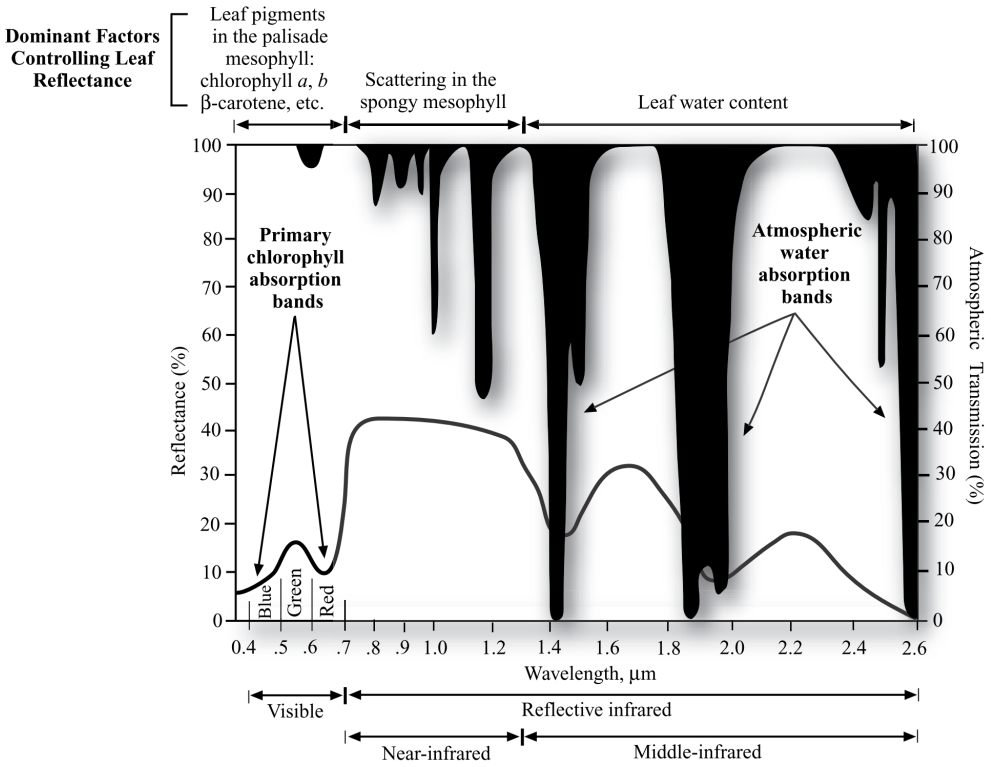

Figure 3.2: Typical spectral reflectance characteristics for healthy green vegetation for the wavelength interval from 400 nm to 2,500 nm. Source: Jensen (2007)

of many cells and intercellular air spaces that result in highly diffuse reflectance (40% to 60%) and transmittance (40% to 60%) of light especially in the near-infrared (NIR) (Campbell and Wynne, 2011; Jensen, 2007). The sharp rise of reflectance between the red and NIR region is called red-edge.

Reflection of radiation from canopies depends both on the radiative properties of the individual components of the vegetation (i.e. leaves, stems, soils, water, etc.), and on the detailed canopy architecture or spatial organisation (i.e. average leaf angle) in relation to the orientation of the sensor and the angular distribution of the incident radiation (Jones and Vaughan, 2010). Measured reflectance therefore is a result of the interactions of those components (Figure 3.4), and is considerably lower than reflectances measured for individual leaves (approx. 10% for a single leaf and approx. 3-5% for a canopy in the visible region, approx. 50% for a single leaf and approx. 35% for a canopy in the near-infrared) (Campbell and Wynne, 2011). This is because much of the light has undergone more than one reflection. The relative lower decrease in the NIR than in the VIS is

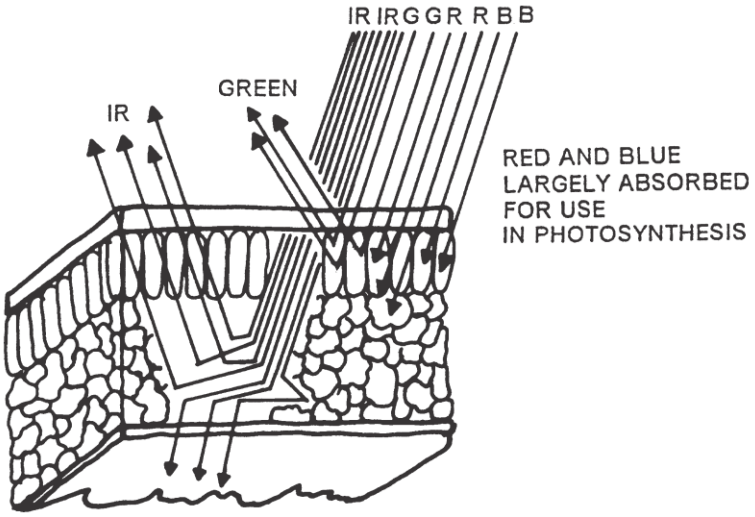

Figure 3.3: Interaction of leaf structure with visible and infrared information. Source: Campbell and Wynne (2011)

due to the leaf additive reflectance, where both the high reflectance and transmission lead to an enrichment of the signal with increasing depth of the canopy (Jensen, 2007; Jones and Vaughan, 2010). The mechanisms that influence leaf reflectance are in general well understood, but the interpretation of reflectance at canopy level remains challenging due to to the multiple light interactions between canopy elements and the background (Homolová et al., 2013). The leaf area index (LAI) is the most important plant variable determining radiation absorption and transmission by canopies. It is defined as the total one-sided area of leaf tissue per unit ground surface area (Bréda, 2003), and frames the area that interacts with radiation and therefore provides the signal captured by remote sensing. In a homogeneous canopy where absorbing components are evenly distributed and small in comparison with the size of the canopy, spectral absorption can be approximated by the Beer's law (Equation 3.1):

$$I = I_0 e^{-kL}, \tag{3.1}$$

where I_0 is the irradiance above the canopy, I the irradiance at a point in the canopy above which there is a leaf area index of L. k is the dimensionless extinction coefficient that determines the rate of attenuation through the canopy, largely influenced by leaf-angle distribution (Hay and Porter, 2006; Jones and Vaughan, 2010).

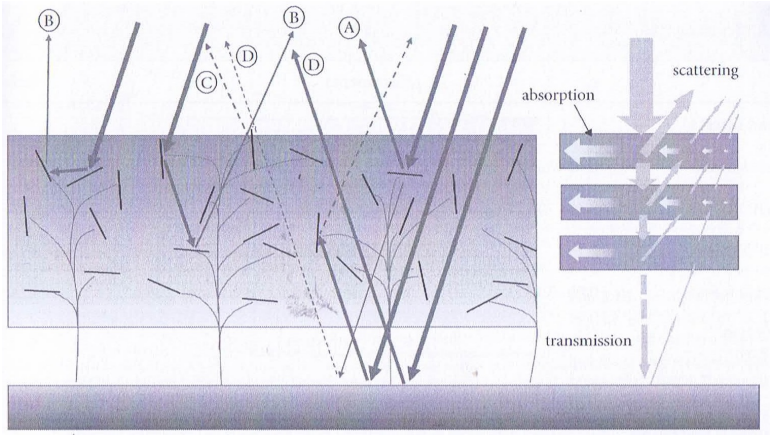

Figure 3.4: Illustration of possible interactions of radiation with a plant canopy (left). Leaves are randomly oriented, showing varying scattering events. (A) shows incident sunlight directly reflected back to the sky, (B) a small fraction that is transmitted through the leaf is reflected from a second leaf, or (C) even a third. Some light is reflected from the soil (D). The right illustration shows a simplification, where the canopy is treated as a set of thin layers. The downward radiation is attenuated by absorption and scattering at each layer, while the upward radiation is the sum of all upwardly scattered radiation. Source: Jones and Vaughan (2010)

3.2 Remote Sensing-Based Estimation of Biophysical Crop Variables

Over the course of the years, a variety of methodologies have been developed to estimate crop variables based on optical RS data. They rely on measurements from the visible to shortwave infrared spectral region, and sensors stretching from digital cameras to full-range spectroradiometers. In their review paper, Verrelst et al. (2015a) developed a categorisation that binned retrieval methods into four groups:

i Parametric regression methods,

ii Non-parametric regression methods,

iii Physically-based methods and

iv Hybrid methods.

The four groups are briefly reviewed below.

3.2.1 Parametric Regression Methods

Parametric regression methods have been the most popular approach to estimate biophysical variables of vegetation using optical RS. Commonly, a parameterized expression relates one or several spectral bands to the variable of interest (e.g. field measurements) via a fitting function. This fitting function may be either linear or non-linear (e.g. exponential, power or x-order polynomial). Figure 3.5 shows a generalized procedure for parametric regression. Homolová et al. (2013) state that these methods are computationally fast and may work well for the particular area and sensor of interest, but lack cause-effect relationships. As a result, the statistical relationships suffer from lack of robustness and transferability, as they are site, species and time specific (Homolová et al., 2013).

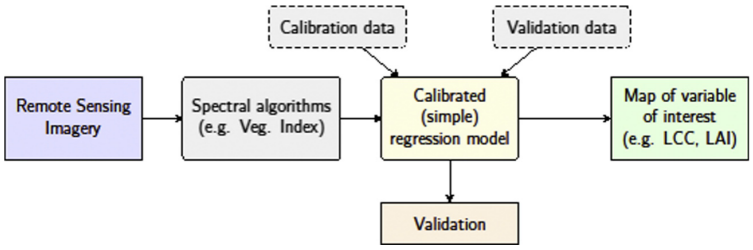

Figure 3.5: Flowchart of a generalized procedure of parametric regression methods. Source: Verrelst et al. (2015a)

The contrast between visible and NIR vegetation canopy reflectance has resulted in the development and investigation of a number of spectral vegetation indices (SVI), facilitating the estimation of certain biophysical variables due to the higher information content than either visible or near-infrared measurements exhibit alone (Jensen, 2007). SVIs are dimensionless measures derived from radiometric data, with the use to indicate the amount of green vegetation present in the sensor's view. The vast majority is based on the sharp increase in reflectance between the visible and the NIR spectrum. They are most commonly used when the relationship is based on data from sensors that deliver only a limited number of broad spectral bands (e.g. multispectral sensors mounted on satellites or aerial vehicles). SVI-based approaches are the most popular because they are simple, easy to understand, and well-documented for a number of vegetation variables (see figure 3.6 for an example, where the LAI of wheat is related to the NDVI). Over the years, many SVIs have been developed. They can be categorized according to their mathematical definition (Verrelst et al., 2015a):

- Two-band SVIs, which comprise the vast majority of indices reported, such as the simple ratio (SR), the normalized difference vegetation index (NDVI), the green normalized difference vegetation index (GNDVI), the soil adjusted vegetation index (SAVI) or the wide dynamic range vegetation index (WDRVI).

- Three-band SVIs, such as the enhanced vegetation index (EVI), the triangular VI (TVI) or the modified chlorophyll absorption in reflectance index (MCARI).

- Four or more band SVIs, which typically combine two SVIs such as the TCARI/OSAVI.

SVIs have been widely developed and used for data delivered by sensors with a limited amount of spectral bands (e.g. most satellite-based multispectral sensors), but are increasingly used in hyperspectral RS as well. Reducing those larger datasets into simple SVI formulations might lead to the situation that parts of the information remain unexploited. Decisions on band selection, index formulation and fitting function should therefore be carefully made (Verrelst et al., 2015a).

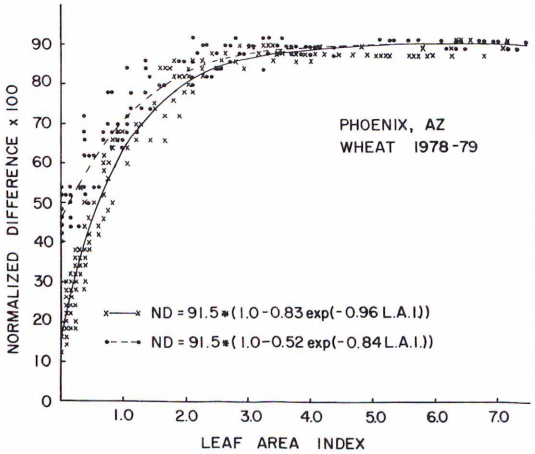

Figure 3.6: An example for parametric regression. Here, the relation between the normalized difference and LAI is examined. The solid line shows the relation for the growth period, the dashed line the relation for the senescence period. Source: Asrar et al. (1984)

3.2.2 Non-Parametric Regression Methods

Non-parametric regression methods have evolved in RS-based estimation of biophysical crop variables due to the development and adaptation of sophisticated learning models to regression challenges. Based on training data, they minimize the estimation error of the variables by adjustment of weights (coefficients) (Verrelst et al., 2015a). An important advantage over parametric regression methods is the use of all spectral bands offered by the sensor (i.e. the full spectrum in case of a hyperspectral measurement), with no explicit selection needed. Complex associations (e.g. non-linear relationships) between the variable of interest and a potentially unlimited number of explanatory predicting variables can be featured without the explicit knowledge of the underlying processes (Houborg and McCabe, 2018). Model over-fitting is prevented by defining model weights through a combination of training set approximation error minimisation while limiting model complexity (Verrelst et al., 2015a). Typical learning approaches include decision trees (e.g. random forests), artificial neural networks, kernel-based algorithms (e.g. support vector machines) and Gaussian process regression (Houborg and McCabe, 2018). A scheme of a generalized non-parametric regression workflow is illustrated in figure 3.7.

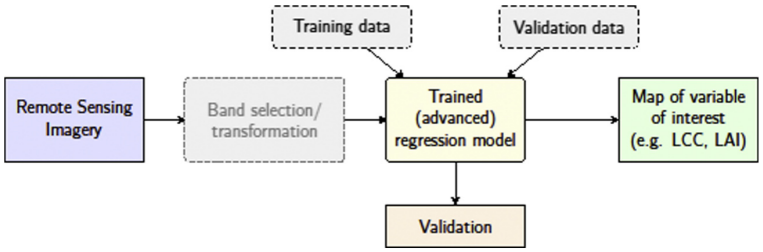

Figure 3.7: Flowchart of a generalized procedure of non-parametric regression methods. Contrary to parametric regression, the band selection/transformation is optional. Source: Verrelst et al. (2015a)

3.2.3 Physically-Based Methods

Physically-based methods rely on the inversion of models that establish cause-effect relationships based on physical laws (Verrelst et al., 2015a). They commonly make use of radiative transfer models (RTMs), which simulate light absorption and scattering inside a vegetation canopy, thereby accounting for leaf biochemical composition and canopy structural properties (Homolová et al., 2013).

Physically-based methods were not in focus of this study; they are mentioned here for the sake of completion. Thus, we refrain from further elaboration. Additional information on this topic is available in the review paper of Verrelst et al. (2015a) or chapter 8 of Jones and Vaughan (2010).

3.2.4 Hybrid Methods

Hybrid methods combine elements of the flexible, computationally-efficient non-parametric methods with physically-based methods, which offer advantages in their generalization levels. In this inverse mapping approach, radiative transfer model-simulated data is used to train a non-parametric model. Contrary to the physically-based approaches, the hybrid methods make use of all available data, and not just the simulated spectrum closest to the measured one.
Hybrid methods were also not in focus of this study, the interested reader is referred to Verrelst et al. (2015a) for a review of publications investigating this approach.

3.3 UAV-Based Remote Sensing

The integration of unmanned aerial vehicles (UAV) into the field of RS unfolded quickly and has had major impacts in the last years, perhaps best expressed by the increase of scientific publications documenting UAV-related RS research (see Cummings et al. (2017) for analysis), the organisation of UAV-devoted conferences such as the biannual ISPRS International Conference on Unmanned Aerial Vehicles in Geomatics (UAV-g), by special issues in well-established scientific journals (e.g. 'UAV-Based Remote Sensing Methods for Modeling, Mapping, and Monitoring Vegetation and Agricultural Crops' or 'Recent Trends in UAV Remote Sensing' in *Remote Sensing*, 'Unmanned Aerial Vehicles for Environmental Applications' in *International Journal of Remote Sensing* and 'Small Unmanned Aerial System Development and Applications in Precision Agriculture and Natural Resource Management' in *European Journal of Remote Sensing*) or the creation of scientific journals such as *Drones* (MDPI AG, Basel, Switzerland) or *Journal of Unmanned Vehicle Systems* (NRC Research Press, Ottawa, Canada).
The application of UAVs in recent years has evolved rapidly due to advancements and price declines in electronics, optics, computer science, batteries, among others (González-Jorge et al., 2017).

There are various acronyms and names under which UAVs are also described, such as *UAS* (Unmanned Aerial System), *drone*, *aerial robot*, or *RPAS* (Remotely-Piloted Aerial System) (Colomina and Molina, 2014). The term UAS describes the entire system comprising the unmanned vehicle, the ground control station and a communications data link for command and control of the vehicle, whereas the term UAV only the vehicle (Colomina and Molina, 2014). Most scientific publications indeed cite the term UAV (Cummings et al., 2017). Whatever the acronym used, they commonly refer to vehicles with flying capacity without any person onboard, able to fly autonomously or fly remotely controlled (Pajares, 2015; Sankaran et al., 2015). In practice, both fixed and rotating wing solutions (or rotocopter) are used (see figure 3.8 for photos). Fixed-wing solutions generally offer longer flying times for the same payload. In contrast, rotating-wing solutions, such as quadcopter, hexacopter or octocopter provide better manoeuvrability and need little space for take off and landing (Toth and Jóźków, 2016). The flying height controls the spatial resolution of the sensor, the maximum area

Figure 3.8: Types of Unmanned Aerial Vehicles. Source: Sankaran et al. (2015)

covered is mainly defined by the available onboard power, the flight regulations in the area and the communication range between the UAV and the operator (Toth and Jóźków, 2016).

Nowadays, UAV versions of all sensors carried on traditional RS systems are available on the market (Cummings et al., 2017). These comprise LiDAR (Lin et al., 2011; Wallace et al., 2012), multispectral cameras (Berni et al., 2009; Verger et al., 2014; Zhou et al., 2017), hyperspectral cameras (Aasen et al., 2015; Yue et al., 2017), spectrometers (Burkart et al., 2015; von Bueren et al., 2015) and thermal cameras (Berni et al., 2009; Gonzalez-Dugo et al., 2013). The majority of studies published on UAV-based environmental research, however, have utilized COTS

digital cameras, which combine good image performance with light payload and cheap procurement cost (Cummings et al., 2017). This type of sensor was also employed in this study. A general overview is presented in section 3.4.
For further information on UAV-based RS, the reader is referred to the excellent reviews by Zhang and Kovacs (2012), Colomina and Molina (2014), Salamí et al. (2014), Pajares (2015), Sankaran et al. (2015), Yang et al. (2017) and González-Jorge et al. (2017).

3.4 Modified Commercial Off-The-Shelf Digital Cameras as Low-Cost Solution

3.4.1 Introduction to COTS Cameras

Commercial off-the-shelf digital cameras (COTS) are increasingly used for research in vegetation-related sciences, due to their low cost, easy operation, light weight, compact size and compact data storage, as well as their possibility to sense NIR light after modification of the body (Rabatel et al., 2014). COTS cameras may be employed with the original characteristics (unaltered), or they may be modified to detect NIR radiation (Verhoeven et al., 2009).
UAV-based COTS applications in crop science comprise crop height estimation (Chu et al., 2016; De Souza et al., 2017; Geipel et al., 2014; Holman et al., 2016; Li et al., 2016; Schirrmann et al., 2017), biomass estimation via canopy height (Bendig et al., 2014, 2015; Li et al., 2016; Maresma et al., 2016), biomass estimation via vegetation indices (Schirrmann et al., 2016; Vega et al., 2015), analysis of phenology (Burkart et al., 2017), LAI estimation (Córcoles et al., 2013; Hunt et al., 2010; Lelong, 2008), yield prediction (Haghighattalab et al., 2017; Maresma et al., 2016; Zhou et al., 2017), crop and weed mapping and classification (Calvario et al., 2017; Castaldi et al., 2016; Yang et al., 2014; Zhang et al., 2016), canopy cover (Chu et al., 2016; Liebisch et al., 2015; Torres-Sánchez et al., 2014; Yang et al., 2014), assessment of field conditions (Gnädinger and Schmidhalter, 2017; Khot et al., 2016) plant vigor and stress assessment (Gago et al., 2015; Ren et al., 2017b) and plant density estimation (Jin et al., 2017).
COTS cameras are typically fitted with either a CCD (Charge Coupled Device) or a CMOS (Complementary Metal Oxide Semiconductor) sensor, where the silicon-based sensor substrate is inherently sensitive to electromagnetic ra-

diation in the wavelengths between 350 nm and 1100 nm, including ultraviolet (UV) and NIR (Nijland et al., 2014). Most digital cameras use a Bayer pattern array of filters to obtain red, green and blue bands for a digital image (see below for a detailed explanation) (Hunt et al., 2010). Along with VIS radiation, these filters transmit UV and NIR radiation, which is why cameras are fitted with an internal hot-mirror filter blocking these wavelengths (Hunt et al., 2010; Nijland et al., 2014). If the rejection filter is removed, the transmission profiles of the Bayer filters remain, and each band is sensitive to its original colour and NIR radiation (Nijland et al., 2014). If the hot-mirror filter is replaced by a filter that allows transmittance of NIR light and selected regions of the visible spectrum, it is possible to acquire NIR-only information in one band. Available filters comprise the following, with a number of commercial companies (e.g. Life Pixel Infrared, Mukilteo, WA, USA; LDP LCC Inc., Carlstadt, NJ, USA; Optik Macario GmbH, Mönchengladbach, Germany; DSLR AstroTEC, Engen, Germany) and do-it-yourself online guides (e.g. `https://publiclab.org/wiki/near-infrared-camera`, accessed December 22, 2017 or `http://www.instructables.com/id/infrared-digital-camera---the-real-way/`, accessed December 22, 2017) offering the conversion:

- 550 or 590 nm long-pass filter giving R = Red + NIR, G = Green + NIR and B = NIR only,
- Dual-band-pass filter that transmits light only in the 400-600 nm and 700-800 nm domains, giving R = NIR only, G = Green and B = Blue,
- NIR only (>700 nm long pass), where all bands have NIR-only sensitivity, but with a wider range in R than in B and G,
- Monotone NIR-only filter, with a more or less same NIR sensitity in all bands (Nijland et al., 2014).

Unfortunately, the filter choice influences the spectral sensitivity and dynamic range of the sensor, resulting in large exposure differences between the bands and possibly causing loss of dynamic range (Nijland et al., 2014). The challenge when employing COTS (modified or unmodified) however is that neither of those are optimized for accurate radiance capture in a scientific context, but rather to produce images that appear pleasing to the human eye. The internal image processing firmware introduces nonlinearities through brand- and model-specific

operations that may change colour, contrast and white balance of the images. Subsequently, the images are transformed to a nonlinear RGB space and compressed in a lossy, irreversible fashion (Figure 3.9) (Akkaynak et al., 2014). Thus, without control over the alteration of image information in a black-box camera system, scientists may compromise data quality and repeatability (Akkaynak et al., 2014).

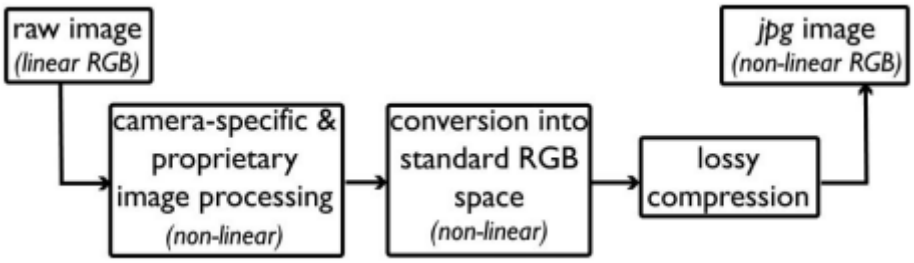

Figure 3.9: Basic image processing pipeline in a consumer camera. Source: Akkaynak et al. (2014)

3.4.2 Working with RAW Imagery

The RAW format commonly exhibits a linear relationship to scene radiance, contrary to the compressed, widely-used JPG format (Akkaynak et al., 2014). A RAW file is the analogue sensor information that was amplified and converted to digital data, without being subjected to any major processing by the camera's firmware (Verhoeven, 2010).

The most widespread method to give colour sensitivity to a camera's sensor is the use of a colour filter array (CFA). A CFA is a mosaic pattern of coloured filters that is positioned on top of the sensor, allowing only specific spectral wavelengths to be collected by the photodiodes. Nowadays, almost all sensors have a Bayer colour filter array, which combines a red, a blue and two green sensor cells (to mimic the higher sensitivity to green light by the human visual system and enlarge the perceived sharpness of the digitally recorded scene) into one true-colour image pixel (Nijland et al., 2014; Verhoeven, 2010). The filters are characterized by their spectral sensitivity, which is unique to every make and model (i.e.two different cameras record different RGB values for the same scene) (Akkaynak et al., 2014). Camera manufacturers typically do not publish this information (Berra et al., 2015). Scientists may therefore either measure or estimate the sensitivity, commonly by taking photographs of monochromatic light produced by a

monochromator (Darrodi et al., 2015). Figure 3.10 shows the spectral response curves from three different unmodified RGB cameras. The analysis of both shape and intensity of the curves shows differences among the camera models (Berra et al., 2015).

Because each pixel senses only one spectral component, an algorithm is needed to estimate the missing colour values (Lebourgeois et al., 2008; Verhoeven, 2010). This interpolation process is also known as demosaicking or CFA colour interpolation (Lebourgeois et al., 2008). A broad range of algorithms (linear and non-linear) with varying complexity and computational demand have been developed in recent years, which give the users the choice (and possibly confusion) to select a specific one according to the data source (Verhoeven, 2010). Verhoeven (2010) tested different demosaicking algorithms and found the AHD (Adaptive Homogeneity-Directed) algorithms to be the best suited for digital NIR imagery. Unfortunately, RAW unprocessed data contains modifications that may occur during the collection, processing and transmission of the data by the sensor system, which are otherwise removed by the in-camera firmware, and that include processes that either introduce unwanted additional measurements or directly alter the strength or spatial properties of the incoming radiance (especially vignetting and lens distortion) (Kelcey and Lucieer, 2012).

Vignetting is defined as a spatially dependent light intensity fallof that results in a progressive radial reduction in radiance strength towards the edges of the image (Kelcey and Lucieer, 2012). The primary mechanism arises from differences in irradiance across the image plane due to the optical properties of the camera lense. The occlusion of light is increased by widening angles, leading to a radial shadowing effect as illumination is reduced (Kelcey and Lucieer, 2012; Lebourgeois et al., 2008). Vignetting causes problems when radiometric quantities are estimated from images (Lebourgeois et al., 2008). Lelong (2008) found the mean digital number to decrease by 5% in the visible bands and by 35% in the infrared one, with the latter mostly due to an additive high-pass filter employed in front of the sensor.

The most-widely used correction method relies upon the generation of a per-pixel correction factor lookup-table (LUT) from a flat field image. Being a uniform, spectrally homogeneous, Lambertian surface, the brightness variations can only be attributed to vignetting, not to the flat field (Kelcey and Lucieer, 2012; Lelong, 2008). Corresponding correction factor imagery can be generated, assuming

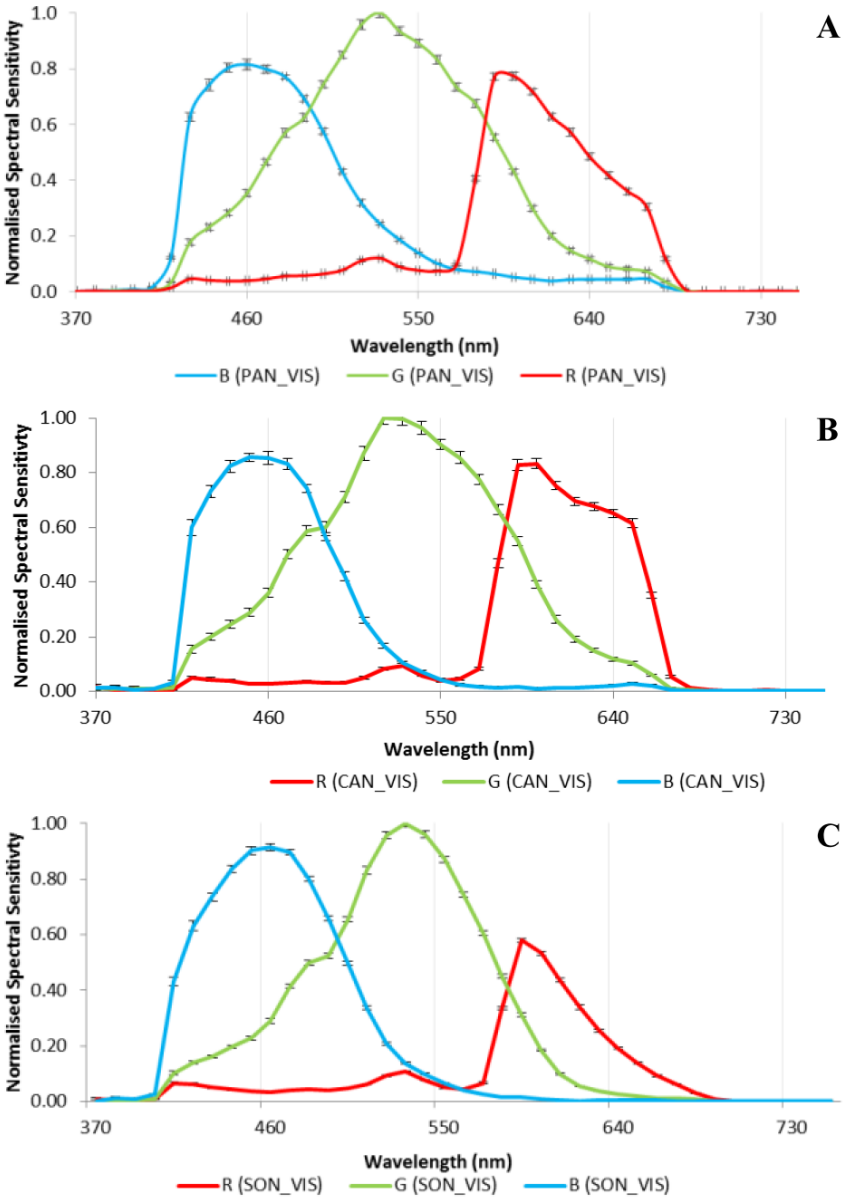

Figure 3.10: Spectral response curves of three unmodified RGB cameras, normalised to the peak value of each camera's green channel. A: Panasonic DMCLX5, B: Canon A2200, C: Sony Nex7. Source: Berra et al. (2015)

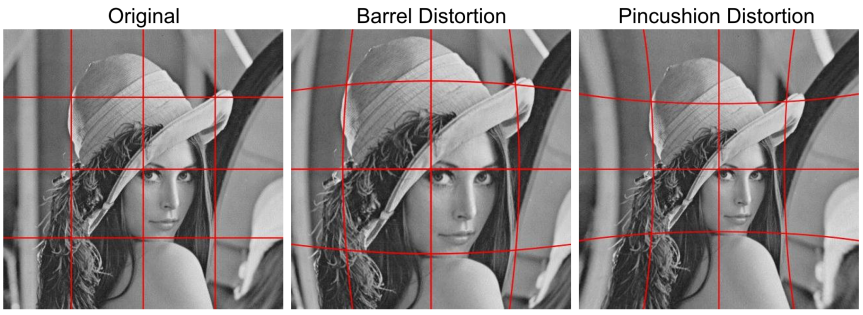

Figure 3.11: Forms of lens distortion: original, barrel lens distortion, pincushion lens distortion. Source: Kelcey and Lucieer (2012)

that the brightest pixel within the image represents the true radiance not influenced by vignetting (Kelcey and Lucieer, 2012). Another method is to average an ensemble of a high number of randomly taken images at different sites, and create a LUT under the assumption that directional effects cancel out statistically (Burkart et al., 2017; Verger et al., 2014). Since vignetting varies between bands, exposure length, filters, aperture and focal length, a different LUT needs to be created for each band and setting (Lebourgeois et al., 2008).

Lens distortion is a modification altering the spatial properties of incoming radiance, and results in a radially dependent geometric shift in a measurement position (Kelcey and Lucieer, 2012). It is caused by a combination of differences in magnification level across the lens surface and the misalignment between lens and the detector plane. It is commonly expressed as radial and tangential distortion, with radial distortion showing a curving effect towards the centre of the lens. Negative displacement results in pincushion distortion, positive displacement in a barrel distortion effect (see figure 3.11) (Kelcey and Lucieer, 2012). Tangential distortion is caused by the non-alignment of the lens with the sensor, resulting in a planar shift in the perspective of the image (Kelcey and Lucieer, 2012).

A widely used model for lens distortion is the Brown-Conrady model, which is able to calculate both the radial and tangential components of lens distortion. It makes use of an even-order polynomial model to calculate the radial displacement of a given pixel. For this, distortion coefficients need to be calculated, which can be done via the utilisation of a planar calibration grid of known geometric properties. Images of the grid are taken from different orientations, which allows for the estimation of both the intrinsic and extrinsic camera parameters based on the point correspondence between the defined geometric properties of the grid and

the distorted points within the image (Kelcey and Lucieer, 2012).
Other modifications include sensor noise and radiance strength disparities, but are commonly not accounted for in studies employing COTS imagery in their analysis. Kelcey and Lucieer (2012) provide a detailed discussion of those modifications.

3.4.3 Processing UAV-Acquired COTS Imagery

A UAV-based image acquisition campaign over a larger area commonly results in hundreds or thousands of images at very high resolution (Laliberte et al., 2011). Every image requires correction for the modifications mentioned above as well as for variations in radiance. The radiance measured by the camera depends on incident radiation at the given time of acquisition, plus the optical properties of the scene. Both the quantity and quality (i.e. the spectral composition) are related to the solar zenith angle and to prevalent atmospheric conditions. To make images comparable, they need to be radiometrically normalised, accounting for both incident radiation and camera settings (Lebourgeois et al., 2008; Zaman et al., 2014). Thereby, the spectral information stored as digital numbers (DN) is converted to reflectance values that correct for factors listed above. This approach is especially important in applications where multitemporal acquisitions are required, such as agriculture or forestry (Berra et al., 2017).
For the creation of an orthophoto, images need to be mosaicked (although Rasmussen et al. (2016) point out that mosaicking is not necessary in agricultural applications, but may facilitate analysis). Two approaches are known: The first relies on traditional photogrammetric methods (software such as Microsoft ICE, or Erdas PhotoModeler), the second approach on software coming from the computer vision domain (Structure from Motion - SfM). The main difference is that SfM software computes 3D points and bases the stitching process on the 3D information, where the colour is assigned accurately to the pixels (Rasmussen et al., 2016). Furthermore, the perspective distortions of the camera are corrected for, which is not necessarily the case in the photogrammetric approach (Rasmussen et al., 2016). Both approaches are computationally intensive.

4 Material and Methods

4.1 Study Area and Field Experiment

This study was based on a field experiment that was established at Campus Klein-Altendorf (CKA), the university's agricultural research facility located 15 km southwest of Bonn between the cities of Meckenheim and Rheinbach (6°59′32″E, 50°37′51″N, 184 meters above sea level). The climate at CKA is characterized by temperate humid conditions with maritime influence. Its location lies in the rain shadow of the Eifel region, in the warmer, rural part of the Lower Rhine Basin. Long-term average yearly precipitation from 1956 to 2014 was 603 mm, the long-term average temperature for the same period was 9.4 °C. The soil is classified as hypereutric, siltic Haplic Luvisol[1] that developed from Loess. The measure of productivity of the field according to the German system[2] is 85 - 90 (`www.cka.uni-bonn.de/standort`, accessed December 22, 2017).

The field experiment was established in a completely randomised sampling design and consisted of a combination of two plant densities (PD) and two treatments of nitrogen (N) fertilization.

This design is commonly used to compare treatments when environmental conditions are fairly uniform, and the principles of replication and randomisation apply. Every treatment is randomly applied to several experimental plots. This ensures that there is no subjectivity in the allocation of treatments to plots. Furthermore, the effects of other factors are expected to cancel out when the means of treatments are compared (Clewer and Scarisbrick, 2013).

Implementation occurred during the growing seasons (May - October) in the years 2015 and 2016. Plant densities comprised 50,000 plants ha^{-1} (S1) and 100,000 plants ha^{-1} (S2), the N treatments 100 kg N ha^{-1} (N1) and 200 kg N ha^{-1} (N2), respectively. Every treatment was conducted on a plot sized 3 m x 30 m, with five repetitions each. Row spacing was 0.75 m. S1 plots were thinned out manually

[1] Deutsche Bodensystematik: Normparabraunerde aus Löss

[2] Ackerzahl nach Reichsbodenschätzung

immediately after emergence since the drilling machine could not be adjusted to varying plant densities. Additionally, all plots were checked for wrongly set plants. N was applied as inorganic ammonium sulfate (ASN) before planting as a one-time treatment. A herbicide (Zintan Platin Plus Pack, Syngenta Agro GmbH, Maintal, Germany) was applied according to standard practice to suppress the growth of weeds. No irrigation scheme was practised.
Two different cultivars were grown between the years, due to unavailability of the cultivar seeds grown in 2015 in the proceeding year. In 2015, the hybrid *Panasch* (AGA Saat, Neunkirchen, Germany) was cultivated, the hybrid *Ricardinio* (KWS Saaten SE, Einbeck, Germany) in 2016.

4.2 UAV-based Image Acquisition

4.2.1 The UAV

We deployed an Mikrokopter OktoXL6S12 (HiSystems GmbH, Moormerland, Germany) rotary copter. The device was lifted by eight engines, which in turn were powered by two 6S batteries. Maximum flight time depended on wind speed and payload, but was usually around 20 minutes. The installed camera mount was able to compensate the copter's rotations in roll and pitch direction, which held the cameras in a stable nadir viewing angle.
The copter mastered waypoint flights via a GPS module. Flight planning was done ahead of the first flight, and the same plan was used for every image acquisition campaign.

4.2.2 Cameras and Imagery

We used two Canon ELPH 110HS compact digital cameras with an effective still resolution of 16.1 megapixels to acquire images. Each camera was equipped with a 1/2.3-inch CMOS sensor containing 4608 x 3456 recording pixels. Originally, both cameras were sensitive to light in the blue, green and red (RGB) domain, due to the Bayer filter mounted on top of the sensor. The modification was done by LDP LLC Inc. (Carlstad, NJ, USA), with installation of filters that were developed in-house. The first camera (hereafter: RGNIR camera) was fitted a blue rejection filter, which supposedly blocked light in the blue domain and in turn rendered this band sensitive to NIR light from roughly 800 nm to 900 nm.

After the modification, this camera delivered R = Red + NIR, G = Green + NIR and B = NIR only (Figure 4.2b). The second camera (hereafter: BGNIR camera) was fitted a dual-band pass filter that blocked light in the red domain; the red channel became sensitive for light in the wavelengths 680 nm to 780 nm (covering the red edge, fig. 4.2a). When the cameras were combined, 5 bands were available (Fig. 4.2c), with a redundancy of the green band.
The Canon Hack Development Kit (CHDK - `http://chdk.wikia.com/`, accessed December 22, 2017) was used as the software application to capture RAW imagery, since the cameras' original firmware did not provide this feature. CHDK is an open-source, freely available software provided for Canon cameras, that adds a number of features not provided by the original software, such as shooting images in RAW, ultra-fast shutter speeds, shutter-priority exposure or aperture-priority exposure. The software also allows for fixed shutter speeds and aperture, which was used to capture all images with the same camera settings.
Images were acquired with a focal length of 4.3 mm. Shutter speed was adjusted per sampling date depending on incident light conditions, but was commonly held between 1/1600s and 1/800s. CHDK was programmed to shoot in an interval mode, with one image every 4 seconds. Images were acquired from approx. 50 meters above ground level.
The flight altitude defines the ground sampling distance (GSD) of each pixel in the images and the maximum area covered without change of batteries (Mesas-Carrascosa et al., 2015), and therefore represents the fair balance between desired spatial resolution and maximum flight time. The ground sampling distance is a result of sensor size, flight altitude and focal length and was calculated to be 1.55 cm given the set of cameras and the flight height.

4.3 Preprocessing of Images

4.3.1 Demosaicking, Removal of Lens Distortion and Vignetting

All RAW images were converted to 16 bit linear TIFF using the dcraw software (David Coffin, `https://www.cybercom.net/~dcoffin/dcraw/`, accessed December 22, 2017). The AHD demosaicking algorithm was used as suggested by Verhoeven (2010). We used Agisoft Lens (Agisoft LLC, St. Petersburg, Russia) to

calculate the Brown-Conrady coefficients. Agisoft Lens is an automatic lens calibration software, which uses a calibration grid (chessboard design) displayed upon a flat panel computer LCD screen to estimate camera calibration parameters. A series of images was taken from slightly different angles with both cameras, and fed into the software, which calculated the coefficients subsequently.
Vignetting effects were quantified averaging 1,500 randomly taken RAW images. A per-pixel correction factor LUT for every band was generated (Fig. 4.3), assuming the brightest pixel corresponds to the true radiance. Every image used in this study was corrected for vignetting effects using the corresponding LUT. The workflow was implemented in *R* (R Core Team, 2017) via the *raster* package (Hijmans, 2016).

4.3.2 Conversion to Reflectance

The empirical line calibration method was used to convert the DNs to reflectance values. This method uses an empirically-derived equation which predicts reflectance from radiance (Fig. 4.4), based on reflectance spectra from calibration targets within the image and their respective radiances recorded by the sensor (Smith and Milton, 1999). A separate equation is developed for each band, and then applied to each pixel of the image. The equations attempt to remove both illumination and atmospheric effects (Smith and Milton, 1999).
We used aluminium plates sized 50 cm x 50 cm covered with Nextel coating (Mankiewicz Gebr. & Co., Hamburg, Germany) placed on the ground next to the field as targets for conversion of digital numbers to reflectance (Fig. 4.5).
Covered with the coating, the targets exhibited a fairly uniform reflectance along the electromagnetic spectrum between 400 nm and 1100 nm, with good lambertian characteristics (see Aasen et al. (2015, Figure 8) for spectra of targets used). In 2015, three panels were used (black, grey, white) for conversion. Due to the NIR bands' low sensitivities, shutter speed had to be adjusted accordingly, which led to saturation of the white panel's signal in the visible bands. Therefore, only the black and grey panels responses were used for conversion of the visible bands, all three panels for conversion of the NIR bands. In 2016, five panels (black, darkgrey, grey, lightgrey, white) were placed next to the field, but only the same ones as in 2015 were used for conversion. We found that, when using all five panels for conversions and comparing reflectance values of invariant features from 2015 and 2016 (e.g. asphalt from the road next to the field), reflectance differed

between 2% to 3%. 100 pixels per panel were extracted from the image that captured the panels from closest to nadir position, averaged, and related to the panel reflectance.

4.3.3 Orthomosaicking

Agisoft Photoscan Professional (Agisoft LLC, St. Petersburg, Russia) was used to perform the photogrammetric processing. It includes the following main steps:

i Image alignment and referencing, where the camera position and orientation is found in 3-dimensional space and coordinates are assigned based on ground control points (GCPs) visible in the images. We used six GCPs located at the edges of the field to reference our images. The position of the points was determined using a Trimble Geo7X (Trimble Inc., Sunnyvale, CA, USA) differential GPS. Alignment was done with the accuracy set to high.

ii Creation of a dense point cloud. Based on the estimated camera positions, Photoscan calculates depth information and combines them into a single dense 3D point cloud. This step is computationally very intensive. We chose a medium reconstruction quality.

iii Mesh creation. Here, the structure of the captured objects is approximated by a number of small polygons. We selected 'Height field' as the surface type, and the dense cloud as the source data.

iv Building the orthomosaic. In this step, Photoscan generates a high resolution image based on the source photos and the reconstructed model. We disabled the blending mode, such that the value for the pixel is taken from the picture with the camera view being almost along the normal to the reconstructed surface in that point. Our intention was to thereby minimise directional effects, since only the central part of each image captured in nadir position contributes to the orthomosaic.

Multi-camera approaches require image registration to accurately establish a relationship between the pixel coordinates of every camera (Rabatel and Labbé, 2016). This is either done by registering all bands directly, or computing a georeferenced and orthorectified mosaic for every set of camera imagery, and subsequently overlaying them based on their coordinates (Rabatel and Labbé, 2016).

We used the first option, processing the images of both cameras in the same workspace and finally built separate orthomosaics (see figure 4.6 for example). A visual assessment of accuracy revealed alignment at sub-pixel accuracy.
This workflow explained above resulted in two orthomosaics per measurement date, one for each camera respectively. They were subsequently analysed in R (R Core Team, 2017).

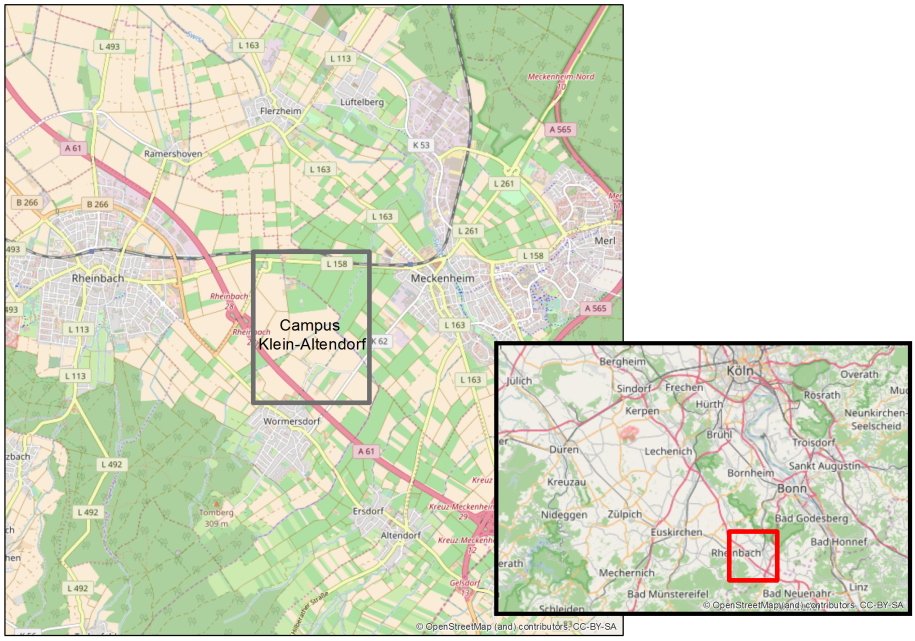

Figure 4.1: The location of Campus Klein-Altendorf in the Lower Rhine Basin. Source: osm.org

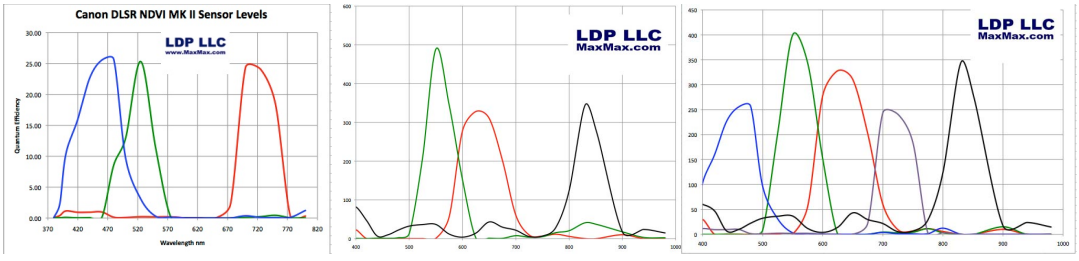

(a) BGNIR Response (b) RGNIR Response (c) Combined Response

Figure 4.2: Cameras' spectral responses as provided by the modifying company. Source: maxmax.com

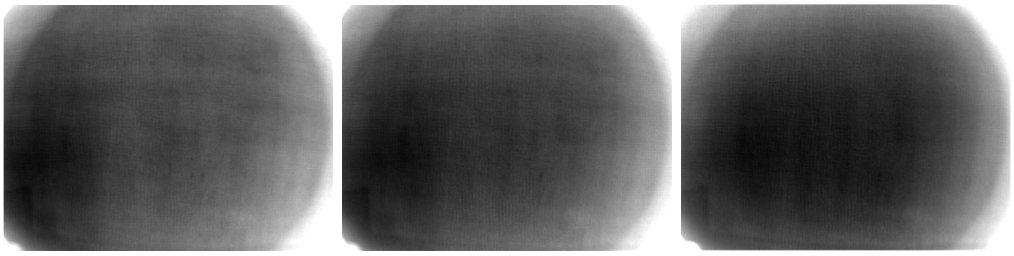

(a) BGNIR Blue Band (b) BGNIR Green Band (c) BGNIR NIR Band

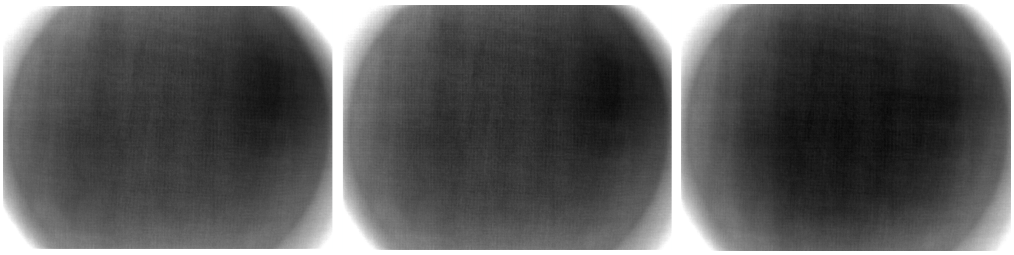

(d) RGNIR Red Band (e) RGNIR Green Band (f) RGNIR NIR Band

Figure 4.3: Visualisation of vignetting effects.

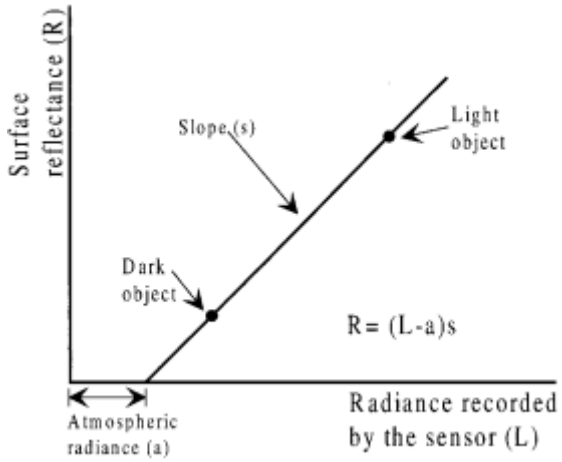

Figure 4.4: Prediction equation development from two calibration targets using the empirical line method. Source: Smith and Milton (1999)

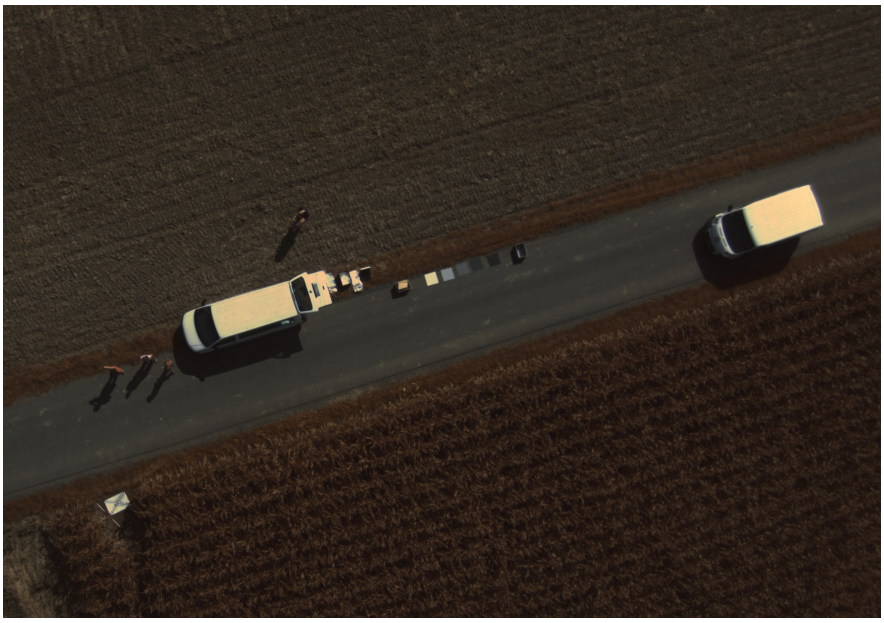

Figure 4.5: Calibration targets seen from 50 m height, visible between the two vehicles. Image captured with RGNIR camera.

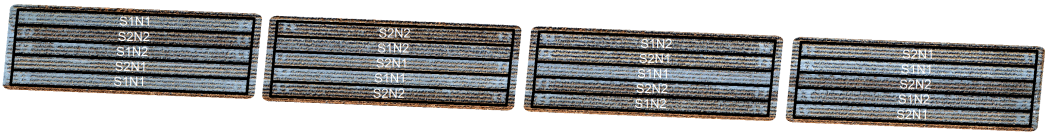

(a) BGNIR

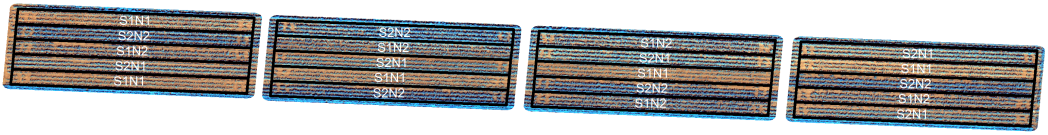

(b) RGNIR

Figure 4.6: Example of the two separate orthomosaics generated for every acquisition day. Figure 4.6a shows orthomosaic generated from the BGNIR camera data, figure 4.6b the orthomosaic generated from the RGNIR camera data. Images were acquired on June 25, 2015. Overlying polygons indicate extent of experimental plots. Destructive sampling areas are visible towards the left and right edges of the block. To lower the size of the dataset, spaces between blocks were removed.

5 Study I: Remote green LAI Estimation in Maize Using UAV-based Modified Consumer Camera Imagery Part I. Impact of Plant Density and Nitrogen Fertilisation

5.1 Abstract

Measuring field trial green leaf area index (gLAI) development in maize using in-situ measurements is labor-intensive, costly work, with often inaccurate results. Unmanned Aerial Vehicle (UAV)-based remote sensing (RS) facilitates estimation due to quick and easy deployment of sensors that are able to cover a number of treatment plots in little time. Modified low-cost cameras with sensitivity in the visible and near-infrared (NIR) domain have recently gained the attention of the scientific community. However, their potential to sense differences in gLAI in maize induced by management factors is largely unexplored. We used two UAV-mounted modified low-cost consumer cameras to acquire nadir images of a maize trial that comprised four treatments in five repetitions, including two plant densities and two nitrogen fertilization levels. The UAV data covered two growing seasons (years 2015 and 2016) in bi-weekly intervals with a ground sampling distance of 1.5 cm. gLAI was measured destructively using a planimeter, on the same days as the image acquisition, with at least 32 samples per date. Relating three selected spectral vegetation indices (NDVI, GNDVI, 3BSI) to our gLAI measurements, we found differing but definite relationships per treatment factor.

gLAI estimation using the two-band indices (NDVI, GNDVI) yielded good results up to gLAI values of 3. The 3-bands approach (3BSI) did not offer any benefits. Comparing gLAI results to the spectral vegetation indices, we determined that sole reliance on vegetation indices was insufficient to draw the right conclusions on the impact of management factors on leaf area development in maize canopies.

5.2 Introduction

Leaf area index (LAI) is one of the key variables in crop growth analysis due to its influence on light interception, biomass production, plant growth and ultimately on crop yield, and is critical to understanding the function of many crop management practices (Wilhelm et al., 2000). It is defined as the total one-sided area of leaf tissue per unit ground surface area (Jonckheere et al., 2004), and can be subdivided into photosynthetically active and inactive components (Nguy-Robertson et al., 2012). The former is composed of green leaf area as a photosynthetically functional component and referred to as green LAI (gLAI) (Viña et al., 2011). Green LAI is a commonly derived variable in field experiments that evaluate the influence of management factors on crops (e.g. fertilizer supply, plant density or pest management). Throughout literature, the terms referring to the leaf area of plants vary. We use the term LAI to describe the total one-sided area including green and senescent tissue, and the term gLAI to describe green, photosynthetically functional leaf area only. Furthermore, the term Green Area Index (GAI) refers to all green elements of the plant canopy (not just leaves) that contribute to the reflected radiation.

Leaf area development of maize (*Zea mays*) is influenced by genotype, climate, plant density (PD) and soil fertility (especially nitrogen supply (N)) with the two latter widely recognized as the most important crop management practices that determine maize plant development and ultimately grain yield in modern agriculture (Yan et al., 2017). The positive yield response to N is mainly due to a larger LAI which increases the amount of radiation intercepted throughout the growing period, a higher average daily photosynthesis rate, or a combination of both (Vos et al., 2005). LAI is reduced in low N supply, mainly by reduction of individual leaf area. Increased plant densities lead to higher LAIs due to increased optimum plant population in modern maize hybrids. On the other hand, high stand densities result in intraspecific competition, which causes an

early increase in interplant variability and may accelerate rate of leaf senescence, thereby post-silking dry matter accumulation.

As ground-based green LAI (gLAI) estimation for detection of differences or similarities between treatments is time-consuming, labour-intensive and spatially restricted, there is need for covering larger amounts of plots at low-cost and within a short period of time. Remote sensing (RS) has proven to estimate gLAI accurately (Gitelson et al., 2003; Nguy-Robertson et al., 2012; Viña et al., 2011), with different approaches documented in scientific literature. The most common and simplest approach assumes a relationship between the spectral data and plant gLAI and thus relies on an explicit parameterized formula, typically derived from statistical knowledge of measured gLAI values and their respective spectral response (Verrelst et al., 2015a). Spectral vegetation indices (SVI) are widely used as the link to gLAI, since they combine information from wavelengths of light absorption and reflectance of plants and limit the impact of directional effects. The interpretation of SVI time courses, however, suffer from soil background reflectance and soil moisture influences as well as saturation of the signal at high gLAI values (Zheng and Moskal, 2009).

With the advancement and easy employment of unmanned aerial vehicles (UAV) and the capability of low cost cameras to sense light in the visible and near-infrared domain, new domains have opened for scientists and agronomists to explore the determination of green leaf area index values at very high temporal and spatial resolution, possibly de-coupled from weather conditions and high procurement cost for technical equipment.

A selection of publications has focused on the RS of leaf area index in crops using UAV based imagery. In a parametric regression approach using a modified RGB camera, Hunt et al. (2010) found the Green Normalized Difference Vegetation Index (GNDVI) to be linearly related to LAI in winter wheat where values were below 2.7 (with an R^2 of 0.85); the index was not responsive to changes above that value. They concluded that more research is needed to distinguish differences in values caused by variation in leaf chlorophyll concentration from those caused by variation in leaf area index (Hunt et al., 2010). In a physically-based approach, Verger et al. (2014) used a UAV-mounted multispectral camera to invert the PROSAIL radiative transfer model using the reflectances from 4 bands for estimation of green area index above wheat and rapeseed. They found that normalized reflectance improved performance of GAI estimates, particularly

under unstable illumination conditions. RMSE for estimates was 0.17 (Verger et al., 2014). Córcoles et al. (2013) used a standard RGB camera to estimate leaf area index of onion via the relationship between estimated canopy cover and LAI. They found that the relationship varied depending on the stage of crop development, with a closer relationship in early growing stages (Córcoles et al., 2013). We were interested in the potentials of UAV-based modified low cost cameras for gLAI estimation in a factorial maize experiment that simulated the two most common crop management practices (plant density and nitrogen fertilizer application). Our objectives of this study therefore were:

i Firstly, we wanted to evaluate the functional dependence between gLAI and selected spectral vegetation indices based on low-cost imagery per management factor at very high spatial resolution,

ii Secondly, we assumed the existence of a functional dependence and so wanted to determine to what extent the chosen broadband indices cover green LAI temporal dynamics induced by plant density and/or nitrogen supply. We wanted to learn if it is possible to draw the same conclusion on the effects of management factors on gLAI development by solely relying on SVI data.

To our knowledge, no study has looked at gLAI – SVI relationships using modified consumer camera imagery in maize before.

5.3 Material and Methods

5.3.1 Study Site and Field Experiment

The study field was located at the University of Bonn's agricultural research facility Campus Klein-Altendorf (CKA), located some 15 kilometers southwest of the city of Bonn, Germany (6°59′32″E, 50°37′51″N, 184 meters above sea level). Climate is characterized by temperate humid conditions with maritime influence. The long-term average precipitation is 625 mm, the average temperature 9.6°C. Soil is classified as alkaline, nutrient rich Haplic Luvisol that developed from loess (Gaiser et al., 2012; Kautz et al., 2010).
The field experiment consisted of a combination of two plant densities and two treatments of nitrogen (N) fertilization arranged in a random sampling design,

and was conducted during the growing seasons (May – October) in the years 2015 and 2016. The plant densities comprised 50,000 plants ha^{-1} (S1) and 100,000 plants ha^{-1} (S2), the N treatments 100 kg ha^{-1} (N1) and 200 kg ha^{-1} (N2), respectively. Every treatment was conducted on a plot sized 3 m x 30 m, with 5 repetitions each (see figure 5.1 for experimental layout). Row spacing was 0.75 m. No irrigation scheme was practiced. Herbicides were applied according to standard practices. Low plant density plots were thinned out by hand after emergence, and all plots were checked for wrongly set plants. N was applied

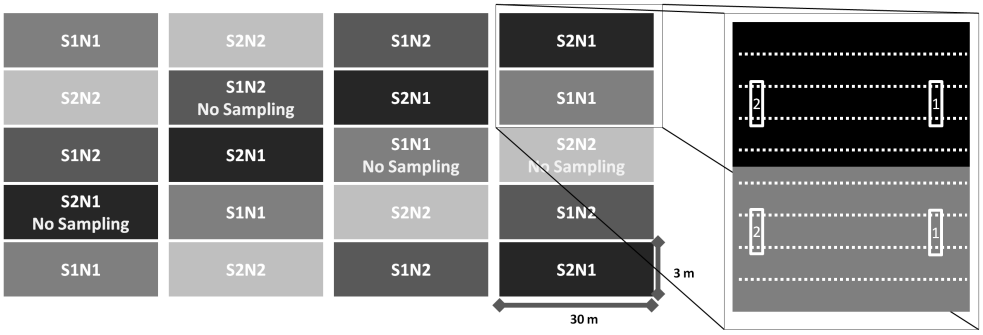

Figure 5.1: Experimental setup (S1 = low planting density (50.000 plants ha-1), S2 = high planting density (100.000 plants ha-1), N1: low nitrogen application (100 kg ha-1), N2: high nitrogen application (200 kg ha-1)). The enlargement on the right shows gLAI sampling spots.

as inorganic ammonium sulfate (ASN) before planting as a one-time treatment. During the 2015 growing season, the early maturing hybrid cultivar Panash (AGA Saat, Neunkirchen, Germany) was planted, the hybrid cultivar Ricardinio in 2016 (KWS Saaten AG, Einbeck, Germany). Both cultivars are similar in their characteristics (FAO number, medium late ripening). The location of the trial was shifted by 170 meters between the years. Table 5.1 provides further details about the trials, including captured phenological stages according to the BBCH scale.

Rainfall and air temperature were recorded at a weather station in the vicinity of the field. The distribution of rainfall differed between the years; 2015 received less rain during the early growing phases (˜80 mm difference at a temperature sum of 500). In total, more rain fell until harvest in 2015 than in 2016 (Figure 5.2). The temperature sum was calculated using 8°C as base temperature as confirmed for temperature climates by Birch et al. (2003). Temperatures beyond 30°C were included in the calculation as the maximum temperature of 30°C, since no increased growth was observed beyond that temperature.

Table 5.1: Basic data about the trials 2015 and 2016. Temperature sum at different phenological stages given in brackets.

Year	2015	2016
Cultivar	Panash (AGA Saat) FAO 200	Ricardinio (KWS) FAO 220
Planting Date	05 May 2015	04 May 2016
Emergence	15 May 2015	10 May 2016
Begin Flowering	14 July 2015 (536.32)	15 July (585.27)
Fruit Development: Milk-ripe stage	14 August 2015 (888.01)	15 August 2016 (918.41)
Full ripening	13 October 2015 (1244.11)	23 September 2016 (1346.67)
Harvest	22 October 2015	29 October 2016
Precipitation until harvest [mm]	393.2	353.1
Temperature Sum until harvest [°Cd]	1251.2	1454.2

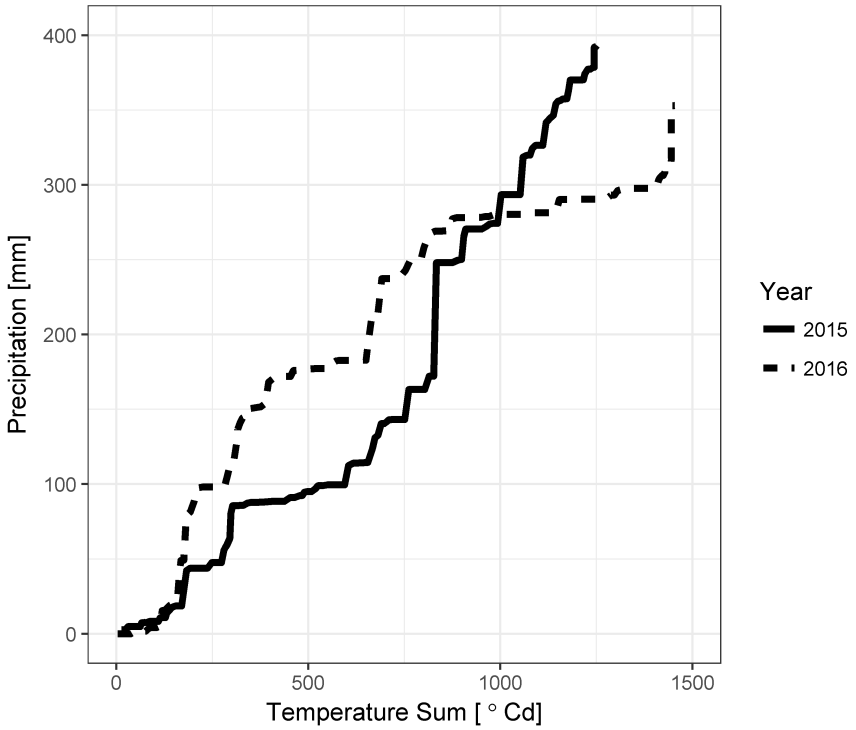

Figure 5.2: Temperature sum (°Cd) vs. precipitation (mm). The solid line shows data for 2015, the dashed line data for 2016.

(a) The UAV (b) The camera system

Figure 5.3: UAV and camera setup. Left picture shows the octocopter employed in this study, the right picture the two cameras mounted inside the frames.

5.3.2 The UAV and Camera System

We employed two Canon ELPH 110 HS digital compact Red-Green-Blue (RGB) cameras, modified by LDP LLC Inc. (Carlstad NJ, United States). The cameras 1 2/3 inch sized CMOS sensor comprised 4608 x 3456 recording pixels (i.e. 16.1 Megapixels). The first camera (hereafter: RGNIR camera) was fitted a blue rejection filter, with sensitivity in the near-infrared (NIR) domain from roughly 800 nm – 900 nm. The information in the blue band was replaced by information in the NIR domain. The second camera (hereafter: BGNIR camera) was fitted with a dual-band-pass filter that blocked light in the red domain; this rendered the sensor sensitive for light in the wavelengths 680 nm to 780 nm. Sensitivity was specified by the provider and was not further investigated from our side. Due to the inherent sensitivity of the camera sensor and the colour filter array fused on top to light in the visible and near-infrared domain, each band became sensitive to the original spectral domain and/or infrared radiation (Nijland et al., 2014). The RGNIR camera delivered R = Red + NIR, G = Green + NIR and B = NIR only, the BGNIR camera delivered B = Blue + NIR, G = Green and R = NIR. The cameras were mounted inside a frame underneath a Mikrokopter OktoXL6S12 (HiSystems GmbH, Moormerland, Germany) octocopter (see Figure 5.3 for picture), a system that has been widely used in scientific studies (Aasen et al., 2015; Bendig et al., 2015; Rasmussen et al., 2016). Zhou et al. (2016) as well as Lu and He (2017) employed the BGNIR camera model in their studies.

5.3.3 Field Measurements

For measuring green leaf area index, 0.5 m of plants in two adjacent rows were sampled destructively at two positions (see Figure 5.1 for visualisation) within 4 plots of each treatment at every sampling date (i.e. 4 treatments x 4 plots x 2 samples = 32 samples per sampling date). To minimize edge effects, we did not sample the outer rows of each plot and skipped 0.5 m of standing plants between the collection dates. Four plots (i.e. one plot per treatment) remained unsampled during the entire course of the trial. Samples were immediately transported back to the institute and leaf area was measured using the LI-COR LI-3100C area meter (LI-COR Inc., Lincoln, NE, USA). gLAI was determined by dividing the total leaf area of each sample by the sampling area (i.e. leaf area / 0.75 m^2). In total, samples were taken on eight dates in 2015 and ten dates in 2016, with a rough interval of 14 days. Assessing LAI and gLAI respectively by destructive sampling is considered the most accurate, labour-intensive method and often serves as calibration for indirect measurement techniques (Jonckheere et al., 2004). Multispectral data was collected on mostly cloud-free days immediately before the sampling of the plants. To avoid major shadow cast, image acquisition took place around solar noon. Images were acquired from an altitude of 50 m, which translates into a ground sampling distance (GSD) of 1.5 cm. Each image was taken with a focal length of 4.3 mm at nadir view. The shutter speed was adjusted from date to date depending on incident light conditions, but remained constant throughout each flight campaign. Six ground control points (GCP) were distributed around the field to ensure correct georeferencing and alignment of the orthophotos, with the position of the GCPs measured by a Trimble Geo7x differential GPS (Trimble Inc., Sunnyvale, CA, USA). We used three different greyscale reference targets corresponding to 5%, 16%, and 58% reflectance respectively in a level position next to the field to convert the images' digital numbers to reflectance values.

5.3.4 Preprocessing of Images

Images were captured in RAW format using the Canon Hackers Development Kit (CHDK - `http://chdk.wikia.com/wiki/CHDK`, accessed 21 October, 2017) to maintain a linear relationship to scene irradiance (Akkaynak et al., 2014; Verhoeven, 2010). The conversion to 16 bit linear TIFF was done using the dcraw software (David Coffin, `https://www.cybercom.net/~dcoffin/dcraw/`, accessed 21

October, 2017) with the adaptive homogeneity directive (AHD) mosaicking algorithm employed following the recommendation by Verhoeven (2010); no gamma correction was applied. Vignetting effects were removed by creating pixel lookup-tables through averaging 1,500 randomly taken images (Burkart et al., 2017; Lebourgeois et al., 2008; Verger et al., 2014). Lens barrel distortion was removed by implementing the Brown-Conrady model implemented in the Agisoft Lens (Agisoft LLC, St. Petersburg, Russia) software package.
We realized that the NIR influence in the visible domains of the cameras did not increase proportionally with increasing NIR reflectance; due to low sensitivity of the sensor in the near-infrared domain, the influence remained stable beyond a certain level. We used a logarithmic function to normalize all pixels in the red and blue bands domain for near-infrared influence. For this, we acquired images of five different grey-scaled panels with nominal reflectances of 5%, 8%, 16%, 30% and 58%, calculated the ratios between the bands in the visible domain and the near-infrared band and fitted a function through the points of red and blue reflectance and the ratios, respectively. Subsequently, the ratio between each red, blue and the respective NIR pixel in each image was calculated, and corrected using the derived function described above. The green band of the RGNIR camera was ignored because we relied on the undisturbed green information from the BGNIR camera. Digital numbers (i.e. pixel values as provided by the cameras) were subsequently converted to reflectance values using the empirical line calibration method via the response of the calibration targets (see Smith and Milton (1999) for a method explanation). Agisoft Photoscan Professional (Agisoft LLC, St. Petersburg, Russia) was used to mosaic and rectify all images to one orthomosaic per camera per acquisition date. We disabled the blending mode to prevent an alteration of pixel values; Agisoft hereby takes the values of each pixel from the photo with the camera view that is closest to nadir view of the reconstructed surface in that point.

5.3.5 Extraction of Reflectance Values and Calculation of Vegetation Indices

We used the raster package (Hijmans, 2016) implemented in R (R Core Team, 2017) to extract the reflectance values of those particular 0.75 m^2 area in the field where the samples were taken. The mean value of each band was calculated subsequently. We calculated three spectral vegetation indices (SVI) based on

the extracted values: NDVI (Normalized Difference Vegetation Index) as the most widely used index in science, the GNDVI (Green Normalized Vegetation Index) and the 3BSI (Three Band Spectral Index). The GNDVI uses the green band instead of the red band; which renders it more responsive to different leaf chlorophyll concentrations (Daughtry et al., 2000). The 3BSI was introduced by Verrelst et al. (2015b) and outperformed most two-band vegetation indices in parametric LAI regression performance. The indices were calculated as follows:

$$NDVI = \frac{(\rho_{NIR} - \rho_{Red})}{(\rho_{NIR} + \rho_{Red})} \tag{5.1}$$

$$GNDVI = \frac{(\rho_{NIR} - \rho_{Green})}{(\rho_{NIR} + \rho_{Green})} \tag{5.2}$$

$$3BSI = \frac{(\rho_{NIR} - \rho_{Red})}{(\rho_{Green} + \rho_{Red})} \tag{5.3}$$

5.3.6 Statistical Analysis

We used descriptive statistics to pronounce the characteristics of gLAI and spectral vegetation index development. Minimal, maximal and mean values were used to evaluate the impact of each treatment. The coefficient of variation was used to assess the variability of measured values for each sampling date. The standard analysis of variance (ANOVA) was calculated to determine whether there were differences between the treatments regarding gLAI and spectral vegetation index values. Tukey's honest significant difference (HSD) test ($\alpha = 0.05$) was used to compare pair wise treatment results. Nonlinear least-squares regression was used to establish the statistical relationship between the measured gLAI values and the SVI values. Although possibly not providing the best fit, we only included exponential models following the formula $SVI = a * (1 - e(-b * gLAI))$ in our study, due to the well-documented invariability of reflectance in the visible spectrum at higher gLAI values (Asrar et al., 1984). At $gLAI = 0$, we fixed the intercept to the soil reflectance derived from averaging 1,000 soil pixels. The residual sum of squares (RSS) was used to evaluate models' performances. RSS measures discrepancy between the data and the derived model; small values indicated a good fit.

5.4 Results

5.4.1 Green Leaf Area (gLAI) Development Statistics

The growing seasons in 2015 and 2016 went well without major disruptive events. First measurements were taken in mid-June of each year, last measurements in mid-October. On average, the lowest gLAI was measured in the S1N1 treatments, the highest in the S2N2 treatments (see Table A in the Appendix for detailed results). The S2N1 treatment developed higher gLAI values than the S1N2 treatment. In both years, the two low plant densities showed lower standard deviation than the high plant densities, the coefficient of variation however did not indicate a trend. Absolute lowest values were measured in the S1N1 treatments (0.12 in 2015 and 0.06 in 2016), the highest values in S2N2 in 2015 (5.19) and in S2N1 in 2016 (5.53). The S1N2 trial developed higher gLAI values in 2015 than in 2016.
For 2015, Tukey's HSD revealed that gLAI values exhibited significant differences between all treatments. For 2016, no significant differences could be seen between the N treatments. Figure 5.4 shows the gLAI development over time, plotted against temperature sum. Leaf area developed quicker in 2015 than in 2016, and faster in high plant densities than in low plant densities. Leaf area increased faster in high N treatments than in low N treatments. Senescence occurred quicker in high plant densities, and earlier in 2016 than in 2015. In both years, gLAI dropped quicker in the S2N2 treatment than in the S2N1 treatment. Contrary to 2016, the 2015 development curves stagnated between 560 and 1100 degrees temperatures sum, without major increases or decreases in leaf area. 2016 showed a more dynamic progression, with S1N1 and S2N1 peaking at 828 degree days, S2N2 earlier at 635 degree days, and S1N2 later at 918 degree days.

5.4.2 LAI-SVI Parametric Regression

Figure 5.5 to Figure 5.7 show the gLAI – SVI models, separated into N fertilisation and plant density impact, per year. Figure 5.5 shows gLAI – NDVI models, Figure 5.6 the gLAI – GNDVI models, and Figure 5.7 the gLAI – 3BSI models, derived as explained in subsection 5.3.5. NDVI models differed for 2015, and resembled for 2016. For 2015, no saturation effect could be noticed within the range of measured gLAI values. Models of S1N2 and S2N1 were similar. In 2016, gNDVI models exhibited saturation at gLAI values > 3. The comparison between plant

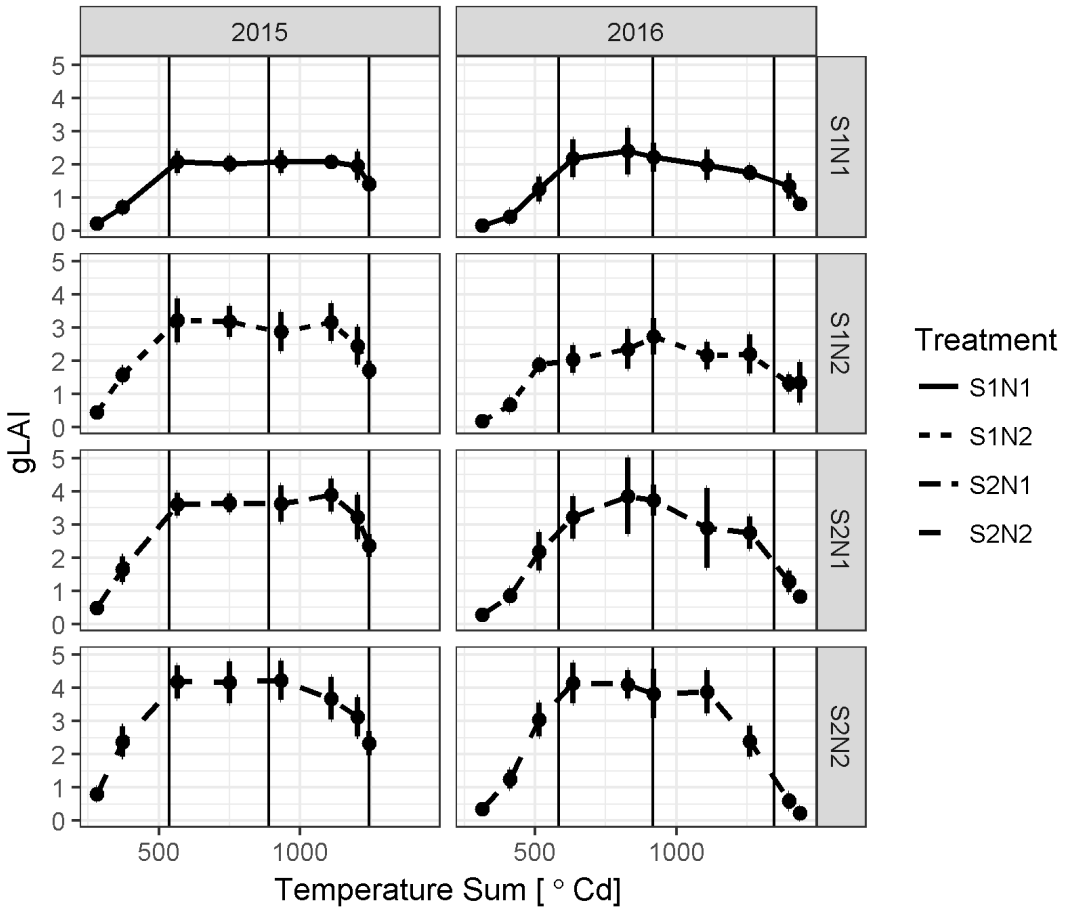

Figure 5.4: gLAI development in the years 2015 and 2016, as per treatment. Error bars show standard deviation. Vertical lines show phenological stages (first line: begin of flowering, second line: Milk-ripe stage, third line: Full ripening).

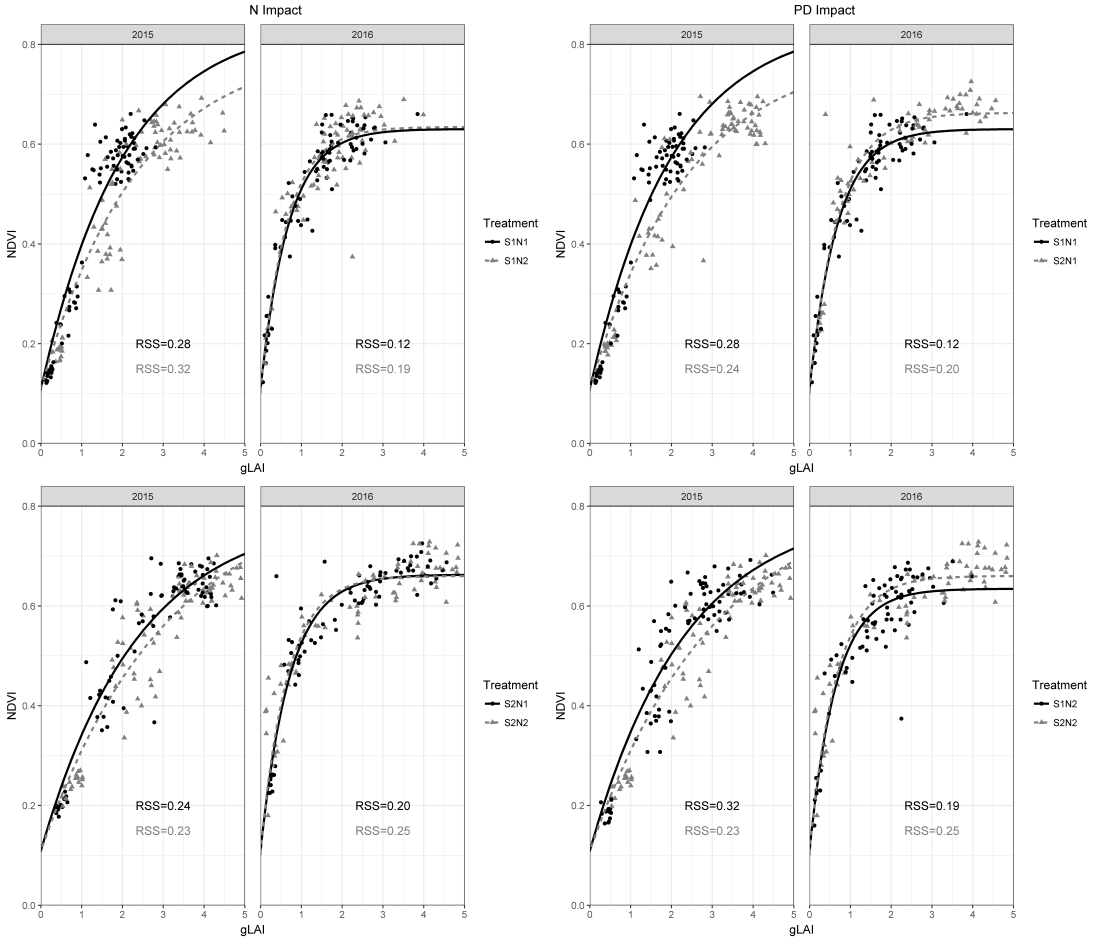

Figure 5.5: gLAI - NDVI relationships per management factor. The left column shows N treatment effects, the right column plant density effects.

densities showed that the point of saturation remained stable, however at different NDVI levels. S2 exhibited higher NDVI values at equal gLAI values. RSS values < 0.32 indicated a good fit for all models, with the tendency of the 2016 models performing better.

Similar to the results above, GNDVI – gLAI models resembled for 2016, and differed for 2015 (Figure 5.6). A clear effect of saturation was noticed in the 2016 data, with gLAI values > 3 not showing an increase in GNDVI values. This effect was not visible in the 2015 data. Models diverged in 2015 for N treatments at low plant density and plant density at low N treatment level, the effect was less strong for the other 2015 models. As for NDVI, models exhibited good fits (all RSS values < 0.33), with the 2016 models performing better. All GNDVI models performed better than NDVI models. No clear saturation effect could

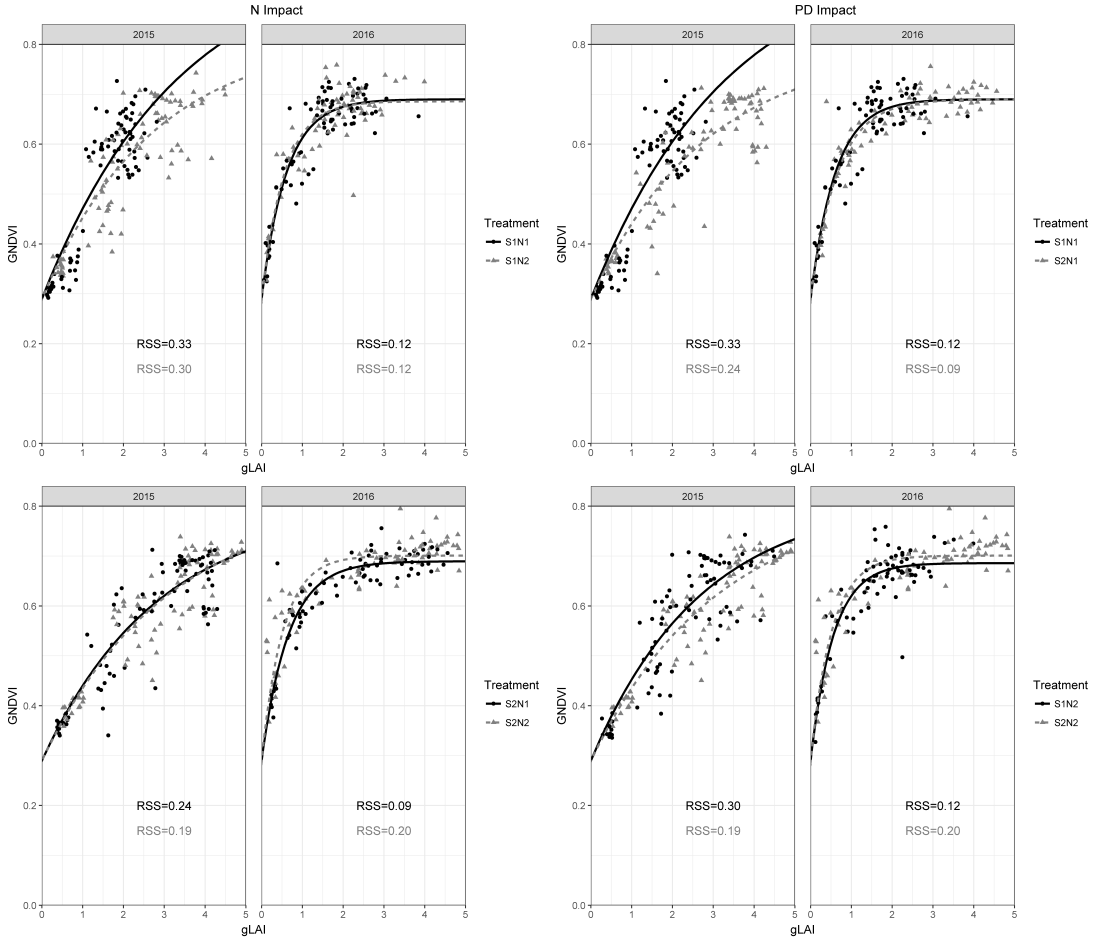

Figure 5.6: gLAI - GNDVI relationships per management factor. The left column shows N treatment effects, the right column plant density effects.

be determined for the 3BSI – gLAI models within the measured range of values (Figure 5.7). Contrary to the NDVI and GNDVI models, this applied to both years. Models in 2016 only diverged at high gLAI values. RSS values were much higher than for NDVI and GNDVI, indicating worse fits. Here, the 2016 models showed better fits.

5.4.3 Influence of gLAI Development on Vegetation Indices

All spectral indices indicated differences between the total mean values of the treatments, with S1N1 exhibiting the lowest value, and S2N2 exhibiting the highest (see tables B-D in the appendix for detailed results). The S2N1 treatment showed higher values than the S1N2 treatment. However, differences between the treatments were not as pronounced as differences between the gLAI measure-

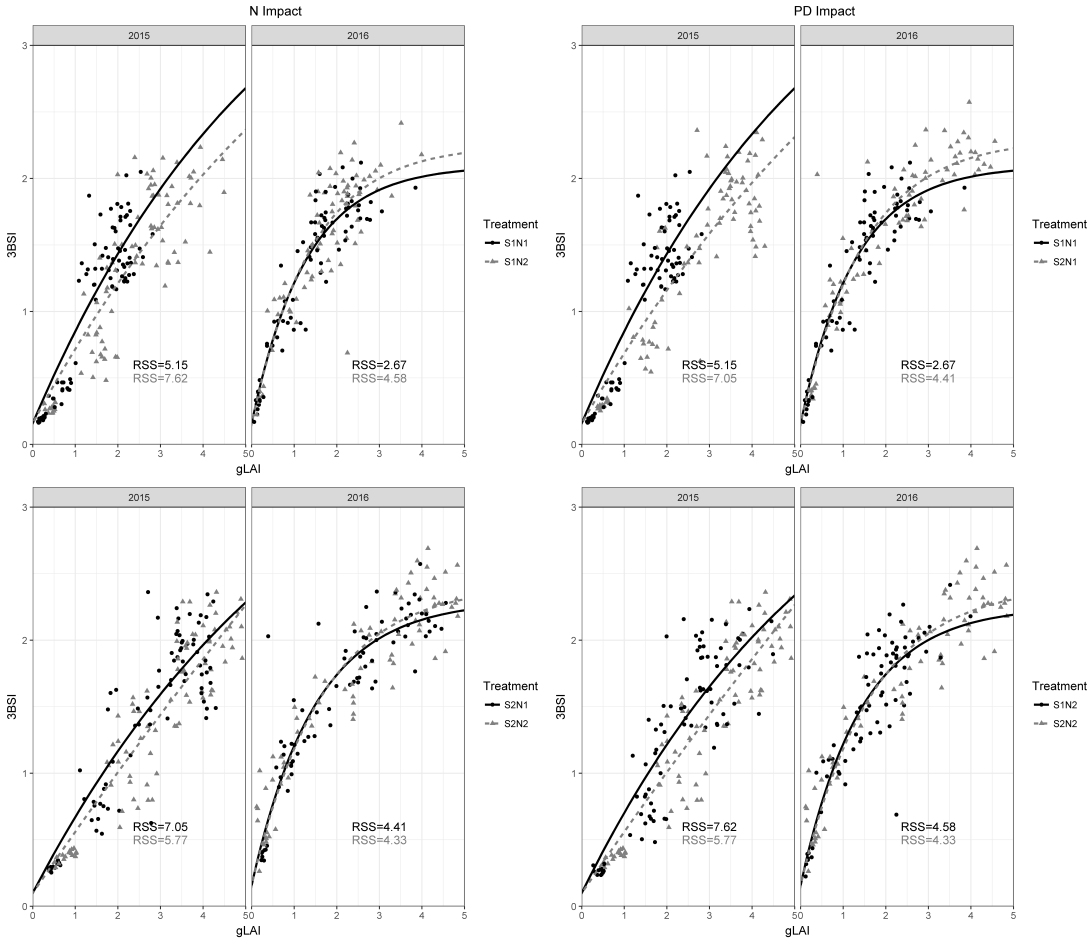

Figure 5.7: gLAI – 3BSI relationships per management factor. The left column shows N treatment effects, the right column plant density effects.

ments. On average, standard deviation of NDVI and GNDVI values were similar. GNDVI showed a lower coefficient of variation than NDVI. The 3BSI values showed greater standard deviation and higher coefficient of variation than NDVI and GNDVI. Absolute lowest values of all indices were found in the in S1N1 treatments, maximum values were found during the flowering and grain filling periods, with NDVI and GNDVI not exhibiting huge differences between the treatments, contrary to 3BSI. The ANOVA for NDVI and 3BSI values showed no difference between the S2N1 and S2N2 trials for both years. The GNDVI ANOVA illustrates no difference between the S1N2 and S2N1 treatments.
Figure 5.8 shows the SVI developments over time, plotted against temperature sum. All three indices showed differences between the treatments during leaf development; NDVI and GNDVI clearly saturated during flowering and grain-filling phase, 3BSI continued to show differences between the trials. Only 3BSI captured the senescence phase adequately.

5.5 Discussion

5.5.1 gLAI Measurement Technique

Contrary to studies that rely on indirect LAI measurement methods via the transmission of radiation in the canopy, we used the direct method of harvesting the maize plants and measuring the area of all leaves within the delimited area. Compared to destructive sampling, indirect methods often underestimate LAI values in maize (Bréda, 2003; Wilhelm et al., 2000). In this study, plants were harvested per area, not per count. Sampling was conducted at uncommon very high temporal resolution (roughly every two weeks). Given the detailed knowledge about plant population and the precision of the measurement method, we have strong confidence in the accuracy of our measured gLAI values.
However, discrepancy remains between the destructively measured area of green leaves and the functional parts of the canopy which influence the spectral signal and are sensed by the cameras, comprising not only leaves, but other parts of the crop, such as stem and husks (commonly referred to as Green Area Index) (Baret et al., 2010; Verger et al., 2014). We are not aware of any literature that discusses a potential influence of green plant organs, apart from leaves, on reflectance and gLAI estimates by remote sensing, especially in bigger crops where organ area is hard to measure. Given the large area of leaves of maize plants, we hypothesize

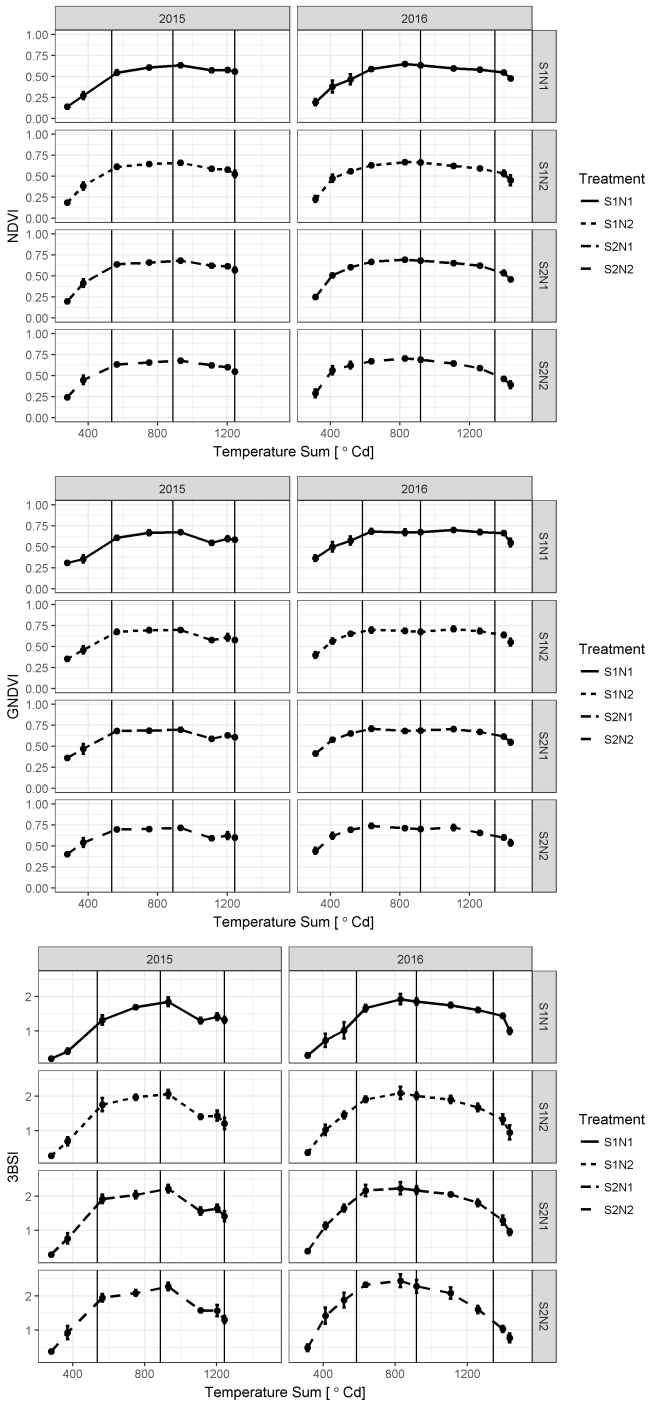

Figure 5.8: SVI development in 2015 (left column) and 2016 (right column). Error bars show standard deviation. Vertical lines show phenological stages (first line: begin of flowering, second line: Milk-ripe stage, third line: Full ripening).

that the influence of other organs to the overall signal is negligible.

5.5.2 SVI Statistics

All three indices managed to capture the general tendencies of the treatments, with S1N1 showing the lowest values, and S2N2 the highest. In general, the coefficient of variation of gLAI values was greater than those of the corresponding SVI values. Given the confidence in our measured gLAI values, we conclude that all spectral vegetation indices derived from our ultra-high resolution UAV imagery failed to capture the variability at multi-plant level in the field. Surprisingly, this was not only the case during flowering and grain filling time when the spectral signal was less responsive, but also during periods of leaf growth and leaf senescence. The 3BSI performed better than NDVI and GNDVI.
The analysis of variance for NDVI and 3BSI showed no significant difference between the high plant density treatments both in 2015 and 2016, contrary to the results of the gLAI analysis. All three SVIs failed to capture the lack of difference between the N treatments in 2016. Additionally, GNDVI indicated no difference between the S1N2 and S2N1 trials for both years. The gLAI data did not show this result. Overall, it is obvious that conclusions drawn from the SVI ANOVAS differed from those drawn from the direct measurements. This puts the sole reliance of management factor analysis on SVIs derived from modified COTS imagery into question; especially when expected gLAI values show asymptotic relationships in the spectral absorption ranges. NDVI and GNDVI curves were only slightly responsive to gLAI changes at values > 3, especially visible in 2016.

5.5.3 Interpretation of LAI Statistics

Including all sampling dates, the interpretation of our analysis of variance indicates that N fertilization differences, plant density differences and the combination thereof show an effect on green leaf area index development in 2015. In 2016, the two different N treatments do not result in different gLAI values. We attribute this to an unequal distribution of rainfall between the years, with 2016 receiving 75 mm more of rain up to a temperature sum of 500. Despite the lack of difference explained above, the treatments lead to different leaf area development dynamics in both years. As expected, low N supply and low plant density resulted in the

lowest gLAI values, high N supply and high plant density in the highest. This development worked out to a range of gLAI values that could be sensed at equal points in time.
Contrary to previous findings in literature, we cannot confirm that high plant densities show greater variability in leaf area development.

5.5.4 LAI-SVI Relationships

The spectral data derived from the employed low-cost cameras delivered meaningful relationships with the measured gLAI data. As expected, NDVI and GNDVI sensitivity saturated at higher gLAI values, however at lower SVI values than assumed from literature. This might be an effect of limited sensitivities and limited dynamic range of the cameras. The gLAI – 3BSI relationship did not saturate within the range of measured values.
Equal gLAI values did not necessarily result in equal spectral vegetation index values, as visible in Figures 5.5 to 5.7. Models especially resembled in 2016, where differences in N application did not show an effect on gLAI development. We therefore assume that, as long as no other factor interferes, the difference in plant density does not show a major effect on the derivation of similar gLAI – SVI models. However, it needs to be taken into consideration that both 50,000 and 100,000 plants ha^{-1} resulted in canopy closure and invariability of values in the visible spectrum due to maximum absorption of light in the canopy. The small differences between models were induced by increased NIR reflectance. We encourage more research to be done on gLAI – SVI relationships in plant densities without canopy closure and/or gLAI values < 3, where the soil contributes to the signal.
Model differences in 2015 were due to a wider spread of SVI values at equal gLAI values. We can only conjecture about the reasons, since unfortunately no variables were measured beyond gLAI. We rule out leaf angle distribution differences as cause since the same cultivar was grown within each year. Differences in chlorophyll content might have caused differences in reflectance, induced by both nitrogen supply and plant density. Effects were especially pronounced in the low nitrogen supply treatment at differing plant densities, and in the low plant density treatment with varying N supply. It is documented that variation in N supply influences leaf structure and composition; lower N uptake results in a lower absorption in the visible range due to a lower pigment content and higher

reflectance in the near-infrared due to smaller and fewer cells (Al-Abbas et al., 1974; Walburg et al., 1982). In 2015, during the early growing states, we observed the highest absorption in the S2N2 treatment and the lowest in S1N1. Initial spectral reflectance in 2015 was twice as high as high as the initial measurement in 2016, with values aligning well after flowering (data not shown). Contrary to this, Ren et al. (2017a) found that chlorophyll content in maize plants decreased significantly with increasing plant density, with densities ranging from 30.000 to 135.000 plants ha^{-1}.

5.5.5 Camera Setup

In all (modified) low-cost commercial off-the shelf digital cameras (COTS), bands have substantial overlap, spectral sensitivity of the bands and wavelength transmittance of filters is unknown, unless exposed to monochromatic light (Berra et al., 2015). We did not examine the spectral sensitivity of the cameras employed, but doubt the correctness of the NIR sensitivities as stated by the provider. Berra et al. (2015) investigated the spectral sensitivity of a Sony Nex7 equipped with a top-notch filter and found that the camera responds to light beyond 900 nm and even to the UV spectrum. Transmission in the NIR range is rather restricted by the sensor substrate than by choice of the filter. This might as well be the case with the RGNIR camera we employed. Due to lower sensitivity in the NIR spectrum, exposure times had to be extended which might have caused a loss in usable dynamic range, especially in the visible ranges.

5.5.6 Possible Shortcoming of UAV-based Imagery

In accordance with the preconditions defined by Rasmussen et al. (2016), we are confident that the quality of the vegetation indices calculated in this study is reliable. All images were acquired during stable illumination conditions. Angular variation is minimised because only pixels close to nadir view were used for mosaicking (roughly all pixels within a radius of about 5 m around nadir view). We are therefore confident that none of the effects discussed above is created or influenced by angular variation. However, more research needs to be done on the question up to what image extent information extracted is reliable.

5.6 Conclusions

Getting back to our objectives, we conclude: Despite poor band segregation, spectral data derived from UAV-based modified low-cost cameras delivered an expressive relationship with measured gLAI values. GNDVI performed slightly better than NDVI; a 3-band combination did not offer any advantages. However, the selected band combinations reached their limits at gLAI values > 3, which is reached in maize well before flowering. Given this, one should be careful when drawing conclusions from SVI values on the impact of management factors on gLAI development, as results might largely be influenced by the signal saturation. Narrowband solutions based on UAV-imaging hyperspectral sensors with band selections in the red-edge and NIR spectrum might perform better and should be focused upon in further research activities.

Despite these drawbacks, we are convinced that UAV-based low-cost COTS camera imagery can greatly contribute to the documentation of gLAI dynamics in crop stands. With this approach, the monitoring is not solely restricted to a few sampling spots in the field, but can cover entire fields at plant level. Heterogeneous growth might be captured, delivering valuable information necessary for site-specific management or for extrapolating crop models from plant to field level. Since most management interventions in maize are conducted before flowering (with gLAI values < 3), the effects of band saturation might not be disadvantageous.

6 Study II: Remote green LAI Estimation in Maize Using UAV-based Modified Consumer Camera Imagery Part II. Improving Parametric and Non-Parametric Regression Performance

6.1 Abstract

Green Leaf Area Index (gLAI) is an important variable in crop growth analysis, and a frequently derived biophysical crop variable in field trials. Remote sensing (RS) facilitates estimation, with UAV-based approaches offering flexible and cost-effective deployment of sensor systems. Extending our analysis from 'Part I: Impact of plant density and nitrogen fertilisation', we evaluated parametric and non-parametric regression methods on their capability to estimate gLAI in maize, relying on UAV-based low-cost camera imagery with non-plants pixels (i.e. shaded and illuminated soil background) a) included in and b) excluded from the analysis. With regard to the parametric regression methods, we tested all possible band combinations for a selected number of two- and three-band formulations as well as different fitting functions. With regard to non-parametric methods, we tested six regression algorithms (Random Forests Regression, Support Vector Regression, Relevance Vector Machines, Gaussian Process Regression, Kernel Regularized Least Squares, Extreme Learning Machine). We found that

all non-parametric methods performed better than the parametric methods, and that kernel-based algorithms outperformed the other tested algorithms. Excluding non-plant pixels from the analysis deteriorated methods' performances. When using parametric regression methods, signal saturation occurred at gLAI values of about 3, and at values around 4 when employing non-parametric methods.

6.2 Introduction

The leaf area index (LAI) is one of the key variable in crop growth analysis due to its influence on light interception, photosynthetic rate, biomass production, plant growth and ultimately crop yield. It is critical to understanding the response of crops to many common crop management practices (Wilhelm et al., 2000), such as fertilizer application and planting density. It is defined as the total one-sided area of leaf tissue per unit ground surface area (Jonckheere et al., 2004), and can be subdivided into photosynthetically active and inactive components (Nguy-Robertson et al., 2012). The former is composed of green leaf area as a photosynthetically functional component and referred to as green LAI (gLAI) (Viña et al., 2011).

Remote sensing (RS) is widely used to detect crop biophysical variables such as gLAI at various spatial and temporal scales. Spectral imagery has the advantage to capture vegetation reflectance of the canopy, which is directly related to gLAI. If based on unmanned aerial vehicles (UAV) as a vertile and flexible platform, measurements can be performed at unprecedented ultra-high spatial resolutions, commonly in ranges from millimetres to centimetres resolution per pixel (Pajares, 2015). Generally, the employment of commercial off-the-shelf (COTS) camera imagery has gained the attention of scientists in recent years (Verhoeven et al., 2009; Verhoeven, 2010; Sakamoto et al., 2011, 2012; Akkaynak et al., 2014; Nijland et al., 2014), especially in UAV-based agricultural applications (Lebourgeois et al., 2008; Hunt et al., 2010; Zhang et al., 2016; Crusiol et al., 2017).

gLAI is a commonly derived variable in field experiments that evaluate the influence of management factors on crops (e.g. fertilizer supply, plant density or pest management). While ground-based estimation for detection of differences or similarities between treatments is time-consuming, labour-intensive and spatially restricted, UAV-based RS covers larger amounts of plots at low-cost and within a short period of time (see Part I of this study).

Verrelst et al. (2015a) developed four methodological categories for general RS based retrieval methods:

i Parametric regression methods: Methods that assume a relationship between spectral measurements and the biophysical variable. An expression is derived from statistics or physical knowledge, containing parameters based on a fitting function that normally hold only for the given spectral data and biophysical variable. Commonly, spectral vegetation indices (SVI) are used as the link to the variable of interest. Models are simple and easy to understand.

ii Non-parametric regression methods: Regression functions are directly determined according to the information from the derived spectral and field data. No assumption about data distribution, spectral band relationships or fitting functions is made. Methods can make use of the full spectral information provided, but are largely considered black boxes. Model weights (coefficients) need to be adjusted to minimize the estimation error of the variables to be predicted.

iii Physically-based methods: Models of cause-effect relationships based on physical laws. The inversion of radiative transfer functions allows for an inference on the variables.

iv Hybrid methods: A combination of non-parametric and physically-based methods. They typically rely on the broad properties of physically-based methods

RS has proven to estimate gLAI accurately with all of the methods categorised above, with most applications based on multispectral satellite data or non-imaging hyperspectral applications. Only few studies have focused on UAV-based derivation of LAI, with different target crops. COTS imagery provides information with great spatial resolution, but with a spectral resolution that might not be known in full detail.
In a parametric regression approach using a modified RGB camera, (Hunt et al., 2010) found the Green Normalized Difference Vegetation Index (GNDVI) to be linearly related to LAI in winter wheat where values were below 2.7 (with an R^2 of 0.85). The index however was not responsive to changes above that value.

In a physically-based approach, Verger et al. (2014) applied a UAV-based multispectral camera to invert the PROSAIL radiative transfer model using the reflectances from 4 bands for the estimation of green area index over wheat and rapeseed. They found that normalized reflectance improved performance of the GAI estimates, particularly under unstable illumination conditions. RMSE for estimates was 0.17 (Verger et al., 2014). Córcoles et al. (2013) used a standard RGB camera to estimate leaf area index of onion via the relationship between estimated canopy cover and LAI. They found that the relationship varied depending on the stage of crop development, with a closer relationship in early growing stages (Córcoles et al., 2013).

To the knowledge of the authors, only few studies have been published so far that investigated RS based LAI estimation applying parametric regression methods. Camps-Valls et al. (2009) used two semi-supervised support vector regression algorithms to estimate LAI in different crops, relying on hyperspectral and simulated multispectral data. The authors found good generalization capabilities, with only a small number of samples (Camps-Valls et al., 2009). Wang et al. (2011) compared multiple linear regression (MLR), partial least squares regression (PLSR) and least squares support vector machine (LS-SVM) methods for the estimation of paddy rice LAI with 15 hyperspectral wavebands. They found that SVM performed better than the other methods. Verrelst et al. (2012a) compared narrowband vegetation indices and GPR for the retrieval of leaf chlorophyll content, LAI and fractional cover based on CHRIS hyperspectral satellite data. GPR outperformed the indices when using at least four out of the 62 bands provided by the sensor (Verrelst et al., 2012a). Yuan et al. (2017) compared random forest (RF), artificial neural network (ANN) and support vector regression (SVR) with a partial least-squares regression (PLRSR) model for the inversion of soybean LAI, derived from UAV hyperspectral remote sensing. They found the RF model suitable for estimating LAI when sample plots and variation are relatively large, and the ANN model more appropriate when sample plots and variation are relatively small Yuan et al. (2017).

A specific problem in estimating either green or total area of leaves or of all plant organs from RS is the mixture of reflective responses of directly illuminated plant organs with those of their background. Further, the spatial resolution of UAV-based RS data may exceed those of the ground truth data. It is then common practice to calculate the average reflectance of all pixels falling within a certain

area, which is subsequently analysed in relation to the respective ground truth data in the same area. The average values, however, might contain signals of illuminated and shaded soil from shadow cast by plants (called 'non-plant pixels' hereafter contrary to 'plant pixels'), and so introduce a source of irritation into the regression that rather aims to capture only the area of plant organs. The major advantage of ultra-high spatial resolution UAV imagery is, however, that it enables to classify for cover of different crop features in an agricultural field, potentially removing factors that might influence the relationship between measured gLAI and the mixed spectral signal of all features within the field of view. This paper adds to our study "Remote green LAI estimation in maize using UAV-based modified consumer camera imagery" which is based on the findings of a two-year maize trial. We investigated the influence of nitrogen (N) fertilization and plant density (PD) on gLAI development, with frequent UAV-based spectral coverage using a set of two modified consumer cameras. Part I (chapter 5) showed that the widely used Normalized Difference Vegetation Index (NDVI), the Green Normalized Difference Vegetation Index (GNDVI) and the 3-Band Spectral Index (3BSI) documented by Verrelst et al. (2015b) all derived from modified low-cost camera imagery hold a strong relationship with field-measured gLAI, when using a parametric regression approach. Management factors, especially N fertilization and – to a lesser extent - also plant density influenced regression parameters, which even resulted in the shift of spectral signal saturation. Based on these findings, in the second part of the study, we posed the following questions:

i Are NDVI, GNDVI and 3BSI the best SVI options for a parametric regression approach when all measurements across the two years and treatments are merged, and annual differences in management and weather impact on crop performance are neglected? Are there other band combinations and/or fitting functions that work better than those mentioned above?

ii How well do non-parametric regression methods perform in estimating gLAI based on COTS camera imagery?

iii Does model performance improve when non-plant pixels are not included in the averaging of pixels across the gLAI sampling area?

To our knowledge, no study has focussed on these questions using UAV-based low-cost imagery. We did not focus on physically-based or hybrid methods as explained above, since the spectral sensitivity of the cameras employed is largely

unknown. Camera manufacturers typically do not release this information, and wavelengths that are transmitted through filters installed in the modification process are mostly not documented (Berra et al., 2015). Thus, we were not able to simulate the sensors' responses in radiative transfer functions.

6.3 Material and Methods

In this section, the field trial, measurement devices and methods as well as the data processing are briefly presented. The reader is kindly referred to Part I of this study for further in-depth information.

6.3.1 Green LAI (gLAI) Field Measurements

gLAI in maize was measured over the course of two growing seasons (years 2015 and 2016) in a field experiment located at Campus Klein-Altendorf (CKA) agricultural research station near the city of Bonn, Germany (6°59′32″E, 50°37′51″N, 184 meters above sea level). The trial consisted of a combination of two N fertilisation (100 kg N ha^{-1} and 200 kg N ha^{-1}) and two plant density treatments (50,000 plants ha^{-1} and 100,000 plants ha^{-1}), which resulted in different development dynamics of leaf area over the course of time.
The hybrid cultivar Panash (AGA Saat, Neunkirchen, Germany) was planted in 2015, the hybrid cultivar Ricardinio (KWS Saaten AG, Einbeck, Germany) in 2016. Both cultivars are similar in their characteristics (FAO number, medium late ripening). Plants were sampled destructively and gLAI was measured in the laboratory using the LI-COR LI-3100C area meter (LI-COR Inc., Lincoln, NE, USA) in approximately 14-day intervals. In 2015, a total of 352 samples were taken on eight sampling dates, in 2016 a total of 304 samples on ten dates. Green LAI was determined by dividing the total leaf area of each plant sample by the ground sampling area (i.e. leaf area / 0.75 m^2).

6.3.2 Collection of Spectral Data and Preprocessing

Spectral data was collected using two Canon ELPH 110 HS digital compact red-green-blue (RGB) cameras, modified by LDP LLC Inc. (Carlstad NJ, United States). Each camera's 1 2/3 inch sized CMOS sensor comprises 4608 x 3456 recording pixels (i.e. 16.1 Megapixels). The first camera (hereafter: RGNIR

camera) was fitted a blue rejection filter, with sensitivity in the red, green and near-infrared (NIR) domain from roughly 800 – 900 nm. Thereby, the spectral information in the blue band was replaced by those in the NIR domain. The second camera (hereafter: BGNIR camera) was fitted with a dual-band-pass filter that blocked light in the red domain; this rendered the sensor sensitive for NIR light in the wavelengths 680 nm to 780 nm. The RGNIR camera delivers R = Red + NIR, G = Green + NIR and B = NIR only, the BGNIR camera delivers B = Blue + NIR, G = Green and R = NIR.

UAV-based camera imagery was collected around solar noon to avoid shadow cast, on mostly cloud-free days, immediately before the sampling of the plants. Images were acquired from an altitude of 50 m (ground sampling distance of 1.5 cm) at nadir view, with a focal length of 4.3 mm and a variable shutter speed that was adjusted from date to date depending on incident light conditions. Three differently grey-scaled reference targets served for the conversion to reflectance values.

Images captured in RAW format were subsequently corrected for lens barrel distortion, vignetting effects and NIR band interference before being converted to reflectance values using the empirical line calibration method. Orthomosaics were created using Agisoft Photoscan Professional (Agisoft LLC, St. Petersburg, Russia).

6.3.3 Extraction of Reflectance Values and Removal of Background Information

We used the raster package (Hijmans, 2016) implemented in R (R Core Team, 2017) to extract the reflectance values within exactly the same ground area of the field where plant each sample was taken. Subsequently, the average reflectance value of each band of the cameras was calculated per sampling plot, i.e. each replicate of the N fertilization and plant density treatments.

In order to classify each image into the components plant tissue, shadow and soil and so to remove non-plant pixels from the data set, the supervised random forest (RF) classifier implemented in the RStoolbox (Leutner and Horning, 2017) was utilized separately for all five spectral bands. RF is a powerful classifier and is readily used in RS studies (Basukala et al., 2017; Rodriguez-Galiano et al., 2012). The classes 'illuminated soil' and 'shaded soil' were subsequently masked and pixel values were replaced with missing values (see figure 6.1 for example).

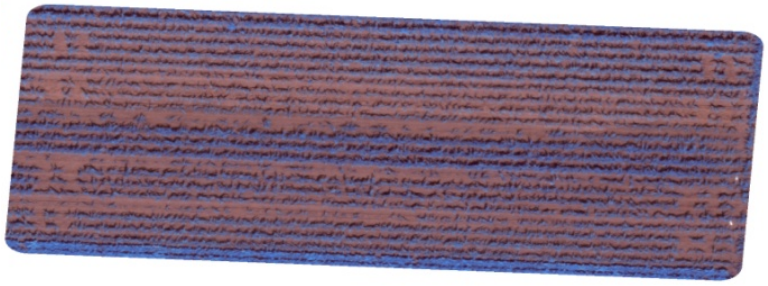

(a) Non-Plant Pixels Included

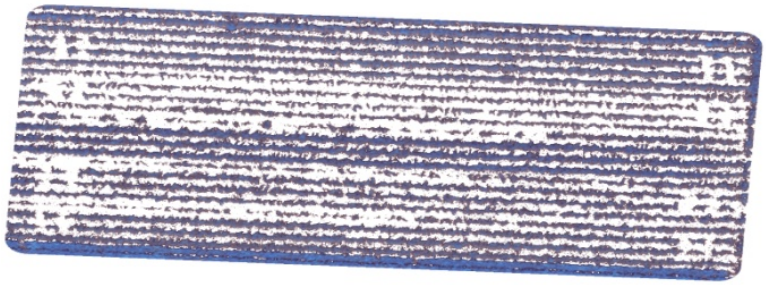

(b) Non-Plant Pixels Removed

Figure 6.1: Example of orthomosaic before (6.1a) and after (6.1b) removal of non-plant pixels. Images acquired on June 25, 2015 with RGNIR camera. Channel combination is R: Red, G: Green, B: NIR. Images show one block of experimental plots. Destructive sampling areas are visible towards the left and right edges of the block.

Pixel values of the sampling plots were extracted and averaged using the method mentioned above, where NA values were ignored in the calculation.

6.3.4 Parametric Regression Methods

We used the spectral indices toolbox (Rivera et al., 2014) embedded in the ARTMO (Automated Radiative Transfer Models Operator) (Verrelst et al., 2012b) software package to test all possible vegetation indices, band combinations and fitting models for reflectance values that do and do not contain non-plant pixel information. The ARTMO package runs in MATLAB and can be accessed at: `http://ipl.uv.es/artmo/` (accessed 22 October, 2017). We split the data into a training and a test data set by taking a simple random sample (with a 70% - 30% apportionment). Model performance using the training set was evaluated based on the estimate of root mean square error ($RMSE$) and the coefficient of determination (R^2). We used the k-fold cross validation resampling technique,

Table 6.1: Types of published indices used in this study and their general formulas.

Type	Formula	Source
Simple Ratio (SR)	$\frac{\rho_a}{\rho_b}$	(le Maire et al., 2004)
Normalized Difference (ND)	$\frac{(\rho_a-\rho_b)}{(\rho_a+\rho_b)}$	(le Maire et al., 2004)
Modified Simple Ratio (mSR)	$\frac{(\rho_a-\rho_c)}{(\rho_b-\rho_c)}$	(le Maire et al., 2004)
Modified Normalized Difference (mND)	$\frac{(\rho_a-\rho_b)}{(\rho_a+\rho_b-2\rho_c)}$	(le Maire et al., 2004)
3 Band Spectral Index (3BSI)	$\frac{(\rho_a-\rho_c)}{(\rho_b+\rho_c)}$	(Verrelst et al., 2015b)
3 Band Spectral Index Wang (3BSI Wang)	$\frac{(\rho_a-\rho_b+2\rho_c)}{(\rho_a+\rho_b-2\rho_c)}$	(Wang et al., 2012)
3 Band Spectral Index Tian (3BSI Tian)	$\frac{(\rho_a-\rho_b-\rho_c)}{(\rho_a+\rho_b+\rho_c)}$	(Tian et al., 2014)

which randomly partitions the samples into k sets of approximately the same size, and fits a model using all samples but one of the subsets. The retained set of samples was predicted by the model and utilized to estimate its performance. Subsequently, the set was returned to the training set, and another set was then retained. The k resampled estimates of performance were subsequently summarized (Kuhn and Johnson, 2013). We used k = 10 as the number of folds and 10 as the number of complete sets of folds to compute. The test set was subsequently compared to the model predicted values to evaluate the accuracy of the model found.

Verrelst et al. (2015b) compiled a list of general index formulations identified in scientific literature, with the majority of formulations extracted from le Maire et al. (2004). We used this list as orientation, but excluded indices based on reflectance signature derivates, as these are derived from continuous spectra of hyperspectral measurements (le Maire et al., 2004), which were not available in this study. Table 6.1 shows the types of indices investigated in this study, where ρ is reflectance, and a, b and c represent the respective bands. Subsequently, each index value was correlated to the measured gLAI value.

6.3.5 Non-Parametric Regression Methods

Non-parametric regression was performed in the caret package (Kuhn et al., 2017) in R (R Core Team, 2017). The *caret* package (abbreviation for **c**lassification and **r**egression training) streamlines algorithms to facilitate the training process of regression and classification models (Kuhn, 2016). It thereby makes use of a number of other *R* packages that implement the algorithms, evaluate the effect of model tuning parameters on performance, choose the best-performing model, and estimate model performance from a set of training data. Table 6.2 lists all non-parametric regression algorithms used in this study, and the method group to which they belong. As for parametric models, performance was evaluated based on the estimate of root mean square error ($RMSE$) and the coefficient of determination (R^2), using the same split dataset. We used the radial basis function kernel for all kernel-based methods, the most widely used kernel in RS (Ghamisi et al., 2017). Method parameters were tuned via the *caret* package, where a candidate set of values is generated and evaluated via a defined amount of model runs (n = 100).

Random Forest Regression (RF)

Random Forests (RF) represent a popular ensemble method that has been widely used in different fields of RS as a classification algorithm, but is rarely applied in regression type analysis (Mutanga et al., 2012). It applies a set of decision trees based on hierarchical connected nodes to improve prediction accuracy, and is capable to deal with complex relationships of discrete or continuous nature. Random Forests is tuned by number of randomly selected predictors to choose from at each split.

Support Vector Regression (SVR)

Support vector regression (SVR) is the implementation of the support vector machines (SVM) method for regression (Smola and Schölkopf, 2004). SVM has found numerous applications in the field of RS because of their ability to handle high-dimensional data with a limited number of training samples (Ghamisi et al., 2017), with publications focussing both on classification and regression problems. Although probably outdated, we recommend Mountrakis et al. (2011) for a thorough review of SVMs in RS. SVR tries to minimize the error by constructing a

hyperplane or a set of hyperplanes that maximize the margin into higher dimensional space. The margin of tolerance is controlled by the ϵ loss function, where all data points with residuals within the threshold ϵ do not contribute to the regression fit, whereas all points with an absolute difference greater than ϵ do by a linear-scale amount (Kuhn and Johnson, 2013). Overfitting is prevented by the user-set cost parameter C, which imposes a penalty on large residuals outside the ϵ margin. The generalization of the regression model is controlled by the kernel function. The estimation accuracy of SVR depends on the good selection of the tuning parameters C, ϵ and the kernel parameters. Kuhn and Johnson (2013) however suggest fixing a value for ϵ and tuning over the other kernel parameters, since there is a relationship between ϵ and the cost parameter, and the latter provides more flexibility for tuning the model.

Relevance Vector Machines (RVM)

The relevance vector machine is a Bayesian approach analog to SVR (Kuhn and Johnson, 2013), and is often used for classification and pattern recognition (Elarab et al., 2015). Parameters have associated prior distributions, and relevance vectors are determined using their posterior distribution. If the distribution is highly concentrated around zero, the prediction equation does not include this sample. Usually, less relevance vectors are constructed in the model than support vectors in an SVR model (Kuhn and Johnson, 2013), but with a comparable generalization function (Tipping, 2001). This results in much faster processing (Demir and Erturk, 2007).
Elarab et al. (2015) used a RVM with LAI, NDVI, thermal and red bands as input to estimate plant chlorophyll concentration over a larger area. The study relied on imagery from a multispectral and a thermal camera mounted on a UAV (Elarab et al., 2015).

Gaussian Process Regression (GPR)

Gaussian Process Regression is another kernel-based machine learning gaining popularity for regression problems. It builds upon the Gaussian Process theory. According to this theory, the learning of the regressor is formulated in terms of a Bayesian estimation problem, where the parameters are assumed to be random variables which are *a priori* jointly drawn from a Gaussian distribution (Pasolli

et al., 2010). The parameters to be tuned comprise magnitude, characteristic length, and noise variance (Hultquist et al., 2014).
Verrelst et al. employed gaussian process regression extensively to estimate biophysical plant variables using RS (Verrelst et al., 2012a, 2016, 2013).

Kernel Regularized Least Squares (KRLS)

Kernel Regularized Least Squares (KRLS) is a machine learning approach that is based on the well-established Regularized Least Squares (RLS) method (Hainmueller and Hazlett, 2014). It is suitable for a range of regression and classification problems, without relying on linearity or additivity assumptions. KRSL constructs a flexible hypothesis space that uses kernels as radial basis functions, and finds the best fitting surface in this space by minimizing a complexity-penalized least squares problem (Hainmueller and Hazlett, 2014). The method is controlled by the two tuning parameters lambda (regularisation parameter) and sigma, which specifies the bandwidth of the Gaussian kernel.
We are not aware of any RS-based publication relying on KRLS regression for estimation of biophysical plant variables.

Extreme Learning Machine (ELM)

The extreme learning machine learning (ELM) algorithm is a feedforward neural network developed for classification or regression applications. It possesses only a single layer of hidden nodes, and does not need any iterative tuning or parameter setting. The input weights and hidden layer bias are randomly chosen and are never updated; the weights between hidden layer and outputs are learned in a single step. The only parameter to be tuned is the number of hidden nodes (Lima et al., 2015). The learning speed of ELM is extremely fast, thereby decreasing the required time for the training of a neural network (Shamshirband et al., 2016), which is especially important when a big data set needs to be processed.
In RS-based applications, ELM was employed in classification of multispectral (Pal, 2009) and hyperspectral images (Bazi et al., 2014; Moreno et al., 2014), but, to our knowledge, not in any regression analysis. It has successfully been used, however, in other predictive environmental applications, such as hydrology (Deo et al., 2016; Rasouli et al., 2012) or climatology (Shamshirband et al., 2016).

Table 6.2: List of non-parametric regression algorithms used in this study.

Group	Name	Source
Decision Tree Learning	Random Forest Regression (RF)	(Breiman, 2001)
Kernel Methods	Support Vector Regression (SVR)	(Vapnik, 1998)
	Relevance Vector Machines (RVM)	(Tipping, 2001)
	Gaussian Process Regression (GPR)	(Rasmussen, 2006)
	Kernel Regularized Least Squares (KRLS)	(Hainmueller and Hazlett, 2014)
Neural Networks	Extreme Learning Machine (ELM)	(Huang et al., 2006)

In this study, we decided not to include Artificial Neural Networks (ANN) in our study due to their complexity. Verrelst et al. (2015b) stated that in the future, ANNs should be replaced with alternative methods that are simpler to train. Furthermore, we did not include linear non-parametric models (e.g. Principal Component Regression or Partial Least Squares Regression) because of the strong nonlinear relationship between gLAI and reflectance in the visible spectrum. Additionally, these methods were designed to deal with collinearity, and perform better if a high number of predictors is given (e.g. a full range hyperspectral spectrum) (Kuhn and Johnson, 2013).
When analysing the correlation matrix of the predictors, we found strong collinearity between the bands in the visible spectrum and the $\rho_{NIR680-780}$ band. To decrease model complexity, we decided to exclude the $\rho_{NIR680-780}$ band. Thus, the following model was fitted to the gLAI and spectral data (equation 6.1):

$$gLAI \sim \rho_{Blue} + \rho_{Green} + \rho_{Red} + \rho_{NIR(800-900)} \tag{6.1}$$

6.4 Results

6.4.1 Parametric Regression with Non-Vegetation Pixels Included

All possible band combinations for the index formulations listed in table 6.1 were tested and analysed. Table 6.3 lists the best-performing band combination and fitting function for each index formulation, with non-vegetation pixels included in the spectral information. Band combinations with a differing order of the same bands and adjusted parameters might perform equally and are not listed here. 3BSI Tian outperformed all other indices, with the lowest $RMSE$ and the highest R^2 for the cross-validation. The other three-band indices (3BSI, 3BSI Wang, mSR and mND) performed worse than two two-band indices, namely Normalized Difference (ND) and Simple Ratio (SR). It is visible that the ρ_{Red} and $\rho_{NIR800-900}$ bands were amongst the best bands in all index formulations. For all formulations except Simple Ratio (SR), an exponential function showed the best fit. Testing the derived combinations against the independent test set

Table 6.3: Cross-validation statistics (R^2 and $RMSE$) for the best-performing band combination and fitting function of each index formulation with non-plant pixels included.

Index Name	Formulation	Fitting Function	Best Bands	$R^2(CV)$	$RMSE(CV)$	$R^2val.$	$RMSEval.$
3BSI Tian	$\frac{(\rho_a-\rho_b-\rho_c)}{(\rho_a+\rho_b+\rho_c)}$	Exponential	a:Red, b:Blue, c:NIR	0.692	0.715	0.753	0.702
ND	$\frac{(\rho_a-\rho_b)}{(\rho_a+\rho_b)}$	Exponential	a:NIR, b:Red	0.689	0.721	0.739	0.725
SR	$\frac{\rho_a}{\rho_b}$	Linear	a:NIR, b:Red	0.685	0.712	0.739	0.684
3BSI	$\frac{(\rho_a-\rho_c)}{(\rho_b+\rho_c)}$	Exponential	a:Red, b:Green, c:NIR	0.669	0.746	0.699	0.776
3BSI Wang	$\frac{(\rho_a-\rho_b+2\rho_c)}{(\rho_a+\rho_b-2\rho_c)}$	Exponential	a:Red, b:NIR, c:Blue	0.636	0.797	0.673	0.824
mSR	$\frac{(\rho_a-\rho_c)}{(\rho_b-\rho_c)}$	Exponential	a:Red, b:Blue, c:NIR	0.616	0.818	0.698	0.799
mND	$\frac{(\rho_a-\rho_b)}{(\rho_a+\rho_b-2\rho_c)}$	Exponential	a:NIR, b:Red, c:Blue	0.604	0.822	0.689	0.783

showed that 3BSI Tian delivered the highest R^2 and SR the lowest $RMSE$. The

scatter plots of the three best performing index formulations (Figure 6.2) show that accuracy decreased beyond gLAI values of 3.

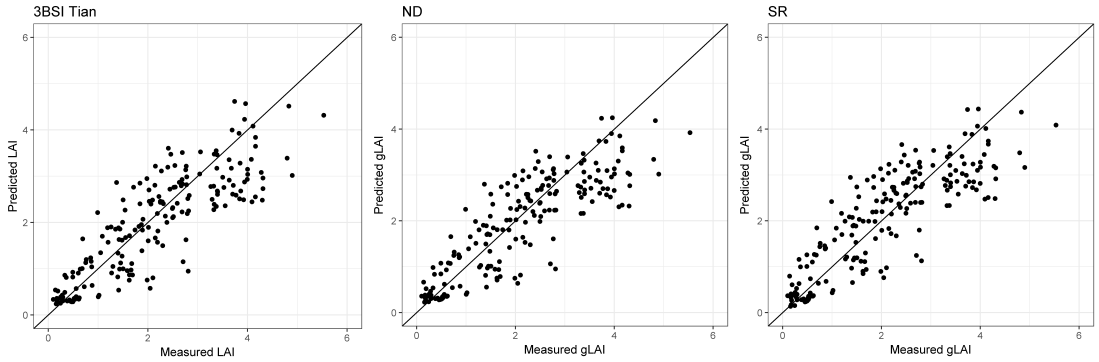

Figure 6.2: Measured vs. estimated gLAI values of the three best-performing index formulations (3BSI Tian, ND and SR) including non-plant pixels, along the 1:1 line.

6.4.2 Parametric Regression with Non-Vegetation Pixels Removed

Table 6.4 lists the best-performing band combination for each index formulation, with non-plant pixels removed. The best-performing indices were 3BSI Tian and ND, which performed equally well (same R^2 and $RMSE$). SR performed better than all other 3-band spectral indices. ρ_{Red} as well as the $\rho_{NIR800-900}$ bands were amongst the best bands. Exponential functions provided the best fit for all index formulations but mSR, where the linear function worked best. Overall, performance of regression with non-vegetation pixels removed was worse than regression with non-vegetation pixels included in the measurements. Testing the models against the validation dataset showed that results deteriorated compared to the dataset that included the non-plant pixels. However, the saturation effect was not indicated as distinctly as above (Figure 6.3).

6.4.3 Non-parametric Regression Algorithms with Non-Vegetation Pixels Included

Table 6.5 shows the results of the cross-validation of all non-parametric regression algorithms, including non-plant pixels. All algorithms outperformed the parametric regression approaches. The best-performing algorithms were Kernel

Table 6.4: Cross-validation statistics (R^2 and $RMSE$) for the best-performing band combination and fitting function of each index formulation with non-plant pixels removed.

Index Name	Formulation	Fitting Function	Best Bands	$R^2(CV)$	$RMSE(CV)$	$R^2(val.)$	$RMSE(val.)$
3BSI Tian	$\frac{(\rho_a-\rho_b-\rho_c)}{(\rho_a+\rho_b+\rho_c)}$	Exponential	a:Red, b:Blue, c:NIR(800-900)	0.680	0.755	0.673	0.712
ND	$\frac{(\rho_a-\rho_b)}{(\rho_a+\rho_b)}$	Exponential	a:NIR(800-900), b:Red	0.680	0.755	0.680	0.702
SR	$\frac{\rho_a}{\rho_b}$	Exponential	a:NIR(800-900), b:Red	0.679	0.766	0.689	0.696
3BSI	$\frac{(\rho_a-\rho_c)}{(\rho_b+\rho_c)}$	Exponential	a:Red, b:Green, c:NIR(800-900)	0.672	0.767	0.682	0.698
3BSI Wang	$\frac{(\rho_a-\rho_b+2\rho_c)}{(\rho_a+\rho_b-2\rho_c)}$	Exponential	a:Red, b:NIR(800-900), c:Green	0.651	0.797	0.669	0.715
mSR	$\frac{(\rho_a-\rho_c)}{(\rho_b-\rho_c)}$	Linear	a:NIR(800-900), b:Blue, c:Green	0.609	0.828	0.601	0.788
mND	$\frac{(\rho_a-\rho_b)}{(\rho_a+\rho_b-2\rho_c)}$	Exponential	a:Blue, b:NIR(800-900), c:Green	0.609	0.849	0.605	0.780

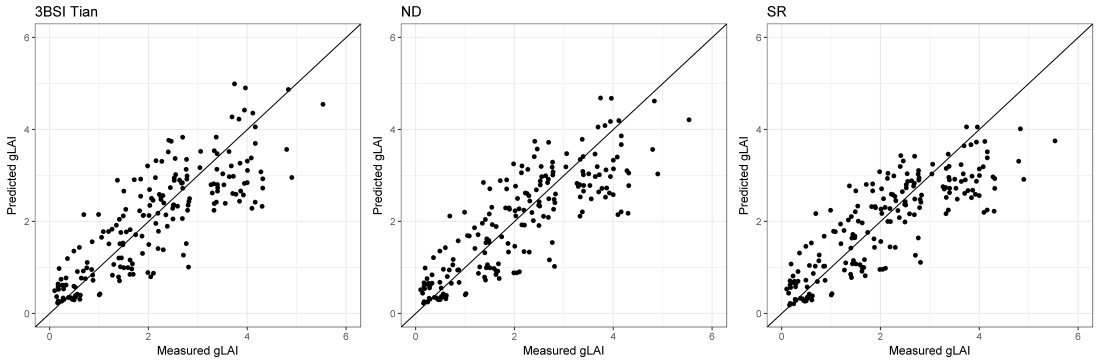

Figure 6.3: Measured vs. estimated gLAI values of the three best-performing index formulations (3BSI, ND and SR) excluding non-plant pixels, along the 1:1 line.

Regularized Least Squares (KRLS), Support Vector Regression (SVR) and Gaussian Processes Regression (GPR), with $R^2 > 0.76$ and $RMSE < 0.64$. Extreme Learning Machine (ELM) performed worse than the other algorithms. The vali-

dation run showed that SVR, GPR and KRLS outperform all other algorithms. Figure 6.4 shows measured vs. estimated gLAI values for the best-performing

Table 6.5: Cross-validation statistics for non-parametric regression algorithms used in this study, with non-plant pixels included.

Name of algorithm	$R^2(CV)$	$RMSE(CV)$	$R^2(val.)$	$RMSE(val.)$
RF	0.758	0.632	0.753	0.652
SVR	0.763	0.626	0.760	0.651
RVM	0.743	0.654	0.745	0.664
GPR	0.762	0.631	0.771	0.632
KRLS	0.765	0.625	0.777	0.622
ELM	0.725	0.673	0.759	0.648

non-parametric models (SVR, GPR, KRLS) including non-plant pixels. Points are scattered closer around the 1:1 line, and no distinct saturation effect can be seen for gLAI values up to 4.

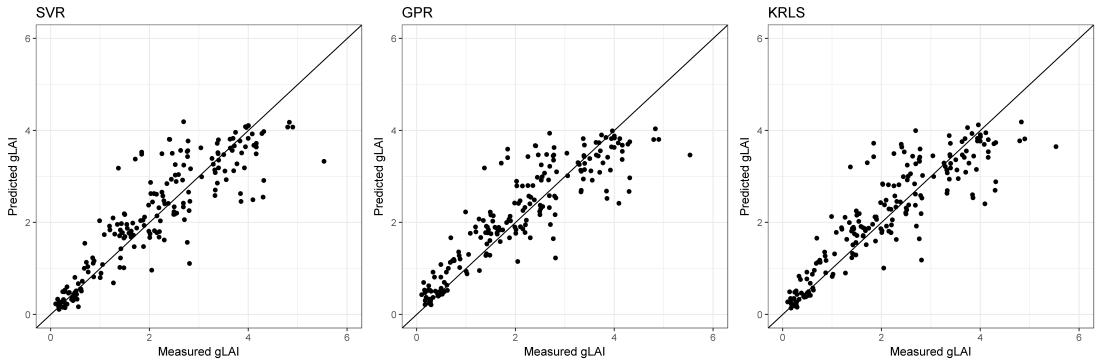

Figure 6.4: Measured vs. estimated gLAI values of the three best-performing non-parametric models (SVR, GPR and KRLS) including non-plant pixels, along the 1:1 line.

6.4.4 Non-Parametric Regression Algorithms with Non-Vegetation Pixels Removed

Table 6.6 displays the results for the cross-validation of all non-parametric regression algorithms excluding all non-plant pixels. As above, Kernel Regularized Least Squares (KRLS), Support Vector Regression (SVR) and Gaussian Processes Regression (GPR) outperformed the other indices, with $R^2 > 0.74$ and $RMSE < 0.657$. Kernel Ridge Regression (KRR) and Extreme Learning Machine (ELM) showed the weakest performance, with $R^2 < 0.68$ and $RMSE > 0.7$.

Furthermore, these two algorithms exhibited a result worse than the best results of parametric regression; all other algorithms provided a better result. The scat-

Table 6.6: Cross-validation statistics for non-parametric regression algorithms used in this study, with non-plant pixels excluded.

Name of algorithm	$R^2(CV)$	$RMSE(CV)$	$R^2(val.)$	$RMSE(val.)$
RF	0.746	0.664	0.709	0.677
SVR	0.743	0.669	0.740	0.634
RVM	0.704	0.719	0.731	0.651
GPR	0.739	0.675	0.741	0.636
KRLS	0.749	0.661	0.744	0.633
ELM	0.666	0.761	0.687	0.694

ter plots of the three best-performing algorithms (SVR, GPR, KRLS) are shown in Figure 6.5. Points are dispersed wider compared to Figure 6.4.

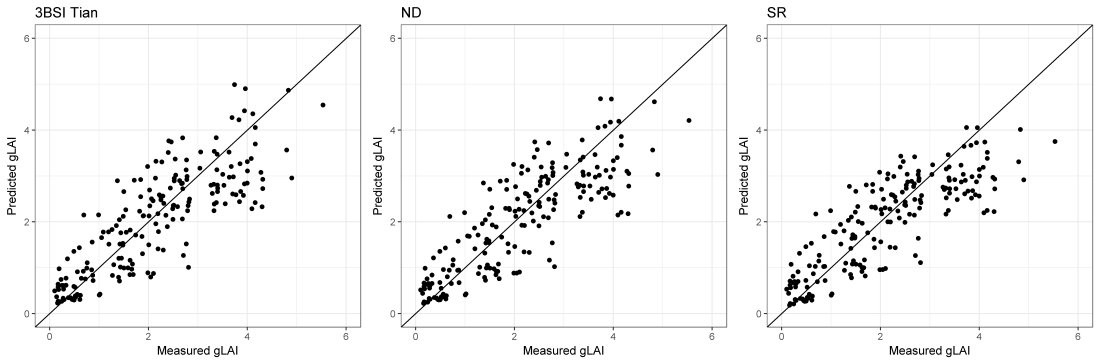

Figure 6.5: Measured vs. estimated gLAI values of the three best-performing non-parametric models (SVR, GPR and KRLS) excluding non-plant pixels, along the 1:1 line.

6.5 Discussion

This study aimed at evaluating parametric and non-parametric regression methods on their capability to estimate gLAI in maize, relying on UAV-based low-cost camera imagery with non-plants pixels (i.e. shaded and illuminated soil background) a) included in and b) excluded from the analysis. This analysis is possible because we relied on ultra-high spatial resolution imagery that allows for separation of plant and non-plant pixels. Furthermore, the flexible employment of the UAV platforms makes the generation of a detailed data set possible. In

the following subsection, we will discuss our employed material and methods in detail.

6.5.1 Camera Set and Imagery

All (modified) low-cost commercial off-the-shelf digital cameras have substantial band overlap, and spectral sensitivity as well as wavelength transmittance of filters is unknown to the end user (see Berra et al. (2015) for an analysis of sensitivities of different cameras). We did not examine the spectral sensitivity of the cameras employed, but doubt the correctness of the NIR sensitivities as stated by the provider. Berra et al. (2015) investigated the spectral sensitivity of a Sony Nex7 equipped with a top-notch filter and found that the camera responds to light beyond 900 nm and even to the UV spectrum. Transmission in the NIR range is rather restricted by the sensor substrate than by choice of the filter. This might as well be the case with the RGNIR camera we employed. Due to lower sensitivity in the NIR spectrum, exposure times had to be extended which might have caused a loss in usable dynamic range, especially in the visible ranges.

6.5.2 Parametric Regression

Our results showed that the widely used two-band indices such as NDVI or GNDVI are not necessarily the best-performing ones to estimate gLAI; it may be worthwhile to test three-band indices as well. In this study, the best-performing index was 3BSI Tian using the band combination a = red, b = blue, c = $NIR_{800-900}$. The NIR band was included in the best bands selection of each formulation, showing that information in the near-infrared is preferable in UAV-based gLAI estimation over standard RGB imagery.
Improving model fit by selecting different fitting functions might make sense from a mathematical point of view; however we would like to stress out that one should consider the underlying physical principles when selecting a fitting function. It is for example well documented that the spectral signal in the visible spectrum saturates at high gLAI levels. Therefore, an exponential function makes sense for normalized difference indices (when $\rho_{NIR}/\rho_{VIS} > 1$, with ρ_{VIS} as a band from the visible spectrum).

6.5.3 Non-Parametric Regression

Non-parametric regression showed good performance, with all algorithms exhibiting R^2 values > 0.72 and $RMSE$ values < 0.67. Especially the kernel methods SVR, GPR and KRLS delivered good results. We assume the strong nonlinearity of the functional dependence between gLAI and reflected radiance leads to good prediction results; furthermore the algorithms exploit the entire provision of bands. Kernel methods are very attractive for retrieval of RS-based biophysical variables because they cope efficiently with low-sized data of potentially high dimensionality, which is the case when models are trained using field-measured data (Verrelst et al., 2013). Verrelst et al. (2012a) pointed out that calculating a vegetation index is not necessary as input for non-parametric regression when those bands are used as direct input. Using the individual bands even showed better performance (Verrelst et al., 2012a).

6.5.4 Effect of Non-Plant Pixels Removal

To our surprise, both parametric regression and non-parametric regression performance was worse when non-plant pixels were removed, compared to non-plant pixels included in the area of measurement and in the models. As already laid out in chapter 5, we attribute this to differing chlorophyll contents in the trials between the years; this resulted in a wider spread of reflectance values at equal gLAI values. This effect is even more pronounced when the influence of soil and shadow pixels on the average value of each sampling area is removed. Soil has higher reflectance in the visible and lower reflectance in NIR spectrum than healthy vegetation, and thus reduces the offset between the contrasting ranges when the average is calculated over an area of different pixels. Given this, we do not see any benefit in removing non-plant pixels from the sampling since their influence does not seem to improve prediction performance.

6.5.5 Parametric vs. Non-Parametric Regression

The comparison between parametric and non-parametric regression methods showed that all non-parametric methods outperformed the parametric ones. R^2 values were higher, $RMSE$ values were lower, and the estimates of the three best-performing algorithms were closer to the 1:1 line. A saturation effect only occurred at $gLAI > 4$ when relying on non-parametric regression methods, and at

$gLAI > 3$ when relying on parametric regression.
Processing speed was not an evaluation criterion in our study. We did not consider this relevant, since our set of measurements was rather small (n=656). It might play a role when dealing with larger datasets; Verrelst et al. (2015b) found that processing the cross-validation statistics of for the best-performing index formulation was considerably faster than processing non-parametric regression algorithms.

6.6 Conclusions

The estimation of gLAI via means of RS has been in focus of research since the 1970s; the emergence of UAVs however has opened up new possibilities and challenges. Our study aimed at improving remote green LAI estimation in maize using UAV-based modified camera imagery by investigating parametric and non-parametric regression methods. Furthermore we were interested in the influence of shadow and soil presence on our model outcome. Our results suggested that non-parametric regression methods outperform the widely-used parametric methods based on spectral vegetation indices. Especially the kernel methods SVR, GPR and KRLS performed well, seemingly able to cope with the non-linear nature of the relationship between gLAI and canopy reflectance. If reliance on parametric regression is needed, one should also look at three-band indices, as our results suggested a better performance than two-band indices. Given the limited number of bands and their broad sensitivities, signal saturation at high gLAI values restricts estimation to maximum gLAI values of 3 when using parametric methods and 4 when using non-parametric methods.
Furthermore, our results showed that model performance possibly even decreases when non-plant pixels are removed from the analysis. This is due to confounding factors that might influence plant reflectance especially in-between different years. When investigating gLAI – spectral data relationships, we suggest to always measure chlorophyll content in a reasonable amount of plants. However, the small difference between the results of inclusion and exclusion of non-plant pixels suggested that it is not necessary to remove non-plant pixels. Further studies on the confounding factors that influence crop reflectance are of great importance for evaluating and improving the methods tested here. Given the ultra-high spatial resolution however, we can think of beneficial effects of separating plant from soil

pixels for cover estimation and analysis of the spatial arrangement of plants in the field.

We assume that our findings are crop-, site- and camera-specific. Marking the start of further research, we suggest studies in maize using the same set of cameras in different locations, later expanding to different crops. What has been presented here for maize in a factorial experiment also offers opportunities for applications at larger spatial extents. The gLAI mapping of time series across large fields or even within agricultural regions and with lower spatial resolution provides useful information on crop performance. The latter is least dependent on water availability, nutrient supply and soil properties and their interaction. The flexibility of UAVs for crop observation allows for the provision of information that is very useful for decision making at various spatial scales, especially for nutrient management, precision farming applications, early stress detection and environmental protection schemes. Further, if combined and interpreted together with phenomapping (Parplies et al., 2016) and existing soil maps, georeferenced gLAI data as key variables of crop growth provide an excellent and easy to derive data source for spatial crop modelling.

7 Study III: Towards Remote Estimation of Radiation Use Efficiency in Maize Using UAV-based Low-Cost Camera Imagery

7.1 Abstract

Radiation Use Efficiency (RUE) defines the productivity with which absorbed photosynthetically active radiation (APAR) is converted to plant biomass. Readily used in crop growth models to predict dry matter accumulation, RUE is commonly determined by elaborate static sensor measurements in the field. Different definitions are used, based on total absorbed PAR (RUE_{total}) or PAR absorbed by the photosynthetically active leaf tissue only (RUE_{green}). Previous studies have shown that the fraction of PAR absorbed (fAPAR), which supports the assessment of RUE, can be reliably estimated via remote sensing (RS), but unfortunately at spatial resolutions too coarse for experimental agriculture. UAV-based RS offers the possibility to cover plant reflectance at very high spatial and temporal resolution, possibly covering several experimental plots in little time. We investigated if a) UAV-based low-cost camera imagery allowed estimating RUEs in different experimental plots where maize was cultivated in the growing season of 2016, b) those values were different from the ones previously reported in literature and c) there was a difference between RUE_{total} and RUE_{green}. We determined fractional cover and canopy reflectance based on the RS imagery. Our study found that RUE_{total} ranges between 4.05 and 4.59, and RUE_{green} between 4.11 and 4.65. These values are higher than those published in other research ar-

ticles, but not outside the range of plausibility. The difference between RUE_{total} and RUE_{green} was minimal, possibly due to prolonged canopy greenness induced by the stay-green trait of the cultivar grown. The procedure presented here makes time-consuming APAR measurements for determining RUE especially in large experiments superfluous.

7.2 Introduction

In agronomy, radiation-use efficiency (RUE, also referred to as light use efficiency LUE) is defined as crop biomass produced per unit of total solar radiation or photosynthetically active radiation (PAR) intercepted by the canopy (Stöckle and Kemanian, 2009). It follows the concept introduced decades ago (Monteith, 1977), where the amount of photosynthates or dry biomass production (g m^{-2}) is expressed as the product of the fraction of absorbed photosynthetically active radiation (fAPAR, with APAR defined as absorbed solar radiation between 400 nm - 700 nm wavelength in MJ m^{-2}) and the efficiency (ϵ) with which the absorbed light is converted into fixed carbon (equation 7.1).

$$DM = fAPAR * PAR * \epsilon \tag{7.1}$$

This concept is widely used in dynamic crop growth modelling (Stöckle and Kemanian, 2009), where daily biomass production is estimated as the product of the amount of radiation intercepted and the RUE for forecasting crop growth and yield. The model's estimation accuracy is affected by limitations of the model itself, because factors influencing biomass production are not considered by the model, and when model parameters or input variables, such as cultivar-dependent RUE, are not available (Morel et al., 2014). Commonly, a constant RUE value is assumed, determined by elaborate field measurements. Unfortunately, there is no standardized procedure to estimate RUE, which has led to various units and experimental approaches (Sinclair and Muchow, 1999). Gitelson and Gamon (2015) point out that there are at least three widely used definitions of photosynthetic RUE based on

i incoming radiation (RUE_{inc}) calculated as

$$RUE_{inc} = DM/PAR_{inc} \tag{7.2}$$

with PAR_{inc} = incident PAR, and DM = dry matter produced,

ii total absorbed light (RUE_{total}) calculated as

$$RUE_{total} = DM/(fAPAR * PAR_{inc}) \tag{7.3}$$

with fAPAR as the fraction of daily PAR absorbed, and

iii radiation absorbed by photosynthetically active vegetation (RUE_{green}) calculated as

$$RUE_{green} = \frac{DM}{fAPAR_{green}} * PAR_{inc} \tag{7.4}$$

with $fAPAR_{green}$ calculated as

$$fAPAR_{green} = fAPAR * (\frac{greenLAI}{totalLAI}) \tag{7.5}$$

where green leaf area index (gLAI) describes the photosynthetically functional leaf tissue per unit ground area, and total LAI the combination of both green and senesced (i.e. brown) leaf area per unit ground area.

The authors furthermore argue that the estimation of crop productivity could be different if different RUE definitions are used, and so they recommend considering RUE_{green} as the standard RUE definition, since it is not confounded by changing pigment and green canopy structure during plant growth and senescence (Gitelson and Gamon, 2015). During the vegetative stage, when LAI_{green} is equal to total LAI, $fAPAR_{green}$ represents the fraction of absorbed photosynthetically active radiation used for photosynthesis. However, during the reproductive stage and subsequent senescence, $fAPAR_{total}$ becomes insensitive to decreasing crop greenness since both, photosynthetic and non-photosynthetic components, intercept PAR_{inc}, while progressively less is used for photosynthesis. Therefore, to obtain a measure of the fAPAR absorbed solely by the photosynthetic component of the vegetation, the fraction of radiation absorbed by photosynthetically active green vegetation ($fAPAR_{green}$) is calculated (Gitelson et al., 2015).
The most widely used method to calculate RUE is to fit a linear relationship between cumulative biomass accumulation and cumulative radiation interception, with the slope of the linear relationship representing the RUE (Sinclair and Muchow, 1999). The determination of RUE_{inc} and RUE_{total} in the field requires the measurement of intercepted or absorbed radiation and dry biomass at time

intervals that are adequate for accurate estimations of both (Stöckle and Kemanian, 2009). The determination of RUE_{green} requires additional measurements of green LAI and brown LAI (i.e. senesced material). Dry biomass used in the calculation usually comprises net aboveground biomass, but not root mass (Sinclair and Muchow, 1999). Absorbed PAR (APAR) is commonly derived as:

$$APAR = PAR_{inc} - PAR_{out} - PAR_{transm} + PAR_{soil} \tag{7.6}$$

with PAR_{inc} representing the incoming PAR radiation above the canopy, PAR_{out} the PAR radiation reflected by canopy and soil, PAR_{transm} the PAR radiation transmitted through the canopy and PAR_{soil} the PAR radiation reflected by the soil (and subsequently absorbed by plant tissue). PAR_{inc} is measured by a sensor above the canopy, pointing towards the sky, PAR_{out} with a sensor pointing downwards towards the canopy. PAR_{transm} is tracked with a sensor placed just above the ground underneath the canopy looking upward, and PAR_{soil} with a sensor placed a few centimetres above the ground, looking downward (e.g. done by (Gitelson et al., 2015; Lindquist et al., 2005; Viña and Gitelson, 2005)).
RUE can be affected by environmental factors such as temperature, radiation and air humidity, or by plant factors such as nutritional and water status, plant development, and source-sink regulation (Stöckle and Kemanian, 2009). It is therefore critical that estimates of crop growth and RUE are obtained under optimal growth conditions (Lindquist et al., 2005). A range of potential maize (Zea mays L.) RUE values have been reported in the literature (see Table 7.1 for a list), with most values ranging between 3.3 g MJ^{-1} and 3.8 g MJ^{-1}.

The overall RUE of a maize crop throughout the growing season strongly depends on the duration of greenness of plant tissue. Recently, the stay green (SG) trait has been identified as an important component in the genetic improvement of several crops to promote stress tolerance and yield improvement (Luche et al., 2015). In maize, this is associated with delayed canopy senescence compared to standard genotypes, which implies a longer period of photosynthetic activity and a longer N retention in the leaves during grain filling, but also lower kernel N concentrations, which might result in lower grain yield (Antonietta et al., 2014). Swanckaert et al. (2017) found, however, that the stay green trait does not necessarily provoke higher assimilate accumulation in the leaves, but is rather a cosmetic one (Swanckaert et al., 2017).
Remote sensing offers potential to reliably estimate the fraction of incoming PAR

Table 7.1: List of maximum RUE values reported for maize.

Source	Average RUE	Based on	Location	Comments
Lindquist et al. (2005)	3.8 g MJ^{-1}	APAR	Sterling, NE, and Lincoln, NE, U.S.A.	Near-optimal growth conditions, five growing seasons, irrigated
Gitelson et al. (2015)	2.24 gC MJ^{-1}	$APAR_{green}$	Mead, NE, U.S.A.	Multiyear observations, irrigated and rainfed, high variability within maize cultivars
Singer et al. (2011)	3.35 g MJ^{-1}	IPAR	Ames, IA, U.S.A.	One growing season, rainfed
Sinclair and Muchow (1999)	1.6 g MJ^{-1} during vegetative growth, 1.7 g MJ^{-1} during reproductive growth	Solar radiation	Various	Review of publications from different locations with different measurement techniques
Claverie et al. (2012)	3.3 g MJ^{-1}	APAR	Toulouse, France	Three growing seasons, irrigated
Dong et al. (2017)	3.41 g MJ^{-1}	APAR	Southern Ontario, Canada	One growing season, rainfed, nitrogen/no nitrogen treatment
Factors for conversion to total solar radiation basis: 0.5 for IPAR, 0.425 for APAR (Sinclair and Muchow, 1999)				

absorbed by active tissue in the canopy, even across larger areas. This is based on the premise that surface structural and optical properties are governed by the vegetation fraction and leaf area index. The interlink is established either via relating fAPAR to spectral vegetation indices (SVI) or via the usage of radiation transfer models (Gitelson et al., 2014). In mixed pixels containing different land covers, precise land cover estimation through remote sensing is challenging. The SVI-fAPAR model is commonly chosen where the spectral reflectance is a linear combination of values of background soil and vegetation (Jones and Vaughan, 2010).

UAV-based remote sensing offers coverage at unprecedented spatial and temporal resolutions due to the low flying altitudes and the versatile, flexible employment of the platform possibly independent from irradiation conditions. UAV-based applications in agronomy comprise biomass estimation via plant height measurements (Bendig et al., 2014; Yue et al., 2017), LAI estimation (Córcoles et al., 2013; Hunt et al., 2010), analysis of phenology (Burkart et al., 2017) and yield prediction (Haghighattalab et al., 2017; Maresma et al., 2016; Zhou et al., 2017), amongst others.

Well-calibrated UAV-based spectral imagery provides reflectance information at much greater detail than other sensors, which reduces the amount of mixed pixels combining soil and vegetation information. This could be used to draw conclusion on the light absorption ability of crop canopies over the course of the growing season, especially within small-scale experimental plots. Furthermore, the spatial resolution allows for the separation of plant tissue, soil and other features in the field.

Based on these findings, we asked:

i Does UAV-based commercial off-the-shelf (COTS) digital camera imagery reflectance data allow for fAPAR estimation support, for ultimately determining RUEs of maize in small-scale experimental plots of variable LAI and biomass development (measured destructively)?

ii Do RUE values of maize derived from this technique differ substantially from field-collected ones reported in the literature?

iii Is there a difference between RUE_{total} and RUE_{green} in the treatments?

We are not aware of any study that partly estimates fAPAR for RUE determination from UAV-based low-cost camera imagery.

7.3 Material and Methods

7.3.1 Study Site and Field Experiment

The field experiment was established in 2016 at Campus Klein-Altendorf (CKA), University of Bonn's own agricultural research facility located southwest the city of Bonn, Germany (6°59′32″E, 50°37′51″N, 184 meters above sea level). Climate is characterized by temperate humid conditions with maritime influence. Long-term average precipitation is 625 mm; average temperature is 9.4°C. The soil is classified as alkaline, nutrient-rich Haplic Luvisol that developed from Loess (Gaiser et al., 2012; Kautz et al., 2010).

The sole purpose of this experiment was to expand plant productivity by formation of different leaf areas; variability in biomass thus resulted from different light absorption over time. Our assumption was to thereby improve the general statement of this study, which could represent heterogeneous growth in a common field. It was not our intention to investigate the influence of management on biomass accumulation.

Established in a random sampling design, the experiment consisted of a combination of two plant densities (PD) and two treatments of nitrogen (N). The plant densities comprised 50,000 plants ha^{-1} and 100,000 plants ha^{-1}, the nitrogen treatments 100 kg ha^{-1} and 200 kg ha^{-1}, respectively. Every treatment was conducted on a plot sized 3 m x 30 m, with 5 repetitions each. Row spacing was 0.75 m (i.e. 4 rows per plot). Nitrogen was applied as inorganic ammonium sulphate (ASN) before planting as one-time treatment. Pesticides were applied according to standard practices, and no irrigation scheme was practised. All treatments were checked for wrongly set plants. Low plant density plots were manually thinned out after emergence.

Rainfall, air temperature at 2 m aboveground and incoming global solar radiation were recorded at the research station's weather station (GWU-Umwelttechnik GmbH, Erftstadt, Germany) in the vicinity of the field.

The hybrid cultivar Ricardinio (KWS Saaten AG, Einbeck, Germany) with stay-green characteristics was grown, which has a recommended plant density, according to the seed producer, of 90,000-95,000 plants ha^{-1} in non-water limited environments (see Table 7.2 for further information, including captured phenological stages according to BBCH scale). The temperature sum was calculated using 8°C as base temperature as confirmed for temperate climates by Birch et

Table 7.2: Basic data about the trial.

BBCH stage	Date	Temperature Sum [°Cd]
Planting Date	04 May 2016	-
Emergence	10 May 2016	44.45
Begin Flowering	15 July 2016	585.72
Fruit Development: Milk-ripe stage	15 August 2016	918.41
Full Ripening	23 September 2016	1346.67
Harvest	29 October 2016	1454.2

al. (2003). Temperatures beyond 30°C were included in the calculation as the maximum temperature of 30°C, since no increased growth was observed beyond that temperature. A total sum of 353.1 mm of precipitation was recorded between planting and harvest. The recorded long-term average (1956-2017) precipitation from May to October is 361 mm (www.cka.uni-bonn.de, accessed Jan 15, 2018).

7.3.2 Leaf Area Index and Dry Biomass Measurements

For measuring leaf area index, 0.5 m of plants in two adjacent rows were sampled destructively at two positions within 4 plots of each treatment at every sampling date (i.e. 4 treatments x 4 plots x 2 samples = 32 samples per sampling date). To minimize edge effects, we did not sample the outer rows of each plot and skipped 0.5 m of standing plants between the collection dates. Four plots (i.e. one plot per treatment) remained unsampled during the entire course of the trial. Samples were immediately transported back to the institute and split into green and senescent material by visual assessment. Green and senescent leaf area was measured separately using the LI-COR LI-3100C area meter (LI-COR Inc., Lincoln, NE, USA). gLAI and brown LAI respectively, was determined by dividing the leaf area of each sample by the sampling area (i.e. leaf area / 0.75 m^2). Samples were taken on ten dates in 2016, with an interval of roughly 14 days. Assessing leaf area by destructive sampling is considered the most accurate method and often serves as calibration for indirect measurement techniques (Jonckheere et al., 2004).

Aboveground biomass was measured from the same samples taken for leaf area measurements. Samples were oven-dried at 105°C for at least 48 hrs until constant weight and weighed subsequently.

7.3.3 Collection of Spectral Data and Preprocessing

Spectral data was collected using two Canon ELPH 110 HS digital compact red-green-blue (RGB) cameras, modified by LDP LLC Inc. (Carlstad NJ, USA). The cameras 1 2/3 inch sized CMOS sensor comprised 4608 x 3456 recording pixels (i.e. 16.1 Megapixels). The first camera (hereafter: RGNIR camera) was fitted a blue rejection filter, with sensitivity in the red, green and near-infrared (NIR) domain from roughly 800 – 900 nm. The information in the blue band was replaced by information in the NIR domain. The second camera (hereafter: BGNIR camera) was fitted with a dual-band-pass filter that blocks light in the red domain; this rendered the sensor sensitive for NIR light in the wavelengths 680 nm to 780 nm. The RGNIR camera delivered R = Red + NIR, G = Green + NIR and B = NIR only, the BGNIR camera delivered B = Blue + NIR, G = Green and R = NIR.

The cameras were mounted inside a frame underneath a Mikrokopter OktoXL6S12 (HiSystems GmbH, Moormerland, Germany) octocopter. Data was collected around noon to avoid shadow cast, on mostly cloud-free days, immediately before the sampling of the plants. Images were acquired from an altitude of 50 m (ground sampling distance of 1.5 cm) at nadir view, with a focal length of 4.3 mm and a variable shutter speed that was adjusted from one campaign to the next, depending on incident light conditions. Three differently grey-scaled reference targets placed next to the field served for the conversion to reflectance values (with nominal reflections of 4%, 16% and 58% of light).

Images captured in RAW format were subsequently corrected for lens barrel distortion, vignetting effects (Burkart et al., 2017; Kelcey and Lucieer, 2012) and NIR band interference before being converted to reflectance values using the empirical line calibration method (Smith and Milton, 1999). Orthomosaics were created using Agisoft Photoscan Professional (Agisoft LLC, St. Petersburg, Russia).

7.3.4 Image Classification and Estimation of Fractional Cover

We classified each orthomosaic into the components plant tissue, illuminated soil and shaded soil (cast from plants) using the supervised random forest (RF) classifier implemented in R's (R Core Team, 2017) RStoolbox (Leutner and Horning, 2017). RF is a powerful classifier and widely used in RS applications based on

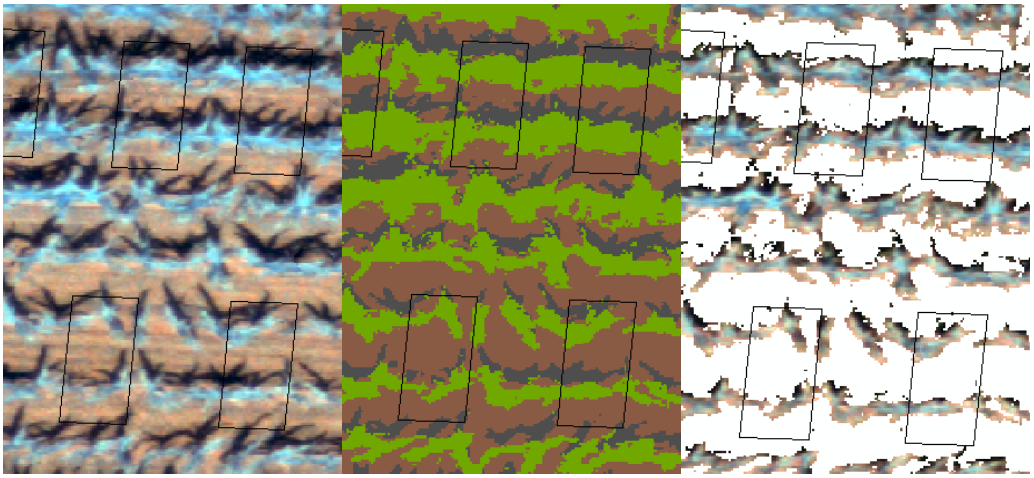

(a) Original Image (b) Classification (c) Soil pixels removed

Figure 7.1: Example of an original image (left), the classification (centre) with green representing plant tissue, brown representing illuminated soil, and black representing shaded soil. The third image (right) shows original image after removal of soil pixels. Black rectangles delineate spots where plants were later sampled destructively for LAI and biomass measurements.

multispectral and hyperspectral data (Ghamisi et al., 2017; Rodriguez-Galiano et al., 2012).

We estimated fractional cover (fCover, i.e. the area of each sampling plot covered by plant material in relation to the entire plot area) to relate reflectance of plant tissue to the gap fraction that would be measured by static sensors in the field. To do this, we divided the number of pixels classified as plant tissue within each sampling plot by the number of total pixels (comprising plant tissue, illuminated soil and shaded soil).

For removal of non-plant reflectances, the classes 'illuminated soil' and 'shaded soil' were subsequently masked and pixel values were replaced with missing values. Pixel values of plant tissue were extracted and averaged within exactly the same ground area of the field where each sample was taken, using the raster (Hijmans, 2016) package implemented in R (R Core Team, 2017). NA values were ignored in the calculation. Figure 7.1 shows the example of an original image, the classification and the image after removal of soil pixels.

7.3.5 Derivation of fAPAR and APAR

$fAPAR_{total}$ and $fAPAR_{green}$ were calculated as shown in equations 7.7 and 7.8. $fPAR_{out}$ describes the fraction of incoming PAR (PAR_{inc}) that was reflected by the canopy, $fPAR_{transm}$ the fraction of PAR_{inc} that was transmitted through the canopy. $fPAR_{soil}$ is the fraction of PAR transmitted through the canopy that was reflected by the soil. fCover describes the fractional vegetation cover in each sampling plot.

$$fAPAR_{total} = (100\% - fPAR_{out} - fPAR_{transm} + fPAR_{soil}) * fCover \quad (7.7)$$

$$fAPAR_{green} = fAPAR_{total} * \frac{gLAI}{totalLAI} \quad (7.8)$$

In order to derive RUE based on UAV-based low cost imagery, we assumed the following:

- The spectrum captured by the blue, red and green bands of the cameras corresponded roughly to the spectrum of photosynthetically active radiation (PAR, 400 nm – 700 nm).
- PAR_{inc} (derived as 0.5 * total solar radiation) measured by the weather station corresponded to PAR_{inc} above the canopy in the field.
- $fPAR_{out}$ corresponded to the average reflectance value (%) that was derived from the red, green and blue bands of the converted camera imagery.
- $fPAR_{transm}$ was not measured directly. We estimated the fraction of PAR transmitted through the canopy by applying the Lambert-Beer law (equation 7.9), where k is the extinction coefficient and gLAI the green leaf area index:

  $$fPAR_{trans} = e^{-k*gLAI} \quad (7.9)$$

  A number of k values have been reported for maize, with recent publications suggesting a range between 0.49 (Lindquist et al., 2005), 0.63 (Liu et al., 2017) and 0.65 (Maddonni et al., 2001) for maize hybrid plants. We selected a k value of 0.55 for our analysis.
- $fPAR_{soil}$ reflects a fixed amount of $fPAR_{transm}$ back into the direction of the canopy, where it is absorbed by the plants. We averaged all pixel values in the class 'illuminated soil', thereby neglecting those influences that vary

soil moisture levels and so affect soil reflectance. An average reflectance of 10% was assumed, based on the average of soil reflectance within the class 'illuminated soil'.

- Temporal increase in fAPAR between sampling dates follows a linear relationship.

- The plants grew free from environmental stresses.

7.3.6 Calculation of RUE

RUE was derived using the cumulative biomass and APAR method, since the majority of studies relies on this method. The amount of PAR that was absorbed by the plants was derived for each sampling date by calculating the definite integral in the plot of cumulated PAR over the growing season vs. $fAPAR_{total}$ and $fAPAR_{green}$, respectively. This value was plotted against destructively-measured dry biomass; the slope of the linear regression indicated the RUE. The entire workflow is illustrated in figure 7.2.

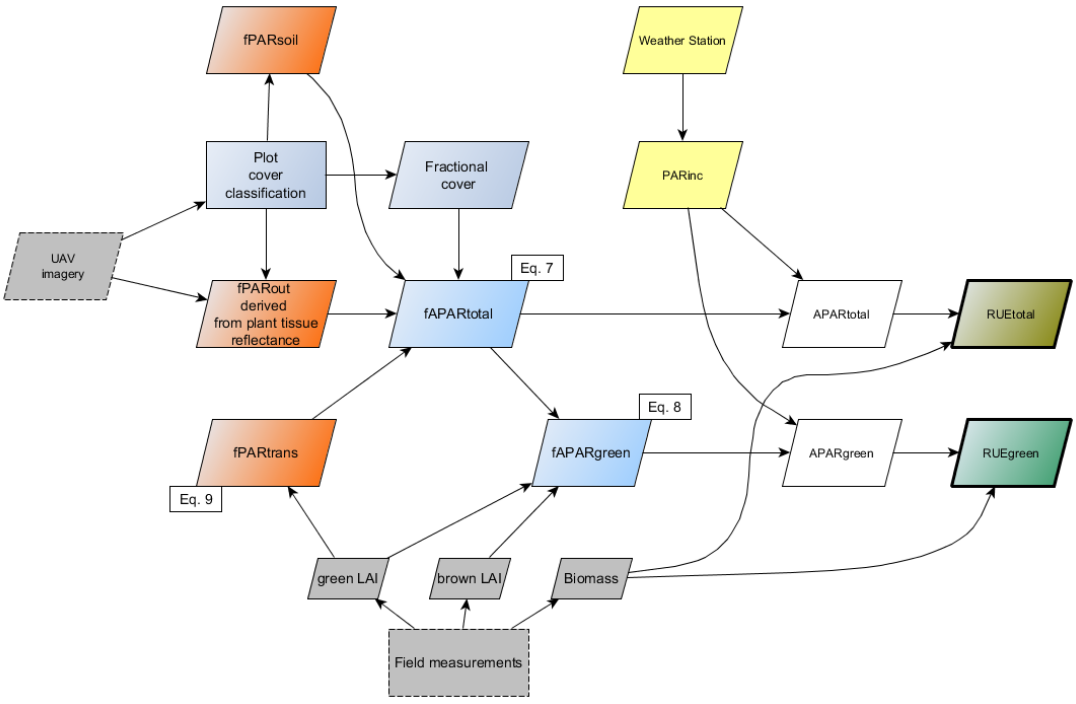

Figure 7.2: Flowchart of RUE_{total} and RUE_{green} estimation method.

7.4 Results

7.4.1 Green LAI, Brown LAI and Fractional Cover Development

The growing season 2016 passed without any major disruptive events. We took the first LAI and biomass samples in mid-June and the last samples in mid-October. The mean gLAI ranged from 0.15 to 0.35 on the first measurement day (15 June, 312°Cd), over 2.2 to 3.83 (15 August, 918°Cd) in mid-season to 0.75 and 2.57 on the last measurement day (16 October, 1436°Cd). Figure 7.3 shows the average gLAI development per treatment. On average, gLAI values >4 were rarely measured, the absolute peak value was 5.53. Lindquist et al. (2005) reported peak gLAI values between 4.8 to 7.8 in different years, Liu et al. (2017) values up to 7.53 and Timlin et al. (2014) average values between 2.2 and 4.28, with peak values between 3 and 5.62.
Mean brown LAI ranged between 0.75 and 2.57 on the last measurement day. Although not in focus of this study, we point out that senescence occurred earlier and faster in the high than in the low plant densities (Figure 7.3). Low plant densities showed more green than brown leaf area at the last measurement date, contrary to the high plant densities.

fCover ranged from 15% to 36% at the beginning of the measurement period. It increased quickly, and reached its maximum in all treatments around 828 °Cd (Figure 7.4), with an average of 88% to 96 % of the measurement plots covered with plant tissue. fCover dropped to an average between 70% and 76% at the end of the growing season.

7.4.2 Biomass Development

The development of average biomass per treatment vs. growing degree days is shown in Figure 7.5. The accumulation followed a typical sigmoidal growth curve, including a decreasing accumulation rate towards the end of the growing season. Measured average values ranged between 14 g m^{-2} and 32 g m^{-2} on the first measurement date and between 1063 g m^{-2} and 1433 g m^{-2} in mid-season. The average biomass measured at the last sampling date (16 October) comprised 1384 g m^{-2} in the S1N1 treatment, 2325 g m^{-2} in the S1N2 treatment, 2225 g m^{-2} in the S2N1 treatment and 2466 g m^{-2} in the S2N2 treatment. In comparison,

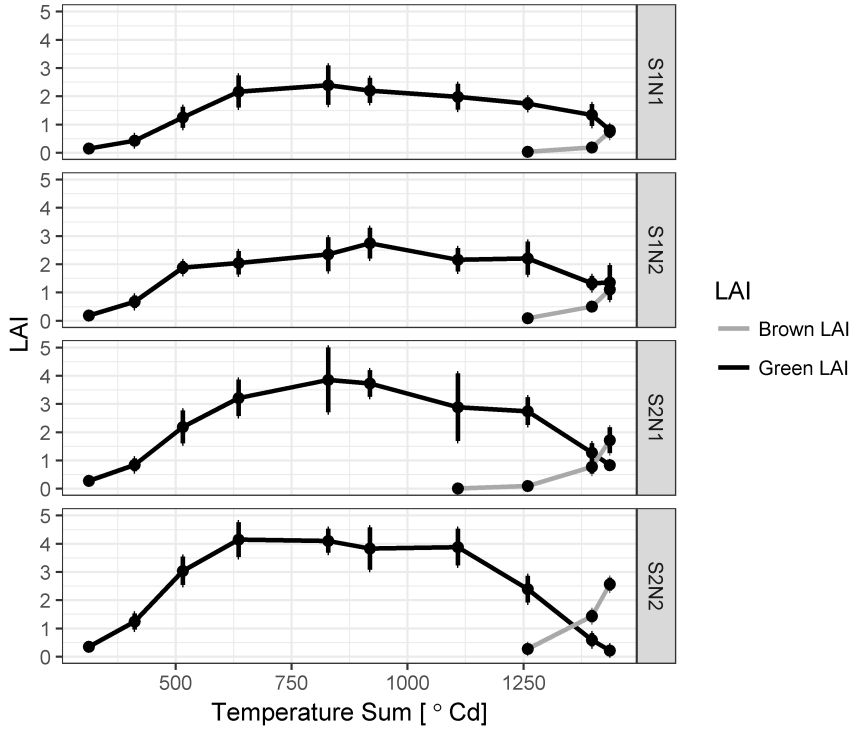

Figure 7.3: Green and Brown LAI development over the course of the growing season 2016. Error bars show standard deviation.

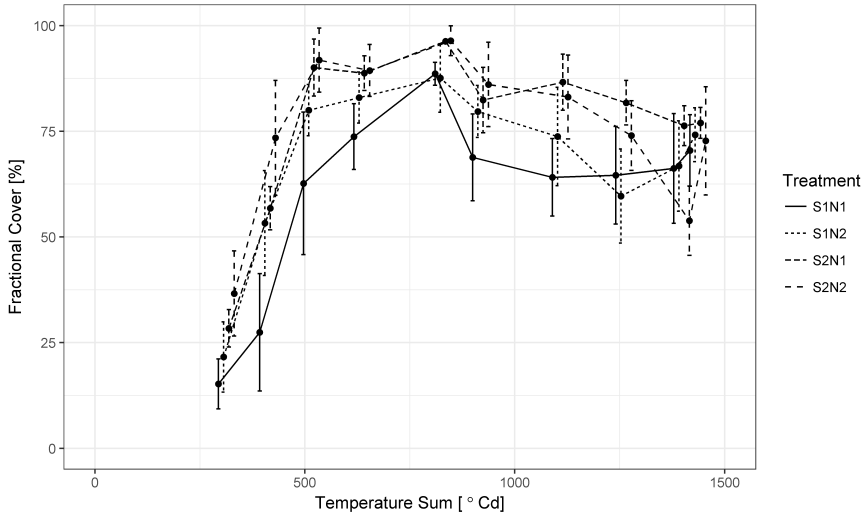

Figure 7.4: Fractional cover development over the course of the growing season 2016. Error bars show standard deviation. The horizontal position was adjusted to avoid overlap.

Lindquist et al. (2005) reported total biomass values at physiological maturity between 2257 and 2916 g m^{-2}, Dong et al. (2017) up to 2500 g m^{-2}.

Given the broad range of measured gLAI and biomass values measured across treatments and over time, the desired variability induced by the field experiment was obtained.

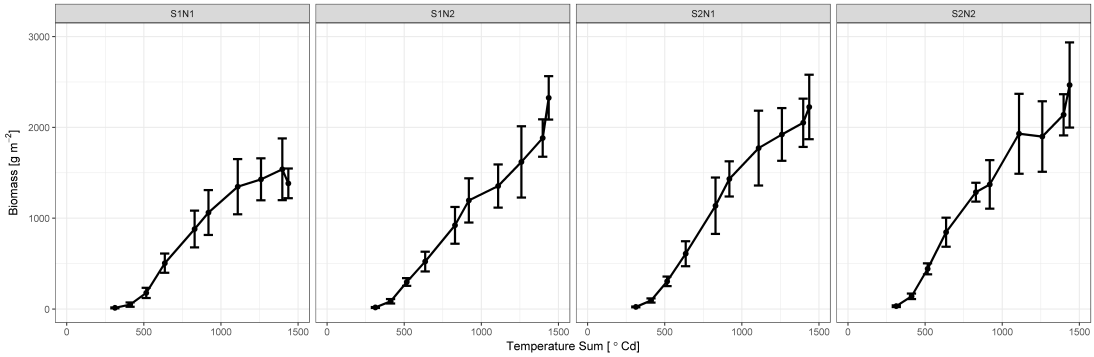

Figure 7.5: Dry biomass development per treatment. Error bars show standard deviation.

7.4.3 Radiation Use Efficiency Development

Figure 7.6 shows the sum of incoming PAR vs. $fAPAR_{total}$ (left) and vs. $fAPAR_{green}$ (right). The course of the curves in both plots was identical until beyond 1000 MJ m^{-2} accumulated PAR. Differences were only visible towards the end of the growing season, where $fAPAR_{total}$ decreased comparatively less due to the stronger influence of reflectance of the senesced leaves. fAPAR of the S2N2 treatment was the highest during most of the growing season, and dropped to the lowest towards the end of the growing season.

Estimated RUE_{total} values for different treatments were 4.3 (S1N1), 4.6 (S1N2), 4.05 (S2N1) and 4.07 (S2N2). Differences to RUE_{green} values were marginal, with 4.33 (S1N1), 4.65 (S1N2), 4.11 (S2N1) and 4.13 (S2N2) reported for the latter (Figure 7.7).

7.5 Discussion

In this study, we determined RUE of maize based on UAV low-cost camera imagery. We are presenting one-year data on the relationship between spectral reflectance of maize canopies, their PAR absorbed and biomass production at the same time intervals. The focal point laid on the capability to derive RUE of maize based on UAV-derived reflectance data rather than on the investigation of

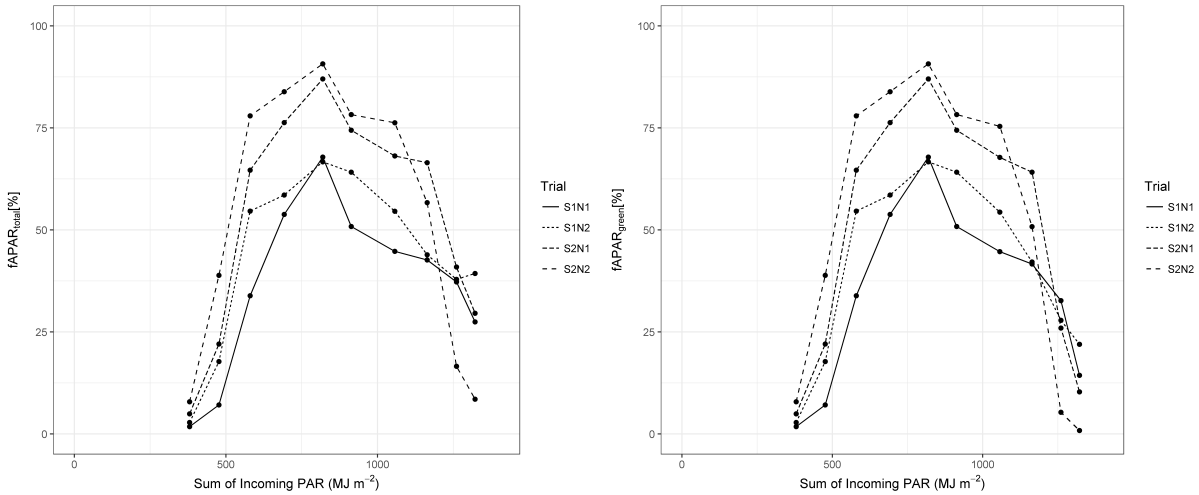

Figure 7.6: $fAPAR_{total}$ (left) and $fAPAR_{green}$ (right) vs. sum of incoming PAR. Each line represents one treatment.

N and PD effects, which might vary between years. $fPAR_{out}$, biomass and LAI were measured biweekly in four different treatments, which resulted in an extraordinary comprehensive dataset, thus making yearly replications of measurement series unnecessary.

7.5.1 Camera Sensitivity

In this study, we assumed that the sensitivity of the red, green and blue bands of the cameras corresponded to the spectral region of PAR. The spectral sensitivity of the bands and wavelength transmittance of filters of most COTS cameras are unknown, unless exposed to monochromatic light (Berra et al., 2015). We did not examine the response of our cameras employed. Berra et al. (2015) investigated the spectral sensitivity of several unmodified and one filter-modified camera, and found that all of the unmodified cameras showed similar ranges within the visible spectrum, with almost all of the RGB channels covering the range of 400-700 nm, but with varying degrees of sensitivity and substantial band overlap (Berra et al., 2015). The filter-modified camera exhibited well-characterized sensitivities in the visible range that were narrower and of more equal intensities than those of the unmodified cameras. We are convinced that, in our case, the influences of varying sensitivities were minimized by the band wise conversion to reflectance values. Admittedly, sensitivity curves generally follow a bell shape (Berra et al., 2015) contrary to PAR quantum sensors, which

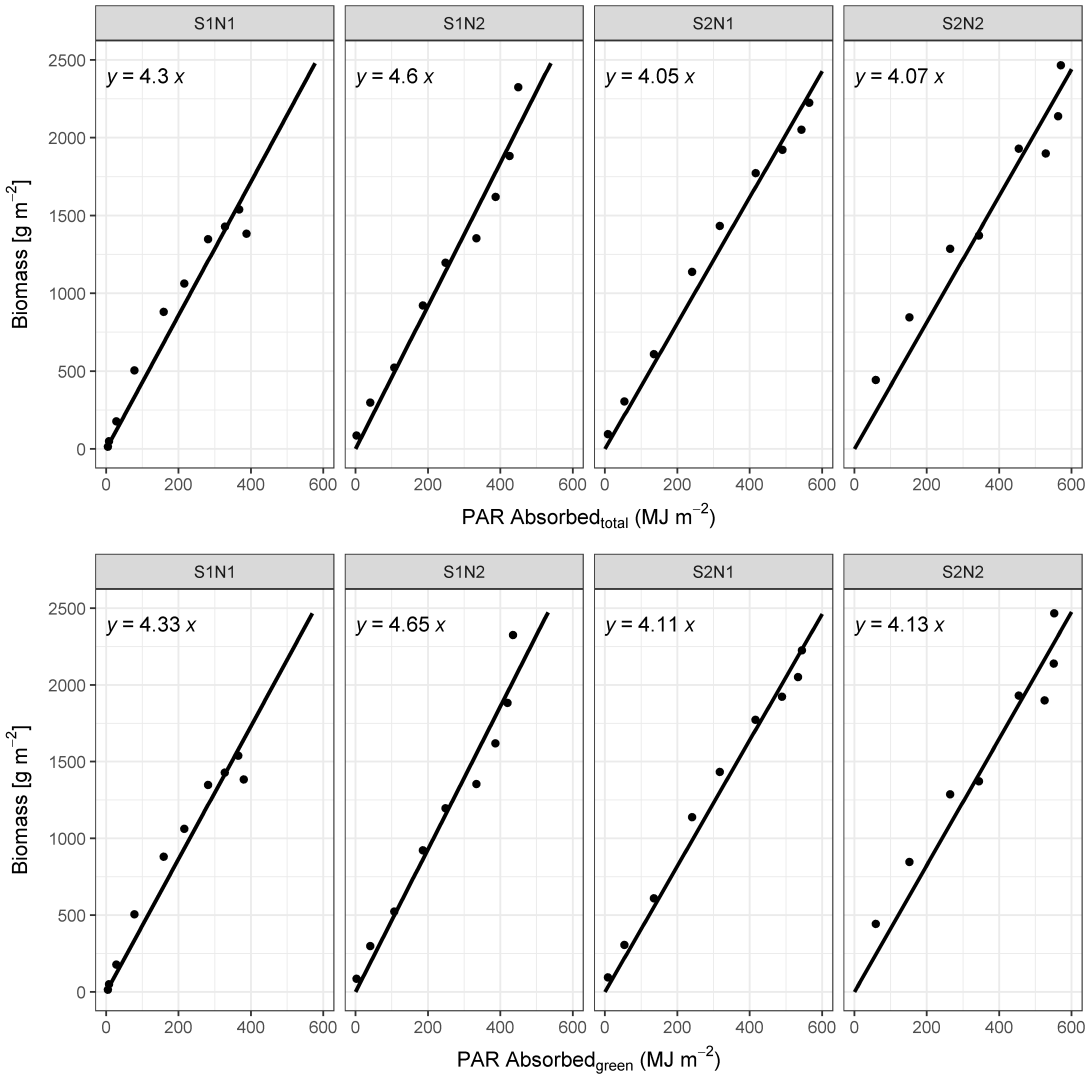

Figure 7.7: Cumulative maize aboveground biomass as a function of cumulative absorbed photosynthetically active radiation. The top row shows relationship per treatment based on $APAR_{total}$, the bottom row based on $APAR_{green}$. The slope of the estimated regression equation is the RUE. The intercept was suppressed.

closely follows the ideal quantum response (Ross and Sulev, 2000). Given this and the overlapping band sensitivities, we are uncertain to make a statement about whether our approach tended to under- or overestimate true PAR reflectance. We encourage future researchers to look into this subject matter.

7.5.2 Green and Brown LAI Development and Measurement Techniques

For this study, green and brown LAI was measured to calculate RUE_{green}. Contrary to studies that rely on indirect LAI measurement methods via the transmission of radiation in the canopy, we used the direct method of harvesting the maize plants and measuring the area of all leaves within the delimited area. Compared to destructive sampling, indirect methods often underestimate LAI values in maize (Bréda, 2003; Wilhelm et al., 2000). In this study, plants were harvested per area, not per count. Sampling was conducted at uncommonly very high temporal resolution (roughly every two weeks). Given the detailed knowledge about plant population and the precision of the measurement method, we have strong confidence in the accuracy of our measured green and brown LAI values. However, discrepancy remains between the destructively measured area of green leaves and the functional parts of the canopy which influence the spectral signal and are sensed by the cameras, comprising not only leaves, but other parts of the crop, such as stem and husks (commonly referred to as Green Area Index) (Baret et al., 2010; Verger et al., 2014). We are not aware of any literature that discusses a potential influence of green plant organs, apart from leaves, on reflectance and gLAI estimates by RS, especially in taller crops where organ area is hard to measure. Given the large area of leaves of maize plants, we hypothesize that the influence of other organs to the overall signal is negligible.

7.5.3 fAPAR Calculation Assumptions

Light attenuation in maize is influenced by canopy architecture, defined in terms of the size, shape and orientation of the aboveground components of the plant (Maddonni et al., 2001). Canopy architecture is influenced by various factors such as management via plant density (Timlin et al., 2014) and row spacing (Andrade et al., 2002), as well as cultivar-specific properties (plant height, leaf number, leaf angle distribution). Modern maize hybrids usually have erect leaves above the ear and flat leaves below the ear (Huang et al., 2017), with erectophile hybrids usually associated with k values <0.5 (Ma et al., 2014). Huang et al. (2017) recently found k values between 0.56-0.74. This shows that estimation of canopy transmittance via the Beer's law remains a great source of uncertainty.
Contrary to other studies estimating RUE in maize, we did not cultivate the

maize crops under irrigated conditions. We assume that water stress did not occur at any time, given the amount of precipitation that fell over the course of the growing season. We furthermore calculated soil moisture retention from data of a physical soil properties analysis (Gaiser et al., 2012) and concluded that soil-moisture tension did not exceed pF values of 3 in 30 cm soil depth until flowering, and at no point in time in 60 cm and 90 cm soil depth (soil moisture measured with EC-5 sensors (Decagon Devices Inc., Pullman, WA, USA) installed in-between the two mid-rows of the unsampled plots, data not shown). Additionally, we did not observe leaf rolling, which is one of the main plant reactions to water stress. Given this, heat stress was also assumed to be minimal, since the critical canopy temperature is generally reduced by the cooling effect of water transpiration (Gabaldón-Leal et al., 2016).

Our approach furthermore assumed that PAR_{soil} absorbed by the canopy comprises radiation transmitted through the canopy only; we neglected directional or diffuse reflection from the surrounding area of the plants. The influence was possibly larger during early growing stages before canopy closure. Especially illuminated soil in-between the rows, which was not covered by leaf tissue yet, could have contributed to PAR absorption to a larger extent. Additionally, the contribution of varying soil moisture to the PAR_{soil} remains unknown. Wet soils commonly reflect less PAR than dry soils (Lobell and Asner, 2002). A number of studies neglected PAR_{soil} altogether, assuming to have only little influence on APAR (e.g. (Lindquist et al., 2005; Tollenaar and Aguilera, 1992)). Gallo and Daughtry (1986) found that intercepted PAR (i.e. 1-PAR_{trans}) overestimated APAR in a maize canopy throughout most of the growing season by less than 4%, which emphasizes the little influence of PAR_{soil} on total APAR.

7.5.4 RUE Values

The RUE values derived in this study were higher than those published in recent articles. Lindquist et al. (2005) found an RUE of 3.8 g MJ^{-1} APAR for aboveground biomass accumulation, PAR_{soil} was not measured. We consider the values presented here plausible, given the trends in biomass increase induced by improved plant breeding. Biomass increase in modern maize hybrids is mostly attributable to higher plant density tolerance (Antonietta et al., 2014), which results from increased light intensity in the mid and lower canopy layers. Maize adapts to increased density by increasing leaf spacing below the ear and the leaf

orientation above the ear, and by reducing leaf width and leaf angle (Gou et al., 2017). Lower RUE in high plant densities could be a result of decreased absorption efficiency due to more self-shading.

In agreement with Lindquist et al. (2005), we also cannot support the common perception that RUE declines during grain fill. Both absorption and biomass increase occurred until the last sampling date.

Unfortunately, no statistical analysis was possible to determine differences or similarities between RUE_{green} and RUE_{total}, and the impact of different treatments. RUE_{green} and RUE_{total} values of the same treatments did not differ considerably. Figure 7.6 furthermore suggests that a difference between $fAPAR_{total}$ and $fAPAR_{green}$ only occurred towards the end of the growing season, around the full ripening stage. The influence of the stay green trait possibly caused this; the longer maintenance of greenness resulted in a weak influence of senesced material to plant reflectance. Although both approaches produce similar results, we nevertheless recommend relying on the RUE_{green} concepts, since the onset of senescence is both cultivar- and weather driven.

Since root mass is difficult to measure, it is commonly not included in RUE estimations. The inclusion would inevitably result in higher values. Root mass of maize around anthesis may comprise 15% to 40% of the total crop mass. N fertilization might decrease root mass or show no impact at all (Anderson, 1988).

As mentioned above, we computed RUE via cumulative APAR. However, Mitchell et al. (1998) pointed out that this method gives false confidence in the true actual value of RUE and so obscures all variation in RUE with time. In fact, the temporal behaviour of RUE is characterized by short term facultative (day-to-day) and long term constitutive (seasonal) variations (Gitelson et al., 2015). RUE_{green} can vary more than 3-fold over the season with no clear pattern, and additionally show day-to-day variability, depending on the physiological status of the vegetation. The daily variability of PAR also causes RUE_{green} day-to-day oscillation, with a decrease due to excessive PAR_{inc}, which cannot be efficiently used by the maize plant. The long term variation is affected by the physiological status and phenology, furthermore by the temporal changes of green and brown plant tissue (Gitelson et al., 2015).

7.6 Conclusion

This study showed that UAV-based reflectance data derived from low-cost camera imagery could be used to support the derivation of RUE values in small-scale experimental plots (provided that the data is well-preprocessed). The great advantage of this approach is that fractional cover and $fPAR_{out}$ as necessary inputs for the calculation of RUE can be sensed over larger areas, and not just point-based. Possibly, the above-mentioned variables could be mapped at small spatial scales (e.g. m^2) in fields, thereby revealing heterogeneous patterns that would otherwise remain undetected. A cultivar-dependent RUE derivation is possible; this gives crop modellers the chance to improve radiation-driven crop growth models. gLAI can also be mapped with the help of UAVs and multispectral or hyperspectral cameras; the mapping of brown LAI is encouraged to be focus of research in future activities. First studies on the estimation of standing biomass in cereals via UAV-based RS were recently published (Bendig et al., 2014; Li et al., 2016; Yue et al., 2017). Taking this under consideration, the need for labour-intensive, costly field measurements could be reduced to a minimum.

8 Synthesis

The research that was documented in this thesis was motivated by the need for estimation of biophysical crop variables in agronomic field experiments, where plots are commonly numerous and small. UAV-based RS delivers data with ultra-high spatial and temporal resolution, since the sensor-carrying platform can be employed flexibly and the sensor is close to the object of interest.
As was shown, our approach relying on a set of modified COTS cameras offers potential to estimate the two very important crop variables gLAI and RUE accurately and contactless. All results of this thesis should, however, be considered under limitations documented as follows.

8.1 Limitations

8.1.1 The Field Experiment

The field experiment as the foundation of this study was set up at Campus Klein-Altendorf, which is characterized by generally favourable growing conditions and fertile soils. The primary intention of the experiment with its four treatments was to develop a broad range of leaf area being measurable simultaneously, over different points in time.
As the data showed, this occurred only partly. The 2016 trial showed no significant differences of leaf area between the different N levels in both low and high plant densities. Prevailing N availability and N nitrification before planting was probably already at a high level, which resulted in no significant differences in gLAI development between the N trials. It is therefore recommended to account for residual nitrogen in field experiments and to choose extremely different N fertilisation rates on these fertile soils (e.g. 0 kg ha^{-1} - 300 kg ha^{-1}) to ensure the effect on maize leaf growth.
Furthermore, the differences in reflectance at equal gLAI values between the years were unexpected (probably caused by different N nitrification rates), which is why

chlorophyll content was unaccounted for in our measurements.
Change of cultivars between the years did not happen for research purposes. The seeds of the cultivar that was grown in 2015 were not available for purchase in 2016 any more.
In a nutshell, it can be said that a number of uncertainties remain in field experiments that cannot necessarily be accounted for.

8.1.2 The Regression Models

Commonly, regression models between spectral data and biophysical crop variables are crop, sensor- and site-specific (Homolová et al., 2013). We therefore assume that a recalibration of the models derived in this study is necessary if the given set of cameras is used in a different location and/or for a different crop. Furthermore, a recalibration is needed if the sensor system is a different one. Considering this, the applicability of the derived models under different side conditions is limited, the methodological approaches, however, are not.
Taking the restrictions of the gLAI regression models into account, the explanatory power at later growing stages of crops remains limited. This is when the plants reach gLAI levels >4, and no distinction is possible via our UAV-based approach. To overcome this issue, narrowband solutions that include information from red-edge and NIR should be investigated (see below).

8.2 Contributions to Knowledge

The findings presented in this thesis, including the three studies in chapters 5, 6 and 7 can be summarized in their contribution to scientific knowledge and the overall objectives of this study (chapter 2) as follows and have not been published up to date in any other study:

- The employed platform (UAV) and sensor (low-cost cameras) combination enables the user to cover larger maize field experiments with ultra-high spatial resolution RS imagery repeatedly, effortless, in little time and under illumination conditions different from clear blue skies;

- Elaborate preprocessing of the RAW data captured by the set of cameras is necessary before the analysis is possible;

- The data derived from UAV-based modified COTS camera imagery can be used to estimate gLAI and RUE (via the estimation of fAPAR and fractional cover) in different treatments of maize in experimental plots;

- A good estimation of gLAI is possible until values of around 3 when relying on spectral vegetation indices, the signal saturates at greater values. This implies that values >3 cannot be determined using this approach.

- Non-parametric regression methods perform better in their gLAI estimation accuracy than SVIs; an estimation of gLAI values >4, however, is not possible;

- Apparently, a general model across different treatments relying on SVIs for gLAI estimation can only be derived at the expense of overall accuracy;

- A sole reliance on vegetation indices is not recommended to determine influences of management factors on gLAI development;

- The exclusion of non-plant pixel does not improve both parametric and non-parametric regression performance substantially and is therefore not necessary for gLAI prediction via UAV-based RS.

8.3 Feasibility of COTS Cameras for Variable Estimation

This study relied on a set of COTS cameras that was modified with filters developed in-house by the modifying company. The exact spectral responses of the cameras were unknown due to the lack of documentation, and to our knowledge, no published study investigated this particular set of cameras. Berra et al. (2015), however, inspected the spectral response of a modified Sony camera equipped with the same filter as the RGNIR camera employed in this study (see figure 8.1 for spectral response curves). They found a much lower sensitivity in the NIR range than in the visible ranges. Additionally, they surprisingly determined sensitivity of the camera to light in the UV range. It is therefore likely that the RGNIR camera employed in this study exposed the same characteristics; the magnitude of likely influence, however, is impossible to quantify.

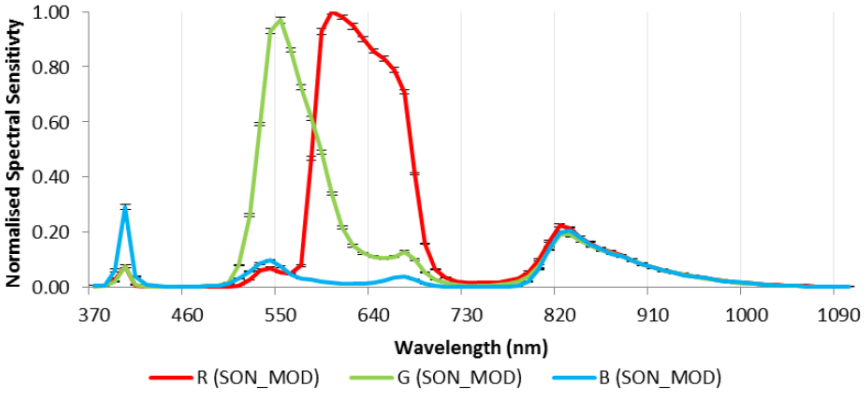

Figure 8.1: Spectral response of a modified Sony camera, equipped with the same filter as the RGNIR camera employed in this study. Data is normalised to the peak of the red channel. Source: Berra et al. (2015)

As shown in figure 3.10 on page 22 and figure 8.1, COTS cameras exhibit overlapping and varying sensitivities in different bands. In contrast, costly sensors developed for scientific purposes show distinct sensitivities without overlap and a similar magnitude. Both types commonly cover the ranges of the electromagnetic spectrum that are influenced by varying leaf area (visible and NIR spectral range), where transitions along the spectrum occur smoothly rather than sharply (see a typical curve of vegetation reflectance in figure 3.2 on page 10).

With respect to the estimation of gLAI, we do not assume a vast performance difference between the two types of cameras as long as the same parts of the spectrum are included in the model. Signal saturation will definitely occur at higher gLAI levels, since this condition is an optical property caused by plant architecture and not by the camera type. Nevertheless, we strongly encourage research comparing the results of the different camera types.

Narrowband solutions, however, might overcome the saturation problem. They rely on bands with small widths covering parts of the electromagnetic spectrum that are not prone to signal saturation at high gLAI levels (e.g. red edge and NIR, see Yao et al. (2017) for an example). This approach cannot be implemented relying on COTS imagery, as the widths of the bands are too wide.

The estimation of RUE was supported by the RS imagery via the calculation of fAPAR and fCover. fAPAR was derived extracting the reflectances from all plant tissue within the sampling plots. This approach relied on calibrated data in the RGB range; NIR information was not necessary.

fCover was determined based on the classification including all available bands

of all pixels inside the sampling plots. However, we assume that a classification including the visible range would have delivered the same results as the difference between plant tissue and soil reflectance is distinct. It can therefore be concluded that study III could have also been conducted relying on calibrated imagery delivered by a RGB camera only.
The analysis of our camera data preceded an elaborate processing of the data, which turned out to be very time-consuming. No information for these cameras on any modifications prevalent in the RAW images (i.e. lens distortion, vignetting effects) was available ahead of this study, such that we had to gather this ourselves. Additionally, we developed the processing chain to convert the cameras' DNs to reflectance values. In contrast, modern imaging spectral sensors assembled for UAV employment commonly include a preprocessing chain, which reduces the time spent on data preparation to a minimum. The trade-off between low procurement cost and time spent on data preparation for COTS imagery should therefore be carefully considered.

8.4 Benefits of UAV-derived Ultra-High Spatial Resolution Data

Data derived from airborne or satellite-based sensors commonly exhibits a much lower spatial resolution than UAV-based RS imagery. This implies a greater number of mixed pixels, which combine the signals of several land covers and possibly hinder an analysis in case only one class is in focus of interest. Additionally, the scale of field-measured variables might not match the scale of the RS data, and hereby obscures a plausible relationship between the two measurements. Contrary to those resolutions, a GSD of 1.5 cm offered by our COTS imagery captures the objects within the area of interest such that a distinction of classes might be possible. Additionally, field measurements can be accurately allocated to the corresponding RS data, possibly capturing variability much better.
We therefore assumed that our derived imagery allowed for the separation of different cover classes (plant tissue, illuminated soil and shaded soil) in our experimental plots, and hypothesized that the extraction of plant-only reflectance benefits the estimation of gLAI and RUE.
The cover classification was successfully included in studies II (chapter 6 from

page 55 onwards) and III (chapter 7 from page 77 onwards) as part of the methodology. In study II, it was used to investigate if the exclusion of non-plant pixels improved parametric and non-parametric models for remote gLAI estimation. In study III, it served both to extract reflectance values from plants only and to calculate the fractional cover in every sampling plot.

To our surprise, an exclusion did not result in improvement of the models (see chapter 6). Since the scale of the gLAI measurements (sampled on 0.75 m^2) exceeded those of the camera imagery, all reflectance values within the sampling area of each gLAI measurement were aggregated to one value. Taking the lack of model improvement and the size of the sampling area into account, an ultra-high spatial resolution (i.e. sub-plant level) as offered by our approach might not be necessary and could be replaced by resolutions aggregating information at plant to plot level.

Contrasting to this argument, neither the extraction of plant tissue reflectance only nor the calculation of fCover would have been possible at those resolutions, since the separation of cover classes was not possible.

In summary, it can be concluded that the utilisation of ultra-high spatial resolution imagery at sub-plant level does not necessarily benefit the estimation of gLAI in experimental plots; the estimation of RUE via fAPAR and fractional cover, however, is not possible at spatial resolutions where plot cover classes cannot be separated.

8.5 Outlook

This thesis looked at the potential of UAV-based COTS imagery for gLAI and RUE estimation in experimental plots. In this section, we would like to point out new challenges and perspectives for dedicated research in the fields of RS and agronomy, as well as for users outside these areas.

In chapters 5 and 6, we explored the capability to remotely estimate gLAI based on parametric and non-parametric regression. Section 3.2, as part of the state of research, additionally introduces physically-based and hybrid methods to estimate crop variables based on optical RS data. These methods are well-established in RS, typically relying on sensor data that is well-documented. Research could be devoted to whether it is possible to estimate gLAI with these methods using our RS system approach, where the spectral responses of the cameras are essentially a blackbox.

Additionally, science could explore if the 3D point cloud, that is created as a by-product for the ultimate generation of the orthomosaics (see subsection 4.3.3), contains additional information that might be beneficial for gLAI and RUE estimation (e.g. leaf inclination angle of individual plants for the estimation of the k-value or estimation of plant height).

Another approach worth investigating could include plant reflectances measured from different viewing angles. While the UAV moves along the designated flight path above the field, the attached cameras continuously take images. With a designated forward and sideward overlap of the images of 70% to 80%, every point in the field is captured from several different viewing angles. Oblique viewing angles might offer additional information on understorey leaves, as the canopy is not only viewed from nadir view. This information might also allow for a distinction of green and senesced leaf material both on top and further down the canopy.

The multiangular observations derived from the imagery could also be used to quantify angular effects of the plant canopy and its components. This supports the estimation of the bidirectional reflectance factor (BRF - defined as the ratio of the radiance reflected by a surface in a given direction to that which would be reflected into the same reflected-beam geometry by an ideal standard surface irradiated in exactly the same way as the target surface (Jones and Vaughan, 2010, page 199)), which could eventually, with several observations combined, be used to model angular variation of the plant canopy.

Our approach requires the accurate installation of ground control points around the field and the dedicated labour force of the pilot for the period of image acquisition. With ongoing improvements in real time kinematic (RTK)-based GPS positioning (i.e., up to centimetre-level accuracy) and autonomous employment of vehicles, it is imaginable that image acquisitions will occur automatically in the future, without user interference. The collection of reference points on the ground might become obsolete; so might the handling of the vehicle. The user could be presented with frequently acquired data ready to be analysed (*'smart remote sensing'*).

The findings presented in this thesis could be used by scientists working with crop models to improve prediction performance by considering cultivar-specific variables or the current status of the gLAI in the field. Furthermore, heterogeneity within the field could be reproduced, since crop models commonly simulate at plant level and do not account for varying conditions in crop stands. Several studies have been published on the coupling of RS data and crops models (e.g. Dong et al. (2017); Jin et al. (2018); Machwitz et al. (2014); Morel et al. (2014)). No study, however, relies on UAV-based COTS imagery.

Plant breeders cultivating different lines in extensive experiments could use the approaches to quickly sense differences in leaf area before flowering, simultaneously examining the genotype-environment-management interaction (as part of a high-throughput crop phenotyping scheme). A RUE mapping activity could involve the destructive sampling of a few plants only to measure biomass over points in time. Biomass could also be determined via UAV-based imagery; research in this coupling process is highly encouraged.

The documented approach, however, is not just restricted to field experiments; cultivated fields could be covered as well. Farmers might profit from the plant-level information as differences in plant growth become apparent, allowing for site-specific applications as part of precision farming rather than applications at field-level. This reduces the environmental impact and monetary cost of the employed means.

9 Bibliography

Aasen, H., Burkart, A., Bolten, A., Bareth, G., Oct. 2015. Generating 3d hyperspectral information with lightweight UAV snapshot cameras for vegetation monitoring: From camera calibration to quality assurance. ISPRS Journal of Photogrammetry and Remote Sensing 108, 245–259.
URL http://www.sciencedirect.com/science/article/pii/S0924271615001938

Akkaynak, D., Treibitz, T., Xiao, B., Gürkan, U. A., Allen, J. J., Demirci, U., Hanlon, R. T., Feb. 2014. Use of commercial off-the-shelf digital cameras for scientific data acquisition and scene-specific color calibration. Journal of the Optical Society of America A 31 (2), 312.
URL http://www.opticsinfobase.org/abstract.cfm?URI=josaa-31-2-312

Al-Abbas, A. H., Barr, R., Hall, J. D., Crane, F. L., Baumgardner, M. F., 1974. Spectra of Normal and Nutrient-Deficient Maize Leaves. Agronomy Journal 66 (1), 16–20.
URL https://dl.sciencesocieties.org/publications/aj/abstracts/66/1/AJ0660010016

Anderson, E. L., May 1988. Tillage and N fertilization effects on maize root growth and root:shoot ratio. Plant and Soil 108 (2), 245–251.
URL https://link.springer.com/article/10.1007/BF02375655

Andrade, F. H., Calviño, P., Cirilo, A., Barbieri, P., 2002. Yield Responses to Narrow Rows Depend on Increased Radiation Interception. Agronomy Journal 94 (5), 975.
URL https://www.agronomy.org/publications/aj/abstracts/94/5/975

Antonietta, M., Fanello, D. D., Acciaresi, H. A., Guiamet, J. J., Jan. 2014. Senescence and yield responses to plant density in stay green and earlier-

senescing maize hybrids from Argentina. Field Crops Research 155, 111–119.
URL http://www.sciencedirect.com/science/article/pii/S0378429013003225

Araus, J. L., Cairns, J. E., Jan. 2014. Field high-throughput phenotyping: the new crop breeding frontier. Trends in Plant Science 19 (1), 52–61.
URL http://www.sciencedirect.com/science/article/pii/S1360138513001994

Asrar, G., Fuchs, M., Kanemasu, E. T., Hatfield, J. L., 1984. Estimating Absorbed Photosynthetic Radiation and Leaf Area Index from Spectral Reflectance in Wheat. Agronomy Journal 76 (2), 300–306.
URL https://dl.sciencesocieties.org/publications/aj/abstracts/76/2/AJ0760020300

Baret, F., de Solan, B., Lopez-Lozano, R., Ma, K., Weiss, M., Oct. 2010. GAI estimates of row crops from downward looking digital photos taken perpendicular to rows at 57.5 zenith angle: Theoretical considerations based on 3d architecture models and application to wheat crops. Agricultural and Forest Meteorology 150 (11), 1393–1401.
URL http://www.sciencedirect.com/science/article/pii/S0168192310001206

Basukala, A. K., Oldenburg, C., Schellberg, J., Sultanov, M., Dubovyk, O., Jan. 2017. Towards improved land use mapping of irrigated croplands: performance assessment of different image classification algorithms and approaches. European Journal of Remote Sensing 50 (1), 187–201.
URL http://www.tandfonline.com/doi/abs/10.1080/22797254.2017.1308235

Bazi, Y., Alajlan, N., Melgani, F., AlHichri, H., Malek, S., Yager, R. R., Jun. 2014. Differential Evolution Extreme Learning Machine for the Classification of Hyperspectral Images. IEEE Geoscience and Remote Sensing Letters 11 (6), 1066–1070.
URL http://ieeexplore.ieee.org/document/6656874/

Belward, A. S., Skøien, J. O., May 2015. Who launched what, when and why; trends in global land-cover observation capacity from civilian earth

observation satellites. ISPRS Journal of Photogrammetry and Remote Sensing 103, 115–128.
URL http://linkinghub.elsevier.com/retrieve/pii/S0924271614000720

Bendig, J., Bolten, A., Bennertz, S., Broscheit, J., Eichfuss, S., Bareth, G., Oct. 2014. Estimating Biomass of Barley Using Crop Surface Models (CSMs) Derived from UAV-Based RGB Imaging. Remote Sensing 6 (11), 10395–10412.
URL http://www.mdpi.com/2072-4292/6/11/10395/

Bendig, J., Yu, K., Aasen, H., Bolten, A., Bennertz, S., Broscheit, J., Gnyp, M. L., Bareth, G., Jul. 2015. Combining UAV-based plant height from crop surface models, visible, and near infrared vegetation indices for biomass monitoring in barley. International Journal of Applied Earth Observation and Geoinformation 39, 79–87.
URL http://linkinghub.elsevier.com/retrieve/pii/S0303243415000446

Berni, J., Zarco-Tejada, P., Suarez, L., Fereres, E., Mar. 2009. Thermal and Narrowband Multispectral Remote Sensing for Vegetation Monitoring From an Unmanned Aerial Vehicle. IEEE Transactions on Geoscience and Remote Sensing 47 (3), 722–738.
URL http://ieeexplore.ieee.org/lpdocs/epic03/wrapper.htm?arnumber=4781575

Berra, E., Gibson-Poole, S., MacArthur, A., Gaulton, R., Hamilton, A., Aug. 2015. ESTIMATION OF THE SPECTRAL SENSITIVITY FUNCTIONS OF UN-MODIFIED AND MODIFIED COMMERCIAL OFF-THE-SHELF DIGITAL CAMERAS TO ENABLE THEIR USE AS A MULTISPECTRAL IMAGING SYSTEM FOR UAVS. ISPRS - International Archives of the Photogrammetry, Remote Sensing and Spatial Information Sciences XL-1/W4, 207–214.
URL http://www.int-arch-photogramm-remote-sens-spatial-inf-sci.net/XL-1-W4/207/2015/

Berra, E. F., Gaulton, R., Barr, S., 2017. Commercial Off-the-Shelf Digital Cameras on Unmanned Aerial Vehicles for Multitemporal Monitoring of Vegetation Reflectance and NDVI. IEEE Transactions on Geoscience and Remote Sensing,

1–9.
URL http://ieeexplore.ieee.org/document/7990537/

Birch, C., Vos, J., van der Putten, P., May 2003. Plant development and leaf area production in contrasting cultivars of maize grown in a cool temperate environment in the field. European Journal of Agronomy 19 (2), 173–188.
URL http://linkinghub.elsevier.com/retrieve/pii/S1161030102000345

Bréda, N. J. J., Jan. 2003. Ground-based measurements of leaf area index: a review of methods, instruments and current controversies. Journal of Experimental Botany 54 (392), 2403–2417.
URL http://jxb.oxfordjournals.org/content/54/392/2403

Breiman, L., Oct. 2001. Random Forests. Machine Learning 45 (1), 5–32.
URL https://link.springer.com/article/10.1023/A:1010933404324

Brüser, K., Feilhauer, H., Linstädter, A., Schellberg, J., Oomen, R. J., Ruppert, J. C., Ewert, F., 2014. Discrimination and characterization of management systems in semi-arid rangelands of South Africa using RapidEye time series. International Journal of Remote Sensing 35 (5), 1653–1673.
URL http://www.tandfonline.com/doi/abs/10.1080/01431161.2014.882028

Burkart, A., Aasen, H., Alonso, L., Menz, G., Bareth, G., Rascher, U., Jan. 2015. Angular Dependency of Hyperspectral Measurements over Wheat Characterized by a Novel UAV Based Goniometer. Remote Sensing 7 (1), 725–746.
URL http://www.mdpi.com/2072-4292/7/1/725

Burkart, A., Hecht, V. L., Kraska, T., Rascher, U., Feb. 2017. Phenological analysis of unmanned aerial vehicle based time series of barley imagery with high temporal resolution. Precision Agriculture, 1–13.
URL http://link.springer.com/article/10.1007/s11119-017-9504-y

Calvario, G., Sierra, B., Alarcón, T. E., Hernandez, C., Dalmau, O., Jun. 2017. A Multi-Disciplinary Approach to Remote Sensing through Low-Cost UAVs. Sensors 17 (6), 1411.
URL http://www.mdpi.com/1424-8220/17/6/1411

Campbell, J., Wynne, R., 2011. Introduction to Remote Sensing. Guilford Publications.
URL https://books.google.de/books?id=zgQDZEya6foC

Camps-Valls, G., Munoz-Mari, J., Gomez-Chova, L., Richter, K., Calpe-Maravilla, J., Apr. 2009. Biophysical Parameter Estimation With a Semisupervised Support Vector Machine. IEEE Geoscience and Remote Sensing Letters 6 (2), 248–252.

Castaldi, F., Pelosi, F., Pascucci, S., Casa, R., Aug. 2016. Assessing the potential of images from unmanned aerial vehicles (UAV) to support herbicide patch spraying in maize. Precision Agriculture, 1–19.
URL http://link.springer.com/article/10.1007/s11119-016-9468-3

Chu, T., Chen, R., Landivar, J. A., Maeda, M. M., Yang, C., Starek, M. J., Aug. 2016. Cotton growth modeling and assessment using unmanned aircraft system visual-band imagery. Journal of Applied Remote Sensing 10 (3), 036018.
URL http://remotesensing.spiedigitallibrary.org/article.aspx?doi=10.1117/1.JRS.10.036018

Claverie, M., Demarez, V., Duchemin, B., Hagolle, O., Ducrot, D., Marais-Sicre, C., Dejoux, J.-F., Huc, M., Keravec, P., Béziat, P., Fieuzal, R., Ceschia, E., Dedieu, G., Sep. 2012. Maize and sunflower biomass estimation in southwest France using high spatial and temporal resolution remote sensing data. Remote Sensing of Environment 124, 844–857.
URL http://www.sciencedirect.com/science/article/pii/S0034425712001678

Clewer, A., Scarisbrick, D., 2013. Practical Statistics and Experimental Design for Plant and Crop Science. Wiley.
URL https://books.google.de/books?id=ZUOIg6KnpfYC

Colomina, I., Molina, P., Jun. 2014. Unmanned aerial systems for photogrammetry and remote sensing: A review. ISPRS Journal of Photogrammetry and Remote Sensing 92, 79–97.
URL http://www.sciencedirect.com/science/article/pii/S0924271614000501

Córcoles, J. I., Ortega, J. F., Hernández, D., Moreno, M. A., May 2013. Estimation of leaf area index in onion (Allium cepa L.) using an unmanned aerial vehicle. Biosystems Engineering 115 (1), 31–42.
URL http://www.sciencedirect.com/science/article/pii/S1537511013000214

Cui, Z., Vitousek, P. M., Zhang, F., Chen, X., Feb. 2016. Strengthening Agronomy Research for Food Security and Environmental Quality. Environmental Science & Technology 50 (4), 1639–1641.
URL http://pubs.acs.org/doi/10.1021/acs.est.6b00267

Cummings, A., McKee, A., Kulkarni, K., Markandey, N., Apr. 2017. The Rise of UAVs. Photogrammetric Engineering & Remote Sensing 83 (4), 317–325.
URL http://www.ingentaconnect.com/content/10.14358/PERS.83.4.317

Darrodi, M. M., Finlayson, G., Goodman, T., Mackiewicz, M., Mar. 2015. Reference data set for camera spectral sensitivity estimation. Journal of the Optical Society of America A 32 (3), 381.
URL https://www.osapublishing.org/josaa/abstract.cfm?uri=josaa-32-3-381

Daughtry, C. S. T., Walthall, C. L., Kim, M. S., de Colstoun, E. B., McMurtrey III, J. E., Nov. 2000. Estimating Corn Leaf Chlorophyll Concentration from Leaf and Canopy Reflectance. Remote Sensing of Environment 74 (2), 229–239.
URL http://www.sciencedirect.com/science/article/pii/S0034425700001139

De Souza, C. H. W., Lamparelli, R. A. C., Rocha, J. V., Magalhães, P. S. G., Jan. 2017. Height estimation of sugarcane using an unmanned aerial system (UAS) based on structure from motion (SfM) point clouds. International Journal of Remote Sensing, 1–13.
URL https://www.tandfonline.com/doi/full/10.1080/01431161.2017.1285082

Demir, B., Erturk, S., Oct. 2007. Hyperspectral Image Classification Using Relevance Vector Machines. IEEE Geoscience and Remote Sensing Letters 4 (4), 586–590.
URL http://ieeexplore.ieee.org/document/4317528/

Deo, R. C., Samui, P., Kim, D., Aug. 2016. Estimation of monthly evaporative loss using relevance vector machine, extreme learning machine and multivariate adaptive regression spline models. Stochastic Environmental Research and Risk Assessment 30 (6), 1769–1784.
URL http://link.springer.com/10.1007/s00477-015-1153-y

Dong, T., Liu, J., Qian, B., Jing, Q., Croft, H., Chen, J., Wang, J., Huffman, T., Shang, J., Chen, P., Jan. 2017. Deriving Maximum Light Use Efficiency From Crop Growth Model and Satellite Data to Improve Crop Biomass Estimation. IEEE Journal of Selected Topics in Applied Earth Observations and Remote Sensing 10 (1), 104–117.
URL http://ieeexplore.ieee.org/document/7592477/

Elarab, M., Ticlavilca, A. M., Torres-Rua, A. F., Maslova, I., McKee, M., Dec. 2015. Estimating chlorophyll with thermal and broadband multispectral high resolution imagery from an unmanned aerial system using relevance vector machines for precision agriculture. International Journal of Applied Earth Observation and Geoinformation 43, 32–42.
URL http://www.sciencedirect.com/science/article/pii/S0303243415000719

Fedoroff, N. V., Battisti, D. S., Beachy, R. N., Cooper, P. J. M., Fischhoff, D. A., Hodges, C. N., Knauf, V. C., Lobell, D., Mazur, B. J., Molden, D., Reynolds, M. P., Ronald, P. C., Rosegrant, M. W., Sanchez, P. A., Vonshak, A., Zhu, J.-K., Feb. 2010. Radically Rethinking Agriculture for the 21st Century. Science 327 (5967), 833–834.
URL http://science.sciencemag.org/content/327/5967/833

Gabaldón-Leal, C., Webber, H., Otegui, M. E., Slafer, G. A., Ordóñez, R. A., Gaiser, T., Lorite, I. J., Ruiz-Ramos, M., Ewert, F., Nov. 2016. Modelling the impact of heat stress on maize yield formation. Field Crops Research 198 (Supplement C), 226–237.
URL http://www.sciencedirect.com/science/article/pii/S0378429016302684

Gago, J., Douthe, C., Coopman, R. E., Gallego, P. P., Ribas-Carbo, M., Flexas, J., Escalona, J., Medrano, H., May 2015. UAVs challenge to assess water stress for sustainable agriculture. Agricultural Water Management 153, 9–19.

URL http://www.sciencedirect.com/science/article/pii/S0378377415000293

Gaiser, T., Perkons, U., Küpper, P. M., Puschmann, D. U., Peth, S., Kautz, T., Pfeifer, J., Ewert, F., Horn, R., Köpke, U., Feb. 2012. Evidence of improved water uptake from subsoil by spring wheat following lucerne in a temperate humid climate. Field Crops Research 126, 56–62.
URL http://www.sciencedirect.com/science/article/pii/S0378429011003340

Gallo, K. P., Daughtry, C. S. T., 1986. Techniques for Measuring Intercepted and Absorbed Photosynthetically Active Radiation in Corn Canopies. Agronomy Journal 78 (4), 752–756.
URL https://dl.sciencesocieties.org/publications/aj/abstracts/78/4/AJ0780040752

Geipel, J., Link, J., Claupein, W., Oct. 2014. Combined Spectral and Spatial Modeling of Corn Yield Based on Aerial Images and Crop Surface Models Acquired with an Unmanned Aircraft System. Remote Sensing 6 (11), 10335–10355.
URL http://www.mdpi.com/2072-4292/6/11/10335

Ghamisi, P., Plaza, J., Chen, Y., Li, J., Plaza, A. J., Mar. 2017. Advanced Spectral Classifiers for Hyperspectral Images: A review. IEEE Geoscience and Remote Sensing Magazine 5 (1), 8–32.
URL http://ieeexplore.ieee.org/document/7882742/

Gitelson, A. A., Gamon, J. A., Jan. 2015. The need for a common basis for defining light-use efficiency: Implications for productivity estimation. Remote Sensing of Environment 156, 196–201.
URL http://linkinghub.elsevier.com/retrieve/pii/S0034425714003617

Gitelson, A. A., Peng, Y., Arkebauer, T. J., Suyker, A. E., Apr. 2015. Productivity, absorbed photosynthetically active radiation, and light use efficiency in crops: Implications for remote sensing of crop primary production. Journal of Plant Physiology 177, 100–109.
URL http://linkinghub.elsevier.com/retrieve/pii/S0176161715000073

Gitelson, A. A., Peng, Y., Huemmrich, K. F., May 2014. Relationship between fraction of radiation absorbed by photosynthesizing maize and soybean canopies and NDVI from remotely sensed data taken at close range and from MODIS 250 m resolution data. Remote Sensing of Environment 147, 108–120. URL http://www.sciencedirect.com/science/article/pii/S0034425714000698

Gitelson, A. A., Viña, A., Arkebauer, T. J., Rundquist, D. C., Keydan, G., Leavitt, B., Mar. 2003. Remote estimation of leaf area index and green leaf biomass in maize canopies. Geophysical Research Letters 30 (5), 1248. URL http://onlinelibrary.wiley.com/doi/10.1029/2002GL016450/abstract

Gnädinger, F., Schmidhalter, U., May 2017. Digital Counts of Maize Plants by Unmanned Aerial Vehicles (UAVs). Remote Sensing 9 (6), 544. URL http://www.mdpi.com/2072-4292/9/6/544

Gonzalez-Dugo, V., Zarco-Tejada, P., Nicolás, E., Nortes, P. A., Alarcón, J. J., Intrigliolo, D. S., Fereres, E., Dec. 2013. Using high resolution UAV thermal imagery to assess the variability in the water status of five fruit tree species within a commercial orchard. Precision Agriculture 14 (6), 660–678. URL https://link.springer.com/article/10.1007/s11119-013-9322-9

González-Jorge, H., Martínez-Sánchez, J., Bueno, M., Arias, a. P., Jul. 2017. Unmanned Aerial Systems for Civil Applications: A Review. Drones 1 (1), 2. URL http://www.mdpi.com/2504-446X/1/1/2

González-Sanpedro, M. C., Le Toan, T., Moreno, J., Kergoat, L., Rubio, E., Mar. 2008. Seasonal variations of leaf area index of agricultural fields retrieved from Landsat data. Remote Sensing of Environment 112 (3), 810–824. URL http://www.sciencedirect.com/science/article/pii/S003442570700274X

Gou, L., Xue, J., Qi, B., Ma, B., Zhang, W., 2017. Morphological Variation of Maize Cultivars in Response to Elevated Plant Densities. Agronomy Journal 109 (4), 1443. URL https://dl.sciencesocieties.org/publications/aj/abstracts/109/4/1443

Haghighattalab, A., Crain, J., Mondal, S., Rutkoski, J., Singh, R. P., Poland, J., 2017. Application of Geographically Weighted Regression to Improve Grain Yield Prediction from Unmanned Aerial System Imagery. Crop Science 0 (0), 0.
URL https://dl.sciencesocieties.org/publications/cs/abstracts/0/0/cropsci2016.12.1016

Hainmueller, J., Hazlett, C., Apr. 2014. Kernel Regularized Least Squares: Reducing Misspecification Bias with a Flexible and Interpretable Machine Learning Approach. Political Analysis 22 (2), 143–168.
URL https://academic.oup.com/pan/article/22/2/143/1546887/Kernel-Regularized-Least-Squares-Reducing

Hay, R., Porter, J., 2006. The Physiology of Crop Yield. Wiley.
URL https://books.google.de/books?id=0bZ8zSJl8HQC

Hijmans, R. J., 2016. raster: Geographic Data Analysis and Modeling.
URL https://CRAN.R-project.org/package=raster

Holman, F., Riche, A., Michalski, A., Castle, M., Wooster, M., Hawkesford, M., Dec. 2016. High Throughput Field Phenotyping of Wheat Plant Height and Growth Rate in Field Plot Trials Using UAV Based Remote Sensing. Remote Sensing 8 (12), 1031.
URL http://www.mdpi.com/2072-4292/8/12/1031

Homolová, L., Malenovský, Z., Clevers, J. G. P. W., García-Santos, G., Schaepman, M. E., Sep. 2013. Review of optical-based remote sensing for plant trait mapping. Ecological Complexity 15, 1–16.
URL http://www.sciencedirect.com/science/article/pii/S1476945X13000524

Houborg, R., McCabe, M. F., Jan. 2018. A hybrid training approach for leaf area index estimation via Cubist and random forests machine-learning. ISPRS Journal of Photogrammetry and Remote Sensing 135, 173–188.
URL https://www.sciencedirect.com/science/article/pii/S0924271617303209

Huang, G.-B., Zhu, Q.-Y., Siew, C.-K., Dec. 2006. Extreme learning machine: Theory and applications. Neurocomputing 70 (1–3), 489–501.

URL http://www.sciencedirect.com/science/article/pii/S0925231206000385

Huang, S., Gao, Y., Li, Y., Xu, L., Tao, H., Wang, P., Feb. 2017. Influence of plant architecture on maize physiology and yield in the Heilonggang River valley. The Crop Journal 5 (1), 52–62.
URL http://www.sciencedirect.com/science/article/pii/S2214514116300939

Hultquist, C., Chen, G., Zhao, K., Aug. 2014. A comparison of Gaussian process regression, random forests and support vector regression for burn severity assessment in diseased forests. Remote Sensing Letters 5 (8), 723–732.
URL http://dx.doi.org/10.1080/2150704X.2014.963733

Hunt, E. R., Hively, W. D., Fujikawa, S. J., Linden, D. S., Daughtry, C. S. T., McCarty, G. W., Jan. 2010. Acquisition of NIR-Green-Blue Digital Photographs from Unmanned Aircraft for Crop Monitoring. Remote Sensing 2 (1), 290–305.
URL http://www.mdpi.com/2072-4292/2/1/290

Jensen, J. R., 2007. Remote sensing of the environment: an earth resource perspective, 2nd Edition. Prentice Hall series in geographic information science. Pearson Prentice Hall, Upper Saddle River, NJ.
URL http://digitool.hbz-nrw.de:1801/webclient/DeliveryManager?pid=4396626&custom_att_2=simple_viewer

Jin, X., Kumar, L., Li, Z., Feng, H., Xu, X., Yang, G., Wang, J., Jan. 2018. A review of data assimilation of remote sensing and crop models. European Journal of Agronomy 92 (Supplement C), 141–152.
URL http://www.sciencedirect.com/science/article/pii/S1161030117301685

Jin, X., Liu, S., Baret, F., Hemerlé, M., Comar, A., Sep. 2017. Estimates of plant density of wheat crops at emergence from very low altitude UAV imagery. Remote Sensing of Environment 198, 105–114.
URL http://www.sciencedirect.com/science/article/pii/S0034425717302651

Jonckheere, I., Fleck, S., Nackaerts, K., Muys, B., Coppin, P., Weiss, M., Baret, F., Jan. 2004. Review of methods for in situ leaf area index determination:

Part I. Theories, sensors and hemispherical photography. Agricultural and Forest Meteorology 121 (1–2), 19–35.
URL http://www.sciencedirect.com/science/article/pii/S0168192303001643

Jones, H. G., Vaughan, R. A., Sep. 2010. Remote sensing of vegetation: principles, techniques, and applications. Oxford University Press.

Kautz, T., Stumm, C., Kösters, R., Köpke, U., Aug. 2010. Effects of perennial fodder crops on soil structure in agricultural headlands. Journal of Plant Nutrition and Soil Science 173 (4), 490–501.
URL http://doi.wiley.com/10.1002/jpln.200900216

Kelcey, J., Lucieer, A., May 2012. Sensor Correction of a 6-Band Multispectral Imaging Sensor for UAV Remote Sensing. Remote Sensing 4 (5), 1462–1493.
URL http://www.mdpi.com/2072-4292/4/5/1462

Khot, L. R., Sankaran, S., Carter, A. H., Johnson, D. A., Cummings, T. F., Jan. 2016. UAS imaging-based decision tools for arid winter wheat and irrigated potato production management. International Journal of Remote Sensing 37 (1), 125–137.
URL http://www.tandfonline.com/doi/full/10.1080/01431161.2015.1117685

Kira, O., Nguy-Robertson, A. L., Arkebauer, T. J., Linker, R., Gitelson, A. A., Mar. 2017. Toward Generic Models for Green LAI Estimation in Maize and Soybean: Satellite Observations. Remote Sensing 9 (4), 318.
URL http://www.mdpi.com/2072-4292/9/4/318

Kross, A., McNairn, H., Lapen, D., Sunohara, M., Champagne, C., Feb. 2015. Assessment of RapidEye vegetation indices for estimation of leaf area index and biomass in corn and soybean crops. International Journal of Applied Earth Observation and Geoinformation 34, 235–248.
URL http://www.sciencedirect.com/science/article/pii/S0303243414001664

Kuhn, M., 2016. A Short Introduction to the caret Package.
URL http://camoruco.ing.uc.edu.ve/cran/web/packages/caret/vignettes/caret.pdf

Kuhn, M., Johnson, K., 2013. Applied Predictive Modeling. SpringerLink : Bücher. Springer New York.
URL https://books.google.de/books?id=xYRDAAAAQBAJ

Kuhn, M., Wing, J., Weston, S., Williams, A., Keefer, C., Engelhardt, A., Cooper, T., Mayer, Z., Kenkel, B., Team, t. R. C., Benesty, M., Lescarbeau, R., Ziem, A., Scrucca, L., Tang, Y., Candan, C., Hunt, T., 2017. caret: Classification and Regression Training.
URL https://CRAN.R-project.org/package=caret

Laliberte, A. S., Goforth, M. A., Steele, C. M., Rango, A., Nov. 2011. Multispectral Remote Sensing from Unmanned Aircraft: Image Processing Workflows and Applications for Rangeland Environments. Remote Sensing 3 (11), 2529–2551.
URL http://www.mdpi.com/2072-4292/3/11/2529

le Maire, G., François, C., Dufrêne, E., Jan. 2004. Towards universal broad leaf chlorophyll indices using PROSPECT simulated database and hyperspectral reflectance measurements. Remote Sensing of Environment 89 (1), 1–28.
URL http://www.sciencedirect.com/science/article/pii/S0034425703002554

Lebourgeois, V., Bégué, A., Labbé, S., Mallavan, B., Prévot, L., Roux, B., Nov. 2008. Can Commercial Digital Cameras Be Used as Multispectral Sensors? A Crop Monitoring Test. Sensors 8 (11), 7300–7322.
URL http://www.mdpi.com/1424-8220/8/11/7300

Lelong, C. C. D., May 2008. Assessment of Unmanned Aerial Vehicles Imagery for Quantitative Monitoring of Wheat Crop in Small Plots. Sensors 8 (5), 3557–3585.
URL http://www.mdpi.org/sensors/list08.htm#s8053557

Leutner, B., Horning, N., 2017. RStoolbox: Tools for Remote Sensing Data Analysis.
URL https://CRAN.R-project.org/package=RStoolbox

Li, W., Niu, Z., Chen, H., Li, D., Wu, M., Zhao, W., Aug. 2016. Remote estimation of canopy height and aboveground biomass of maize using high-resolution stereo images from a low-cost unmanned aerial vehicle system. Ecological

Indicators 67, 637–648.
URL http://linkinghub.elsevier.com/retrieve/pii/S1470160X16301406

Liebisch, F., Kirchgessner, N., Schneider, D., Walter, A., Hund, A., Feb. 2015. Remote, aerial phenotyping of maize traits with a mobile multi-sensor approach. Plant Methods 11 (1), 9.
URL http://www.plantmethods.com/content/11/1/9/abstract

Lillesand, T. M., 2000. Remote Sensing and Image Interpretation. John Wiley & Sons.

Lima, A. R., Cannon, A. J., Hsieh, W. W., Nov. 2015. Nonlinear regression in environmental sciences using extreme learning machines: A comparative evaluation. Environmental Modelling & Software 73, 175–188.
URL http://linkinghub.elsevier.com/retrieve/pii/S1364815215300281

Lin, Y., Hyyppa, J., Jaakkola, A., May 2011. Mini-UAV-Borne LIDAR for Fine-Scale Mapping. IEEE Geoscience and Remote Sensing Letters 8 (3), 426–430.
URL http://ieeexplore.ieee.org/document/5624563/

Lindquist, J. L., Arkebauer, T. J., Walters, D. T., Cassman, K. G., Dobermann, A., 2005. Maize radiation use efficiency under optimal growth conditions. Agronomy Journal 97 (1), 72–78.
URL https://dl.sciencesocieties.org/publications/aj/abstracts/97/1/0072

Liu, G., Hou, P., Xie, R., Ming, B., Wang, K., Xu, W., Liu, W., Yang, Y., Li, S., Nov. 2017. Canopy characteristics of high-yield maize with yield potential of 22.5mgha1. Field Crops Research 213 (Supplement C), 221–230.
URL http://www.sciencedirect.com/science/article/pii/S0378429017307451

Lobell, D. B., Asner, G. P., 2002. Moisture effects on soil reflectance. Soil Science Society of America Journal 66 (3), 722–727.

Lu, B., He, Y., Jun. 2017. Species classification using Unmanned Aerial Vehicle (UAV)-acquired high spatial resolution imagery in a heterogeneous grassland.

ISPRS Journal of Photogrammetry and Remote Sensing 128, 73–85.
URL http://www.sciencedirect.com/science/article/pii/S0924271616305688

Luche, H. d. S., Silva, J. A. G. d., Maia, L. C. d., Oliveira, A. C. d., Oct. 2015. Stay-green: a potentiality in plant breeding. Ciência Rural 45 (10), 1755–1760.
URL http://www.scielo.br/scielo.php?script=sci_arttext&pid=S0103-84782015001001755&lng=en&tlng=en

Ma, D. L., Xie, R. Z., Niu, X. K., Li, S. K., Long, H. L., Liu, Y. E., Aug. 2014. Changes in the morphological traits of maize genotypes in China between the 1950s and 2000s. European Journal of Agronomy 58 (Supplement C), 1–10.
URL http://www.sciencedirect.com/science/article/pii/S1161030114000422

Maat, H., Feb. 2011. The history and future of agricultural experiments. NJAS - Wageningen Journal of Life Sciences 57 (3), 187–195.
URL http://www.sciencedirect.com/science/article/pii/S1573521410000461

Machwitz, M., Giustarini, L., Bossung, C., Frantz, D., Schlerf, M., Lilienthal, H., Wandera, L., Matgen, P., Hoffmann, L., Udelhoven, T., Dec. 2014. Enhanced biomass prediction by assimilating satellite data into a crop growth model. Environmental Modelling & Software 62, 437–453.
URL http://www.sciencedirect.com/science/article/pii/S1364815214002345

Maddonni, G. A., Otegui, M. E., Cirilo, A. G., Jul. 2001. Plant population density, row spacing and hybrid effects on maize canopy architecture and light attenuation. Field Crops Research 71 (3), 183–193.
URL http://www.sciencedirect.com/science/article/pii/S0378429001001587

Maresma, n., Ariza, M., Martínez, E., Lloveras, J., Martínez-Casasnovas, J. A., Nov. 2016. Analysis of Vegetation Indices to Determine Nitrogen Application and Yield Prediction in Maize (Zea mays L.) from a Standard UAV Service. Remote Sensing 8 (12), 973.
URL http://www.mdpi.com/2072-4292/8/12/973

Mesas-Carrascosa, F.-J., Torres-Sánchez, J., Clavero-Rumbao, I., García-Ferrer, A., Peña, J.-M., Borra-Serrano, I., López-Granados, F., Sep. 2015. Assessing Optimal Flight Parameters for Generating Accurate Multispectral Orthomosaicks by UAV to Support Site-Specific Crop Management. Remote Sensing 7 (10), 12793–12814.
URL http://www.mdpi.com/2072-4292/7/10/12793

Mitchell, P., Sheehy, J., Woodward, F., 1998. Potential yields and the efficiency of radiation use in rice. Vol. 32 of IRRI Discussion Paper Series. Manila.

Monteith, J. L., Nov. 1977. The management of inputs for yet greater agricultural yield and efficiency - Climate and the efficiency of crop production in Britain. Phil. Trans. R. Soc. Lond. B 281 (980), 277–294.
URL http://rstb.royalsocietypublishing.org/content/281/980/277

Morel, J., Bégué, A., Todoroff, P., Martiné, J.-F., Lebourgeois, V., Petit, M., Nov. 2014. Coupling a sugarcane crop model with the remotely sensed time series of fIPAR to optimise the yield estimation. European Journal of Agronomy 61, 60–68.
URL http://linkinghub.elsevier.com/retrieve/pii/S1161030114000963

Moreno, R., Corona, F., Lendasse, A., Graña, M., Galvão, L. S., Mar. 2014. Extreme learning machines for soybean classification in remote sensing hyperspectral images. Neurocomputing 128, 207–216.
URL http://linkinghub.elsevier.com/retrieve/pii/S0925231213010102

Mountrakis, G., Im, J., Ogole, C., May 2011. Support vector machines in remote sensing: A review. ISPRS Journal of Photogrammetry and Remote Sensing 66 (3), 247–259.
URL http://www.sciencedirect.com/science/article/pii/S0924271610001140

Mutanga, O., Adam, E., Cho, M. A., Aug. 2012. High density biomass estimation for wetland vegetation using WorldView-2 imagery and random forest regression algorithm. International Journal of Applied Earth Observation and Geoinformation 18, 399–406.

URL http://www.sciencedirect.com/science/article/pii/S0303243412000566

Nguy-Robertson, A., Gitelson, A., Peng, Y., Viña, A., Arkebauer, T., Rundquist, D., 2012. Green Leaf Area Index Estimation in Maize and Soybean: Combining Vegetation Indices to Achieve Maximal Sensitivity. Agronomy Journal 104 (5), 1336.
URL https://www.agronomy.org/publications/aj/abstracts/104/5/1336

Nijland, W., de Jong, R., de Jong, S. M., Wulder, M. A., Bater, C. W., Coops, N. C., Jan. 2014. Monitoring plant condition and phenology using infrared sensitive consumer grade digital cameras. Agricultural and Forest Meteorology 184, 98–106.
URL http://www.sciencedirect.com/science/article/pii/S0168192313002621

Pajares, G., Apr. 2015. Overview and Current Status of Remote Sensing Applications Based on Unmanned Aerial Vehicles (UAVs). Photogrammetric Engineering & Remote Sensing 81 (4), 281–330.
URL http://openurl.ingenta.com/content/xref?genre=article&issn=0099-1112&volume=81&issue=4&spage=281

Pal, M., Jul. 2009. Extreme-learning-machine-based land cover classification. International Journal of Remote Sensing 30 (14), 3835–3841.
URL http://dx.doi.org/10.1080/01431160902788636

Parplies, A., Dubovyk, O., Tewes, A., Mund, J.-P., Schellberg, J., Dec. 2016. Phenomapping of rangelands in South Africa using time series of RapidEye data. International Journal of Applied Earth Observation and Geoinformation 53, 90–102.
URL http://www.sciencedirect.com/science/article/pii/S0303243416301313

Pasolli, L., Melgani, F., Blanzieri, E., Jul. 2010. Gaussian Process Regression for Estimating Chlorophyll Concentration in Subsurface Waters From Remote Sensing Data. IEEE Geoscience and Remote Sensing Letters 7 (3), 464–468.
URL http://ieeexplore.ieee.org/document/5411816/

R Core Team, 2017. R: A Language and Environment for Statistical Computing. R Foundation for Statistical Computing, Vienna, Austria.
URL https://www.R-project.org/

Rabatel, G., Gorretta, N., Labbé, S., Jan. 2014. Getting simultaneous red and near-infrared band data from a single digital camera for plant monitoring applications: Theoretical and practical study. Biosystems Engineering 117, 2–14.
URL http://www.sciencedirect.com/science/article/pii/S1537511013000962

Rabatel, G., Labbé, S., Jan. 2016. Registration of visible and near infrared unmanned aerial vehicle images based on Fourier-Mellin transform. Precision Agriculture.
URL http://link.springer.com/10.1007/s11119-016-9437-x

Ranum, P., Peña-Rosas, J. P., Garcia-Casal, M. N., Apr. 2014. Global maize production, utilization, and consumption. Annals of the New York Academy of Sciences 1312 (1), 105–112.
URL http://onlinelibrary.wiley.com/doi/10.1111/nyas.12396/abstract

Rasmussen, C. E., 2006. Gaussian processes for machine learning. MIT Press.

Rasmussen, J., Ntakos, G., Nielsen, J., Svensgaard, J., Poulsen, R. N., Christensen, S., Mar. 2016. Are vegetation indices derived from consumer-grade cameras mounted on UAVs sufficiently reliable for assessing experimental plots? European Journal of Agronomy 74, 75–92.
URL http://linkinghub.elsevier.com/retrieve/pii/S1161030115300733

Rasouli, K., Hsieh, W. W., Cannon, A. J., Jan. 2012. Daily streamflow forecasting by machine learning methods with weather and climate inputs. Journal of Hydrology 414, 284–293.
URL http://www.sciencedirect.com/science/article/pii/S0022169411007633

Ren, B., Liu, W., Zhang, J., Dong, S., Liu, P., Zhao, B., Apr. 2017a. Effects of plant density on the photosynthetic and chloroplast characteristics of maize

under high-yielding conditions. The Science of Nature 104 (3-4), 12.
URL https://link.springer.com/article/10.1007/s00114-017-1445-9

Ren, D. D. W., Tripathi, S., Li, L. K. B., Jan. 2017b. Low-cost multispectral imaging for remote sensing of lettuce health. Journal of Applied Remote Sensing 11 (1), 016006.
URL http://remotesensing.spiedigitallibrary.org/article.aspx?doi=10.1117/1.JRS.11.016006

Rivera, J. P., Verrelst, J., Delegido, J., Veroustraete, F., Moreno, J., May 2014. On the Semi-Automatic Retrieval of Biophysical Parameters Based on Spectral Index Optimization. Remote Sensing 6 (6), 4927–4951.
URL http://www.mdpi.com/2072-4292/6/6/4927

Rodriguez-Galiano, V. F., Ghimire, B., Rogan, J., Chica-Olmo, M., Rigol-Sanchez, J. P., Jan. 2012. An assessment of the effectiveness of a random forest classifier for land-cover classification. ISPRS Journal of Photogrammetry and Remote Sensing 67, 93–104.
URL http://www.sciencedirect.com/science/article/pii/S0924271611001304

Ross, J., Sulev, M., Feb. 2000. Sources of errors in measurements of PAR. Agricultural and Forest Meteorology 100 (2), 103–125.
URL http://www.sciencedirect.com/science/article/pii/S0168192399001446

Salamí, E., Barrado, C., Pastor, E., Nov. 2014. UAV Flight Experiments Applied to the Remote Sensing of Vegetated Areas. Remote Sensing 6 (11), 11051–11081.
URL http://www.mdpi.com/2072-4292/6/11/11051/

Sankaran, S., Khot, L. R., Espinoza, C. Z., Jarolmasjed, S., Sathuvalli, V. R., Vandemark, G. J., Miklas, P. N., Carter, A. H., Pumphrey, M. O., Knowles, N. R., Pavek, M. J., Oct. 2015. Low-altitude, high-resolution aerial imaging systems for row and field crop phenotyping: A review. European Journal of Agronomy 70, 112–123.
URL http://www.sciencedirect.com/science/article/pii/S1161030115300095

Schirrmann, M., Giebel, A., Gleiniger, F., Pflanz, M., Lentschke, J., Dammer, K.-H., Aug. 2016. Monitoring Agronomic Parameters of Winter Wheat Crops with Low-Cost UAV Imagery. Remote Sensing 8 (9), 706.
URL http://www.mdpi.com/2072-4292/8/9/706

Schirrmann, M., Hamdorf, A., Giebel, A., Gleiniger, F., Pflanz, M., Dammer, K.-H., Jun. 2017. Regression Kriging for Improving Crop Height Models Fusing Ultra-Sonic Sensing with UAV Imagery. Remote Sensing 9 (7), 665.
URL http://www.mdpi.com/2072-4292/9/7/665

Shamshirband, S., Mohammadi, K., Tong, C. W., Petković, D., Porcu, E., Mostafaeipour, A., Ch, S., Sedaghat, A., Mar. 2016. Application of extreme learning machine for estimation of wind speed distribution. Climate Dynamics 46 (5-6), 1893–1907.
URL http://link.springer.com/10.1007/s00382-015-2682-2

Shiferaw, B., Prasanna, B. M., Hellin, J., Bänziger, M., Sep. 2011. Crops that feed the world 6. Past successes and future challenges to the role played by maize in global food security. Food Security 3 (3), 307–327.
URL http://link.springer.com/10.1007/s12571-011-0140-5

Sinclair, T. R., Muchow, R. C., Jan. 1999. Radiation Use Efficiency. Advances in Agronomy 65, 215–265.
URL http://www.sciencedirect.com/science/article/pii/S0065211308609141

Singer, J. W., Meek, D. W., Sauer, T. J., Prueger, J. H., Hatfield, J. L., Feb. 2011. Variability of light interception and radiation use efficiency in maize and soybean. Field Crops Research 121 (1), 147–152.
URL http://linkinghub.elsevier.com/retrieve/pii/S0378429010003217

Smith, G. M., Milton, E. J., Jan. 1999. The use of the empirical line method to calibrate remotely sensed data to reflectance. International Journal of Remote Sensing 20 (13), 2653–2662.
URL http://dx.doi.org/10.1080/014311699211994

Smola, A. J., Schölkopf, B., Aug. 2004. A tutorial on support vector regression. Statistics and Computing 14 (3), 199–222.

URL https://link.springer.com/article/10.1023/B:STCO.0000035301.49549.88

Stöckle, C. O., Kemanian, A. R., 2009. Chapter 7 - Crop Radiation Capture and Use Efficiency: A Framework for Crop Growth Analysis. In: Crop Physiology. Academic Press, San Diego, pp. 145–170, dOI: 10.1016/B978-0-12-374431-9.00007-4.
URL http://www.sciencedirect.com/science/article/pii/B9780123744319000074

Swanckaert, J., Pannecoucque, J., Waes, J. V., Steppe, K., Labeke, M.-C. V., Reheul, D., Jul. 2017. Stay-green characterization in Belgian forage maize. The Journal of Agricultural Science 155 (5), 766–776.
URL https://www.cambridge.org/core/journals/journal-of-agricultural-science/article/staygreen-characterization-in-belgian-forage-maize/9CD73D8672AFF4B68BFDFB9CD495CA78

Tian, Y.-C., Gu, K.-J., Chu, X., Yao, X., Cao, W.-X., Zhu, Y., Mar. 2014. Comparison of different hyperspectral vegetation indices for canopy leaf nitrogen concentration estimation in rice. Plant and Soil 376 (1-2), 193–209.
URL http://link.springer.com/10.1007/s11104-013-1937-0

Timlin, D. J., Fleisher, D. H., Kemanian, A. R., Reddy, V. R., 2014. Plant Density and Leaf Area Index Effects on the Distribution of Light Transmittance to the Soil Surface in Maize. Agronomy Journal 106 (5), 1828.
URL https://dl.sciencesocieties.org/publications/aj/abstracts/106/5/1828

Tipping, M. E., 2001. Sparse Bayesian Learning and the Relevance Vector Machine. Journal of Machine Learning Research 1 (Jun), 211–244.
URL http://www.jmlr.org/papers/v1/tipping01a.html

Tollenaar, M., Aguilera, A., 1992. Radiation use efficiency of an old and a new maize hybrid. Agronomy journal 84 (3), 536–541.

Tollenaar, M., Wu, J., 1999. Yield improvement in temperate maize is attributable to greater stress tolerance. Crop Science 39 (6), 1597–1604.

URL https://dl.sciencesocieties.org/publications/cs/abstracts/39/6/1597

Torres-Sánchez, J., Peña, J. M., de Castro, A. I., López-Granados, F., Apr. 2014. Multi-temporal mapping of the vegetation fraction in early-season wheat fields using images from UAV. Computers and Electronics in Agriculture 103, 104–113.
URL http://www.sciencedirect.com/science/article/pii/S0168169914000568

Toth, C., Jóźków, G., May 2016. Remote sensing platforms and sensors: A survey. ISPRS Journal of Photogrammetry and Remote Sensing 115, 22–36.
URL http://www.sciencedirect.com/science/article/pii/S0924271615002270

Vapnik, V., 1998. Statistical learning theory. Wiley, New York.

Vega, F. A., Ramírez, F. C., Saiz, M. P., Rosúa, F. O., Apr. 2015. Multi-temporal imaging using an unmanned aerial vehicle for monitoring a sunflower crop. Biosystems Engineering 132, 19–27.
URL http://www.sciencedirect.com/science/article/pii/S1537511015000185

Verger, A., Vigneau, N., Chéron, C., Gilliot, J.-M., Comar, A., Baret, F., Sep. 2014. Green area index from an unmanned aerial system over wheat and rapeseed crops. Remote Sensing of Environment 152, 654–664.
URL http://www.sciencedirect.com/science/article/pii/S0034425714002193

Verhoeven, G., Smet, P., Poelman, D., Vermeulen, F., Oct. 2009. Spectral Characterization of a Digital Still Camera's NIR Modification to Enhance Archaeological Observation. IEEE Transactions on Geoscience and Remote Sensing 47 (10), 3456–3468.
URL http://ieeexplore.ieee.org/lpdocs/epic03/wrapper.htm?arnumber=5196727

Verhoeven, G. J. J., Apr. 2010. It's all about the format – unleashing the power of RAW aerial photography. International Journal of Remote Sensing 31 (8),

2009–2042.
URL http://dx.doi.org/10.1080/01431160902929271

Verrelst, J., Camps-Valls, G., Muñoz-Marí, J., Rivera, J. P., Veroustraete, F., Clevers, J. G. P. W., Moreno, J., Oct. 2015a. Optical remote sensing and the retrieval of terrestrial vegetation bio-geophysical properties – A review. ISPRS Journal of Photogrammetry and Remote Sensing 108, 273–290.
URL http://www.sciencedirect.com/science/article/pii/S0924271615001422

Verrelst, J., Muñoz, J., Alonso, L., Delegido, J., Rivera, J. P., Camps-Valls, G., Moreno, J., Mar. 2012a. Machine learning regression algorithms for biophysical parameter retrieval: Opportunities for Sentinel-2 and -3. Remote Sensing of Environment 118, 127–139.
URL http://www.sciencedirect.com/science/article/pii/S003442571100397X

Verrelst, J., Rivera, J. P., Gitelson, A., Delegido, J., Moreno, J., Camps-Valls, G., Oct. 2016. Spectral band selection for vegetation properties retrieval using Gaussian processes regression. International Journal of Applied Earth Observation and Geoinformation 52, 554–567.
URL http://www.sciencedirect.com/science/article/pii/S0303243416301234

Verrelst, J., Rivera, J. P., Moreno, J., Camps-Valls, G., Dec. 2013. Gaussian processes uncertainty estimates in experimental Sentinel-2 LAI and leaf chlorophyll content retrieval. ISPRS Journal of Photogrammetry and Remote Sensing 86, 157–167.
URL http://www.sciencedirect.com/science/article/pii/S092427161300213X

Verrelst, J., Rivera, J. P., Veroustraete, F., Muñoz-Marí, J., Clevers, J. G. P. W., Camps-Valls, G., Moreno, J., Oct. 2015b. Experimental Sentinel-2 LAI estimation using parametric, non-parametric and physical retrieval methods – A comparison. ISPRS Journal of Photogrammetry and Remote Sensing 108, 260–272.
URL http://www.sciencedirect.com/science/article/pii/S0924271615001239

Verrelst, J., Romijn, E., Kooistra, L., Sep. 2012b. Mapping Vegetation Density in a Heterogeneous River Floodplain Ecosystem Using Pointable CHRIS/PROBA Data. Remote Sensing 4 (9), 2866–2889.
URL http://www.mdpi.com/2072-4292/4/9/2866

Viña, A., Gitelson, A. A., Sep. 2005. New developments in the remote estimation of the fraction of absorbed photosynthetically active radiation in crops. Geophysical Research Letters 32 (17).
URL http://doi.wiley.com/10.1029/2005GL023647

Viña, A., Gitelson, A. A., Nguy-Robertson, A. L., Peng, Y., Dec. 2011. Comparison of different vegetation indices for the remote assessment of green leaf area index of crops. Remote Sensing of Environment 115 (12), 3468–3478.
URL http://www.sciencedirect.com/science/article/pii/S0034425711002926

von Bueren, S. K., Burkart, A., Hueni, A., Rascher, U., Tuohy, M. P., Yule, I. J., Jan. 2015. Deploying four optical UAV-based sensors over grassland: challenges and limitations. Biogeosciences 12 (1), 163–175.
URL http://www.biogeosciences.net/12/163/2015/

Vos, J., Putten, P. E. L. v. d., Birch, C. J., Jul. 2005. Effect of nitrogen supply on leaf appearance, leaf growth, leaf nitrogen economy and photosynthetic capacity in maize (Zea mays L.). Field Crops Research 93 (1), 64–73.
URL http://www.sciencedirect.com/science/article/pii/S0378429004002400

Walburg, G., Bauer, M. E., Daughtry, C. S. T., Housley, T. L., 1982. Effects of Nitrogen Nutrition on the Growth, Yield, and Reflectance Characteristics of Corn Canopies. Agronomy Journal 74 (4), 677–683.
URL https://dl.sciencesocieties.org/publications/aj/abstracts/74/4/AJ0740040677

Wallace, L., Lucieer, A., Watson, C., Turner, D., May 2012. Development of a UAV-LiDAR System with Application to Forest Inventory. Remote Sensing 4 (6), 1519–1543.
URL http://www.mdpi.com/2072-4292/4/6/1519

Wang, F.-m., Huang, J.-f., Lou, Z.-h., Jun. 2011. A comparison of three methods for estimating leaf area index of paddy rice from optimal hyperspectral bands. Precision Agriculture 12 (3), 439–447.
URL https://link.springer.com/article/10.1007/s11119-010-9185-2

Wang, W., Yao, X., Yao, X., Tian, Y., Liu, X., Ni, J., Cao, W., Zhu, Y., Apr. 2012. Estimating leaf nitrogen concentration with three-band vegetation indices in rice and wheat. Field Crops Research 129, 90–98.
URL http://www.sciencedirect.com/science/article/pii/S0378429012000299

Wilhelm, W. W., Ruwe, K., Schlemmer, M. R., 2000. Comparison of three leaf area index meters in a corn canopy. Crop Science 40 (4), 1179–1183.
URL https://dl.sciencesocieties.org/publications/cs/abstracts/40/4/1179

Yan, P., Pan, J., Zhang, W., Shi, J., Chen, X., Cui, Z., Feb. 2017. A high plant density reduces the ability of maize to use soil nitrogen. PLOS ONE 12 (2), e0172717.
URL http://journals.plos.org/plosone/article?id=10.1371/journal.pone.0172717

Yang, C., Westbrook, J. K., Suh, C. P.-C., Martin, D. E., Hoffmann, W. C., Lan, Y., Fritz, B. K., Goolsby, J. A., Jun. 2014. An Airborne Multispectral Imaging System Based on Two Consumer-Grade Cameras for Agricultural. Remote Sensing 6 (6), 5257–5278.
URL http://www.mdpi.com/2072-4292/6/6/5257

Yang, G., Liu, J., Zhao, C., Li, Z., Huang, Y., Yu, H., Xu, B., Yang, X., Zhu, D., Zhang, X., Zhang, R., Feng, H., Zhao, X., Li, Z., Li, H., Yang, H., 2017. Unmanned aerial vehicle remote sensing for field-based crop phenotyping: Current status and perspectives. Frontiers in Plant Science 8.
URL http://journal.frontiersin.org/article/10.3389/fpls.2017.01111/full

Yao, X., Wang, N., Liu, Y., Cheng, T., Tian, Y., Chen, Q., Zhu, Y., Dec. 2017. Estimation of Wheat LAI at Middle to High Levels Using Unmanned Aerial Vehicle Narrowband Multispectral Imagery. Remote Sensing 9 (12), 1304.
URL http://www.mdpi.com/2072-4292/9/12/1304

Yuan, H., Yang, G., Li, C., Wang, Y., Liu, J., Yu, H., Feng, H., Xu, B., Zhao, X., Yang, X., Mar. 2017. Retrieving Soybean Leaf Area Index from Unmanned Aerial Vehicle Hyperspectral Remote Sensing: Analysis of RF, ANN, and SVM Regression Models. Remote Sensing 9 (4), 309.
URL http://www.mdpi.com/2072-4292/9/4/309

Yue, J., Yang, G., Li, C., Li, Z., Wang, Y., Feng, H., Xu, B., Jul. 2017. Estimation of Winter Wheat Above-Ground Biomass Using Unmanned Aerial Vehicle-Based Snapshot Hyperspectral Sensor and Crop Height Improved Models. Remote Sensing 9 (7), 708.
URL http://www.mdpi.com/2072-4292/9/7/708

Zaman, B., Jensen, A., Clemens, S. R., McKee, M., Dec. 2014. Retrieval of Spectral Reflectance of High Resolution Multispectral Imagery Acquired with an Autonomous Unmanned Aerial Vehicle. Photogrammetric Engineering & Remote Sensing 80 (12), 1139–1150.
URL http://www.ingentaconnect.com/content/10.14358/PERS.80.12.1139

Zaman-Allah, M., Vergara, O., Araus, J. L., Tarekegne, A., Magorokosho, C., Zarco-Tejada, P. J., Hornero, A., Albà, A. H., Das, B., Craufurd, P., Olsen, M., Prasanna, B. M., Cairns, J., Jun. 2015. Unmanned aerial platform-based multi-spectral imaging for field phenotyping of maize. Plant Methods 11 (1), 35.
URL http://www.plantmethods.com/content/11/1/35/abstract

Zhang, C., Kovacs, J. M., Dec. 2012. The application of small unmanned aerial systems for precision agriculture: a review. Precision Agriculture 13 (6), 693–712.
URL https://link.springer.com/article/10.1007/s11119-012-9274-5

Zhang, J., Yang, C., Song, H., Hoffmann, W. C., Zhang, D., Zhang, G., Mar. 2016. Evaluation of an Airborne Remote Sensing Platform Consisting of Two Consumer-Grade Cameras for Crop Identification. Remote Sensing 8 (3), 257.
URL http://www.mdpi.com/2072-4292/8/3/257

Zheng, G., Moskal, L. M., Apr. 2009. Retrieving Leaf Area Index (LAI) Using Remote Sensing: Theories, Methods and Sensors. Sensors 9 (4), 2719–2745.
URL http://www.mdpi.com/1424-8220/9/4/2719

Zhou, J., Pavek, M. J., Shelton, S. C., Holden, Z. J., Sankaran, S., Sep. 2016. Aerial multispectral imaging for crop hail damage assessment in potato. Computers and Electronics in Agriculture 127, 406–412.
URL http://linkinghub.elsevier.com/retrieve/pii/S0168169916304124

Zhou, X., Zheng, H. B., Xu, X. Q., He, J. Y., Ge, X. K., Yao, X., Cheng, T., Zhu, Y., Cao, W. X., Tian, Y. C., Aug. 2017. Predicting grain yield in rice using multi-temporal vegetation indices from UAV-based multispectral and digital imagery. ISPRS Journal of Photogrammetry and Remote Sensing 130, 246–255.
URL http://www.sciencedirect.com/science/article/pii/S0924271616302337

Appendix

Table A: gLAI analysis results

Year	Date	Temperature Sum	Trial	Min	Mean	Max	SD	CV
2015	18.06.2015	279.6	S1N1	0.12	0.21	0.31	0.06	26.95
			S1N2	0.27	0.45	0.53	0.08	17.68
			S2N1	0.37	0.49	0.65	0.09	19.47
			S2N2	0.52	0.80	1.02	0.18	22.01
	30.06.2015	371.8	S1N1	0.38	0.70	1.01	0.18	25.27
			S1N2	1.14	1.57	1.99	0.22	13.79
			S2N1	1.11	1.65	2.78	0.38	23.15
			S2N2	1.75	2.38	3.33	0.46	19.17
	16.07.2015	564.7	S1N1	1.45	2.07	2.82	0.34	16.31
			S1N2	1.87	3.22	4.49	0.66	20.60
			S2N1	2.97	3.61	4.17	0.35	9.68
			S2N2	3.38	4.18	4.92	0.50	11.95
	03.08.2015	750.5	S1N1	1.59	2.01	2.29	0.24	12.19
			S1N2	2.72	3.18	3.78	0.46	14.60
			S2N1	3.40	3.65	4.08	0.28	7.75
			S2N2	3.39	4.17	5.00	0.63	15.12
	20.08.2015	931.1	S1N1	1.33	2.08	2.54	0.35	16.71
			S1N2	1.99	2.88	3.94	0.59	20.67
			S2N1	2.71	3.62	4.24	0.55	15.26
			S2N2	3.52	4.23	5.19	0.59	13.85
	11.09.2015	1110.4	S1N1	1.87	2.08	2.31	0.15	7.31
			S1N2	2.33	3.17	4.16	0.58	18.26
			S2N1	2.69	3.88	4.30	0.49	12.71
			S2N2	2.34	3.69	4.23	0.64	17.46
	30.09.2015	1202.9	S1N1	1.29	1.95	2.59	0.43	22.15
			S1N2	1.57	2.46	3.32	0.57	23.03
			S2N1	1.83	3.22	4.18	0.67	20.96
			S2N2	2.35	3.14	3.97	0.59	18.86
	12.10.2015	1244.1	S1N1	1.08	1.41	1.79	0.24	16.73
			S1N2	1.20	1.73	2.09	0.27	15.89
			S2N1	1.77	2.36	2.76	0.35	14.92

Continued on next page

Table A – continued from previous page

Year	Date	Temperature Sum	Trial	Min	Mean	Max	SD	CV
			S2N2	1.88	2.34	2.88	0.37	15.68
2016	15.06.2016	312.7	S1N1	0.06	0.16	0.28	0.07	42.35
			S1N2	0.12	0.19	0.28	0.06	30.98
			S2N1	0.23	0.28	0.36	0.05	16.62
			S2N2	0.18	0.35	0.56	0.11	30.60
	27.06.2016	411.1	S1N1	0.15	0.43	0.74	0.20	47.15
			S1N2	0.37	0.68	1.05	0.23	33.70
			S2N1	0.58	0.85	1.24	0.23	26.95
			S2N2	0.86	1.25	1.72	0.29	23.25
	08.07.2016	515.4	S1N1	0.72	1.26	1.75	0.38	30.07
			S1N2	1.55	1.88	2.23	0.23	12.25
			S2N1	0.99	2.19	2.83	0.59	26.78
			S2N2	2.38	3.04	3.94	0.50	16.59
	19.07.2016	635.4	S1N1	1.49	2.17	3.06	0.57	26.21
			S1N2	1.37	2.05	2.52	0.42	20.50
			S2N1	2.18	3.22	4.00	0.65	20.08
			S2N2	3.37	4.15	4.81	0.62	14.93
	05.08.2016	828.9	S1N1	1.60	2.40	3.85	0.70	29.37
			S1N2	1.56	2.36	3.51	0.60	25.58
			S2N1	1.57	3.86	5.53	1.15	29.86
			S2N2	3.51	4.11	4.83	0.43	10.41
	15.08.2016	918.4	S1N1	1.50	2.21	2.80	0.45	20.28
			S1N2	2.26	2.75	3.99	0.55	19.99
			S2N1	2.69	3.73	4.16	0.47	12.67
			S2N2	2.40	3.83	4.84	0.75	19.60
	31.08.2016	1108.3	S1N1	1.40	1.98	2.55	0.46	23.22
			S1N2	1.57	2.16	3.03	0.42	19.21
			S2N1	0.39	2.89	4.31	1.20	41.50
			S2N2	2.78	3.88	4.55	0.65	16.84
	13.09.2016	1259.3	S1N1	1.49	1.74	2.20	0.22	12.82
			S1N2	1.54	2.22	3.29	0.59	26.67
			S2N1	2.21	2.75	3.84	0.49	17.82

Continued on next page

Table A – continued from previous page

Year	Date	Temperature Sum	Trial	Min	Mean	Max	SD	CV
			S2N2	1.58	2.40	3.31	0.47	19.79
			S1N1	0.69	1.34	2.05	0.39	29.02
	29.09.2016	1397.5	S1N2	0.75	1.33	1.64	0.26	19.27
			S2N1	0.93	1.28	1.85	0.33	25.50
			S2N2	0.19	0.60	0.87	0.23	39.40
			S1N1	0.62	0.81	0.97	0.15	18.16
	16.10.2016	1436.2	S1N2	0.89	1.36	2.25	0.61	45.08
			S2N1	0.64	0.84	0.94	0.14	16.58
			S2N2	0.12	0.22	0.49	0.18	80.26

Table B: NDVI analysis results

Year	Date	Temperature Sum	Trial	Min	Mean	Max	SD	CV
2015	18.06.2015	279.6	S1N1	0.12	0.14	0.16	0.01	7.78
			S1N2	0.16	0.19	0.21	0.01	7.86
			S2N1	0.18	0.20	0.23	0.01	6.66
			S2N2	0.20	0.24	0.27	0.02	8.18
	30.06.2015	371.8	S1N1	0.20	0.27	0.36	0.04	15.04
			S1N2	0.31	0.38	0.44	0.04	10.98
			S2N1	0.35	0.41	0.50	0.04	10.59
			S2N2	0.34	0.45	0.54	0.05	11.42
	16.07.2015	564.7	S1N1	0.49	0.55	0.59	0.03	5.22
			S1N2	0.55	0.61	0.66	0.03	4.47
			S2N1	0.62	0.64	0.69	0.02	2.62
			S2N2	0.61	0.64	0.66	0.02	2.59
	03.08.2015	750.5	S1N1	0.59	0.61	0.62	0.01	1.76
			S1N2	0.63	0.64	0.66	0.01	1.77
			S2N1	0.64	0.66	0.67	0.01	1.93
			S2N2	0.64	0.66	0.68	0.01	2.03
	20.08.2015	931.1	S1N1	0.61	0.63	0.66	0.02	2.76
			S1N2	0.62	0.66	0.69	0.02	3.53
			S2N1	0.66	0.68	0.70	0.01	1.59
			S2N2	0.65	0.68	0.70	0.02	2.44
	11.09.2015	1110.4	S1N1	0.55	0.57	0.60	0.02	3.22
			S1N2	0.57	0.59	0.63	0.02	3.29
			S2N1	0.60	0.62	0.66	0.02	3.65
			S2N2	0.60	0.62	0.64	0.01	2.20
	30.09.2015	1202.9	S1N1	0.55	0.58	0.60	0.02	2.93
			S1N2	0.55	0.58	0.62	0.02	3.82
			S2N1	0.58	0.62	0.63	0.02	2.74
			S2N2	0.58	0.60	0.63	0.02	2.95
	12.10.2015	1244.1	S1N1	0.53	0.56	0.60	0.02	4.17
			S1N2	0.48	0.53	0.60	0.04	7.46
			S2N1	0.51	0.57	0.61	0.03	5.21
			S2N2	0.52	0.55	0.58	0.02	4.49

Continued on next page

Table B – continued from previous page

Year	Date	Temperature Sum	Trial	Min	Mean	Max	SD	CV
2016	15.06.2016	312.7	S1N1	0.12	0.19	0.23	0.04	18.75
			S1N2	0.16	0.23	0.27	0.03	14.88
			S2N1	0.23	0.25	0.28	0.02	7.29
			S2N2	0.18	0.29	0.33	0.05	16.20
	27.06.2016	411.1	S1N1	0.26	0.38	0.45	0.07	18.25
			S1N2	0.38	0.47	0.52	0.04	8.87
			S2N1	0.47	0.51	0.53	0.02	4.55
			S2N2	0.47	0.56	0.62	0.05	8.55
	08.07.2016	515.4	S1N1	0.37	0.47	0.55	0.06	12.77
			S1N2	0.52	0.56	0.57	0.02	3.38
			S2N1	0.57	0.60	0.64	0.02	3.00
			S2N2	0.54	0.62	0.66	0.04	6.42
	19.07.2016	635.4	S1N1	0.55	0.59	0.61	0.02	3.65
			S1N2	0.62	0.63	0.64	0.01	1.32
			S2N1	0.63	0.67	0.69	0.02	2.41
			S2N2	0.65	0.67	0.69	0.01	1.98
	05.08.2016	828.9	S1N1	0.62	0.65	0.66	0.01	2.11
			S1N2	0.65	0.67	0.69	0.02	2.33
			S2N1	0.67	0.69	0.73	0.02	2.75
			S2N2	0.68	0.71	0.73	0.02	3.00
	15.08.2016	918.4	S1N1	0.62	0.63	0.65	0.01	1.41
			S1N2	0.66	0.66	0.67	0.01	1.08
			S2N1	0.66	0.68	0.70	0.01	1.91
			S2N2	0.66	0.69	0.72	0.02	3.62
	31.08.2016	1108.3	S1N1	0.58	0.60	0.64	0.02	3.15
			S1N2	0.60	0.62	0.64	0.01	2.11
			S2N1	0.63	0.65	0.67	0.01	1.57
			S2N2	0.61	0.65	0.68	0.02	3.16
	13.09.2016	1259.3	S1N1	0.57	0.58	0.60	0.01	2.27
			S1N2	0.56	0.59	0.62	0.02	3.52
			S2N1	0.61	0.62	0.64	0.01	1.62
			S2N2	0.56	0.59	0.62	0.02	3.56

Continued on next page

Table B – continued from previous page

Year	Date	Temperature Sum	Trial	Min	Mean	Max	SD	CV
	29.09.2016	1397.5	S1N1	0.52	0.55	0.57	0.02	3.34
			S1N2	0.47	0.53	0.57	0.03	6.13
			S2N1	0.49	0.54	0.57	0.03	5.05
			S2N2	0.42	0.46	0.49	0.02	4.65
	16.10.2016	1436.2	S1N1	0.44	0.48	0.50	0.02	4.87
			S1N2	0.37	0.45	0.52	0.06	13.06
			S2N1	0.44	0.46	0.49	0.02	4.93
			S2N2	0.34	0.39	0.44	0.04	10.33

Table C: GNDVI analysis results

Year	Date	Temperature Sum	Trial	Min	Mean	Max	SD	CV
2015	18.06.2015	279.6	S1N1	0.29	0.31	0.34	0.01	3.58
			S1N2	0.34	0.35	0.39	0.01	4.12
			S2N1	0.34	0.36	0.38	0.01	3.44
			S2N2	0.36	0.40	0.43	0.02	4.55
	30.06.2015	371.8	S1N1	0.24	0.36	0.43	0.04	12.42
			S1N2	0.38	0.46	0.53	0.04	9.16
			S2N1	0.34	0.47	0.56	0.06	12.07
			S2N2	0.45	0.54	0.65	0.05	9.41
	16.07.2015	564.7	S1N1	0.57	0.61	0.64	0.02	3.83
			S1N2	0.62	0.67	0.71	0.03	3.78
			S2N1	0.65	0.68	0.70	0.01	1.82
			S2N2	0.68	0.70	0.73	0.02	2.19
	03.08.2015	750.5	S1N1	0.64	0.67	0.73	0.03	4.49
			S1N2	0.66	0.69	0.74	0.02	3.47
			S2N1	0.66	0.68	0.70	0.01	1.94
			S2N2	0.69	0.70	0.74	0.02	2.30
	20.08.2015	931.1	S1N1	0.65	0.67	0.71	0.02	2.53
			S1N2	0.69	0.70	0.71	0.01	1.15
			S2N1	0.68	0.70	0.71	0.01	1.87
			S2N2	0.70	0.72	0.73	0.01	1.38
	11.09.2015	1110.4	S1N1	0.53	0.55	0.59	0.02	3.42
			S1N2	0.56	0.58	0.60	0.01	2.12
			S2N1	0.56	0.59	0.60	0.01	1.87
			S2N2	0.58	0.59	0.62	0.01	2.15
	30.09.2015	1202.9	S1N1	0.55	0.60	0.64	0.03	4.90
			S1N2	0.53	0.61	0.66	0.04	6.32
			S2N1	0.60	0.63	0.65	0.01	2.36
			S2N2	0.55	0.62	0.66	0.04	6.50
	12.10.2015	1244.1	S1N1	0.56	0.59	0.60	0.01	2.36
			S1N2	0.55	0.58	0.61	0.02	3.52
			S2N1	0.58	0.61	0.64	0.02	3.27
			S2N2	0.58	0.60	0.62	0.01	2.44

Continued on next page

Table C – continued from previous page

Year	Date	Temperature Sum	Trial	Min	Mean	Max	SD	CV
2016	15.06.2016	312.7	S1N1	0.33	0.37	0.40	0.03	8.93
			S1N2	0.33	0.40	0.44	0.03	8.69
			S2N1	0.38	0.41	0.44	0.02	5.14
			S2N2	0.37	0.44	0.48	0.04	7.96
	27.06.2016	411.1	S1N1	0.40	0.50	0.56	0.06	11.25
			S1N2	0.49	0.56	0.59	0.03	5.51
			S2N1	0.54	0.58	0.60	0.02	3.07
			S2N2	0.55	0.62	0.66	0.03	5.53
	08.07.2016	515.4	S1N1	0.52	0.57	0.63	0.05	8.28
			S1N2	0.62	0.65	0.68	0.02	3.04
			S2N1	0.63	0.65	0.67	0.01	2.16
			S2N2	0.67	0.69	0.71	0.01	1.58
	19.07.2016	635.4	S1N1	0.64	0.68	0.72	0.03	4.03
			S1N2	0.66	0.70	0.76	0.03	4.37
			S2N1	0.68	0.71	0.76	0.03	3.57
			S2N2	0.72	0.74	0.80	0.02	3.31
	05.08.2016	828.9	S1N1	0.62	0.67	0.72	0.03	5.17
			S1N2	0.66	0.69	0.73	0.03	3.65
			S2N1	0.66	0.68	0.71	0.02	2.99
			S2N2	0.69	0.71	0.73	0.01	1.99
	15.08.2016	918.4	S1N1	0.64	0.67	0.71	0.02	3.56
			S1N2	0.65	0.68	0.73	0.02	3.57
			S2N1	0.66	0.69	0.71	0.02	2.55
			S2N2	0.67	0.70	0.72	0.02	2.26
	31.08.2016	1108.3	S1N1	0.68	0.70	0.73	0.02	2.35
			S1N2	0.68	0.71	0.75	0.03	3.91
			S2N1	0.69	0.70	0.72	0.01	1.95
			S2N2	0.67	0.72	0.78	0.03	4.27
	13.09.2016	1259.3	S1N1	0.64	0.68	0.71	0.03	3.99
			S1N2	0.66	0.68	0.73	0.03	4.21
			S2N1	0.64	0.67	0.71	0.02	2.93
			S2N2	0.63	0.66	0.69	0.02	3.25

Continued on next page

Table C – continued from previous page

Year	Date	Temperature Sum	Trial	Min	Mean	Max	SD	CV
	29.09.2016	1397.5	S1N1	0.63	0.67	0.68	0.02	2.97
			S1N2	0.60	0.64	0.69	0.03	4.16
			S2N1	0.58	0.62	0.65	0.02	3.69
			S2N2	0.56	0.60	0.63	0.02	4.09
	16.10.2016	1436.2	S1N1	0.48	0.55	0.58	0.05	8.43
			S1N2	0.50	0.55	0.59	0.04	7.44
			S2N1	0.52	0.55	0.58	0.03	4.97
			S2N2	0.51	0.54	0.59	0.03	6.27

Table D: 3BSI analysis results

Year	Date	Temperature Sum	Trial	Min	Mean	Max	SD	CV
2015	18.06.2015	279.6	S1N1	0.16	0.19	0.23	0.02	8.97
			S1N2	0.23	0.27	0.32	0.03	9.50
			S2N1	0.25	0.29	0.35	0.02	8.21
			S2N2	0.29	0.38	0.44	0.04	10.45
	30.06.2015	371.8	S1N1	0.28	0.41	0.61	0.08	19.32
			S1N2	0.48	0.69	0.88	0.12	17.39
			S2N1	0.55	0.77	1.09	0.15	19.74
			S2N2	0.59	0.93	1.36	0.19	20.54
	16.07.2015	564.7	S1N1	1.09	1.32	1.58	0.14	10.47
			S1N2	1.37	1.76	2.14	0.19	10.91
			S2N1	1.76	1.91	2.24	0.12	6.42
			S2N2	1.77	1.94	2.11	0.11	5.63
	03.08.2015	750.5	S1N1	1.63	1.70	1.77	0.06	3.29
			S1N2	1.87	1.98	2.06	0.08	3.83
			S2N1	1.85	2.03	2.17	0.11	5.17
			S2N2	1.96	2.08	2.21	0.09	4.13
	20.08.2015	931.1	S1N1	1.71	1.85	2.05	0.13	6.87
			S1N2	1.87	2.07	2.23	0.12	5.86
			S2N1	2.04	2.22	2.36	0.11	5.00
			S2N2	2.04	2.27	2.42	0.11	4.91
	11.09.2015	1110.4	S1N1	1.19	1.30	1.39	0.08	6.31
			S1N2	1.34	1.41	1.52	0.07	4.85
			S2N1	1.41	1.56	1.74	0.10	6.58
			S2N2	1.52	1.57	1.63	0.04	2.42
	30.09.2015	1202.9	S1N1	1.28	1.41	1.60	0.10	6.92
			S1N2	1.19	1.44	1.71	0.15	10.08
			S2N1	1.41	1.64	1.75	0.10	6.20
			S2N2	1.35	1.57	1.78	0.16	10.31
	12.10.2015	1244.1	S1N1	1.20	1.32	1.51	0.09	7.02
			S1N2	1.00	1.21	1.50	0.16	13.45
			S2N1	1.14	1.41	1.63	0.14	10.16
			S2N2	1.16	1.31	1.47	0.11	8.13

Continued on next page

Table D – continued from previous page

Year	Date	Temperature Sum	Trial	Min	Mean	Max	SD	CV
2016	15.06.2016	312.7	S1N1	0.17	0.29	0.36	0.06	22.21
			S1N2	0.22	0.36	0.44	0.06	18.03
			S2N1	0.34	0.40	0.45	0.04	9.92
			S2N2	0.26	0.49	0.58	0.10	19.96
	27.06.2016	411.1	S1N1	0.40	0.72	0.93	0.19	26.38
			S1N2	0.71	1.02	1.21	0.15	14.47
			S2N1	0.97	1.13	1.24	0.10	8.44
			S2N2	0.97	1.42	1.72	0.24	16.73
	08.07.2016	515.4	S1N1	0.71	1.02	1.36	0.24	23.28
			S1N2	1.31	1.46	1.59	0.10	6.87
			S2N1	1.48	1.65	1.80	0.10	5.95
			S2N2	1.41	1.87	2.07	0.22	11.58
	19.07.2016	635.4	S1N1	1.55	1.66	1.83	0.09	5.57
			S1N2	1.79	1.91	2.08	0.08	4.31
			S2N1	1.86	2.16	2.37	0.17	7.65
			S2N2	2.25	2.32	2.43	0.06	2.60
	05.08.2016	828.9	S1N1	1.69	1.93	2.12	0.15	7.75
			S1N2	1.90	2.10	2.42	0.18	8.55
			S2N1	1.98	2.23	2.57	0.18	7.94
			S2N2	2.15	2.44	2.69	0.19	7.76
	15.08.2016	918.4	S1N1	1.70	1.85	2.00	0.09	5.08
			S1N2	1.89	2.01	2.18	0.10	5.06
			S2N1	2.03	2.17	2.34	0.11	5.28
			S2N2	2.05	2.28	2.60	0.19	8.34
	31.08.2016	1108.3	S1N1	1.67	1.75	1.90	0.07	4.02
			S1N2	1.81	1.91	2.10	0.11	5.69
			S2N1	2.00	2.05	2.14	0.05	2.33
			S2N2	1.86	2.08	2.32	0.16	7.80
	13.09.2016	1259.3	S1N1	1.53	1.61	1.69	0.06	3.79
			S1N2	1.51	1.68	1.87	0.11	6.50
			S2N1	1.68	1.80	1.92	0.10	5.44
			S2N2	1.45	1.60	1.79	0.11	6.58

Continued on next page

Table D – continued from previous page

Year	Date	Temperature Sum	Trial	Min	Mean	Max	SD	CV
	29.09.2016	1397.5	S1N1	1.34	1.44	1.52	0.06	3.91
			S1N2	1.11	1.33	1.50	0.14	10.51
			S2N1	1.07	1.29	1.47	0.13	10.33
			S2N2	0.89	1.03	1.12	0.09	8.54
	16.10.2016	1436.2	S1N1	0.91	1.00	1.09	0.09	9.25
			S1N2	0.69	0.95	1.18	0.20	21.59
			S2N1	0.87	0.95	1.06	0.09	9.09
			S2N2	0.64	0.77	0.95	0.13	16.76